[American Journal of Science, Vol. 320, June, 2020, P. 479–532, DOI 10.2475/06.2020.01]

American Journal of Science

JUNE 2020

RECONSIDERING THE UPLIFT HISTORY AND PENEPLANATION OF THE NORTHERN LHASA TERRANE, TIBET

MIQUELA INGALLS*,§,†, DAVID B. ROWLEY**, BRIAN S. CURRIE***, and ALBERT S. COLMAN**

ABSTRACT. The elevation history of the Tibetan Plateau promises insight into the mechanisms and dynamics that develop and sustain high topography over tens of millions of years, as well as the contribution of uplift-related erosive flux to Cenozoic global cooling. The elevation history of the center and northern margin of the plateau have been historically less well-constrained than the southern margin. A diverse suite of techniques, each with their own biases and uncertainties, yield discrepant mid-Cenozoic elevation estimates (0–5 km). We reconstruct Paleogene to Miocene elevations of the Lunpola basin on the northern Lhasa terrane, the southernmost crustal block of the Tibetan Plateau, using stable isotope paleoaltimetry and clumped-isotope paleothermometry on lacustrine and pedogenic carbonates, integrated with previously published compound-specific n-alkane-derived hydrogen isotopes. Paleo-elevation estimates for the Lunpola basin (~3.1–4.7 km) demonstrate that the northern edge of the Lhasa Block attained high elevation prior to ~24 Ma and potentially by the Early Eocene (<48 Ma). Our results allow for the possibility that the entire Lhasa Block was composed of extremely thick continental crust at the initiation of India-Asia collision, rather than restricting the extent of thick crust to the Linzizong volcanic arc ("Lhasaplano" model) or Gangdese Mountains, and also refutes studies invoking a low elevation interpretation based on higher oxygen and compound-specific δD isotope values. Better constraints on depositional ages in the Lunpola basin are needed to refine the early Cenozoic elevation history along the Bangong-Nujiang suture zone. Finally, we posit that interpretations of proxy data can be biased by incomplete or selective sampling, and propose multi-proxy, intrinsically cross-disciplinary studies to resolve inconsistent interpretations from otherwise unrelated proxies.

Keywords: paleoaltimetry, tectonics, oxygen isotopes, carbonate clumped isotopes, proxy assessment, Tibetan Plateau, Lunpola basin

INTRODUCTION

A comprehensive elevation history of the southern Tibetan Plateau (Lhasa terrane) is critical for understanding the tectonic mechanisms and dynamics that grow and sustain high altitude terranes for tens of millions of years, as well as for correlating uplift-related continental weathering to global cooling. The Tibetan Plateau— ~>4 km above sea level (a.s.l.)—is comprised of several continental terranes that accreted to the southern margin of Eurasia during Mesozoic collisions (Chengfa and others,

* Division of Geological and Planetary Sciences, California Institute of Technology, Pasadena, California 91125 USA

** Department of the Geophysical Sciences, The University of Chicago, 5734 S. Ellis Avenue, Chicago, Illinois 60637 USA

*** Department of Geology and Environmental Earth Science, Miami University, Oxford, Ohio 45056 USA

† Present address: Department of Geosciences, Pennsylvania State University, University Park, Pennsylvania 16802

† Corresponding author: ingalls@psu.edu

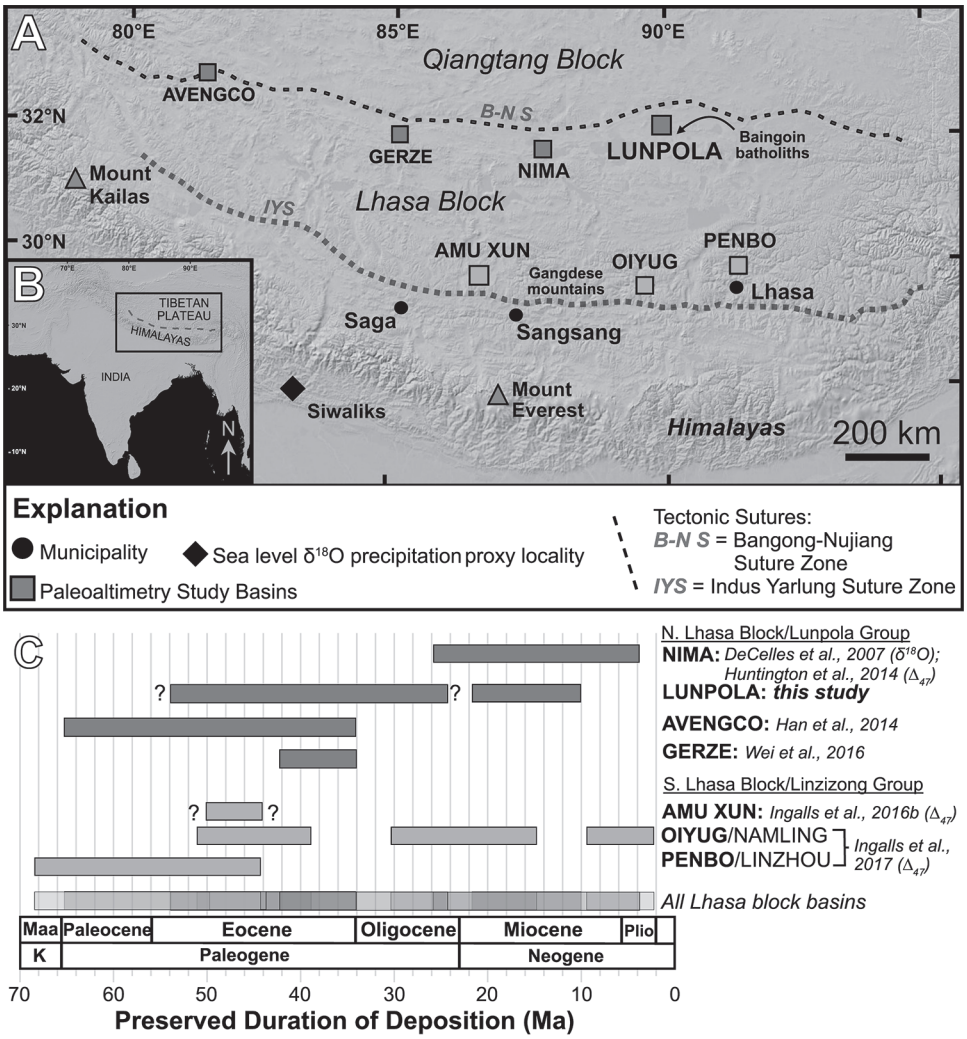

Fig. 1. (A) Regional map of the Lhasa tectonic block with localities of previous (DeCelles and others, 2007b; Han and others, 2014; He and others, 2007; Huntington and others, 2015; Ingalls and others, 2017; Wei and others, 2016) and current paleoaltimetry and basin studies marked. (B) Location map of India-Asia collision zone and the Himalaya. (C) Time intervals recorded by and preserved in sedimentary basins discussed in the text, and total Cenozoic preserved sedimentary sequences across the Lhasa block.

1986). The active continental margin between India and Eurasia is defined by the Gangdese mountain range and Linzizong volcanic arc that formed in the Late Cretaceous to Early Cenozoic as a result of the northward subduction of the Neotethyan oceanic lithosphere prior to the onset of India-Asia collision (Murphy and others, 1997; Ding and Lai, 2003). New thrust fault-bound basins (for example, Oiyug, Penbo; fig. 1) formed to the immediate north and south of the Indus-Yarlung Suture (IYS) consequent to continental collision (Kapp and others, 2007; DeCelles and others, 2018). These depocenters, filled with fluvial-lacustrine sedimentary rocks, have been the focus of extensive paleo-altitude reconstructions (DeCelles and others, 2011; Quade and others, 2011; Ding and others, 2014; Huntington and others, 2015; Currie

and others, 2016; Ingalls and others, 2017) aimed at determining the temporal relationship between Tibetan uplift and India-Asia collision. These records support the hypothesis that the entire Linzizong arc was >4 km a.s.l. (Ingalls and others, 2017) by at least 56 Ma (He and others, 2007). However, there have been far fewer paleoaltitude studies of the northern margin of the Lhasa terrane. More robust constraints on the northern elevation history are required to test the "Lhasaplano" model for Tibetan Plateau development—that is, that the entire Lhasa terrane was high-standing prior to collision—and to make quantitative estimates of the contribution of uplift-related erosive flux to global Cenozoic cooling.

Previous Elevation Reconstructions of the Northern Lhasa Terrane

In this study, we considered existing paleo-elevation records from four sedimentary basins across the northern Lhasa block—Avengco, Gerze, Nima, and Lunpola—with a particular focus on the relatively well-studied Lunpola basin (fig. 1), for which we provide new clumped isotope temperatures of carbonate formation [$T(\Delta_{47})$]. Previous studies of the Lunpola basin have used a variety of paleontology, palynology, and geochemistry techniques, each with their own biases and uncertainties. In some cases, new records have only broadened the discrepancies in paleoelevation estimates. For example, paleontological records that infer ancient environmental conditions and elevations based on the ecosystems and altitudes occupied by nearest living relatives (NLRs) have been used to suggest the Lunpola basin could have been anywhere from approximately sea level (Wei and others, 2016; Wu and others, 2017) to 3 km a.s.l. (Tao and others, 2012) in the Oligocene. Alternatively, the NLRs of Eocene fossils found in the Lunpola basin could suggest a warmer than modern and dry climate without altitude implications (Sun and others, 1984; Wu and others, 2008). However, excluding Wei and others (2016), no NLR studies have rigorously assessed the "chicken and egg" conundrum presented by Molnar and England (1990). That is, paleontological reconstructions of ancient environments are based on the geographic and altitudinal range occupied by NLRs of an extinct species in the modern climate, but range is highly sensitive to local climate-related parameters and global climate change (for example, Peppe and others, 2011)—in particular, intensification of icehouse conditions since the Eocene. Thus, were the species present in the Eocene Lunpola basin different from today due to a warmer global climate or altitudinal range restrictions? NLR-based altitude reconstructions assume modern climate conditions (that is, temperature and moisture lapse rates). If absolute temperature and precipitation tolerances of a genus remained relatively static through geologic time, Paleogene and Early Neogene NLRs would have had an expanded geographic range due to warmer and moister conditions relative to modern relatives in a colder and drier late Cenozoic climate. From this perspective, NLR estimates should be viewed as absolute minima and not actual paleo-elevation estimates.

Palynological records are interpreted to demonstrate a change in ecosystem temperatures and/or precipitation, which have been related to change in land surface elevation. However, even within the palynological literature, different positions are taken on the use of pollen abundance in tectonic reconstructions. Wu and others (2014) suggested that the Late Oligocene to Miocene decrease in subtropical pollen and leaf fossils from Tibet could have been due to global cooling rather than a local increase in altitude, but did not address the origin of the associated depleted isotopic compositions. Alternatively, Sun and others (2015) used the mixed pollen distribution of lowland and coniferous species to argue for a topographically variable landscape of peaks and interconnected valleys. However, the absence of geological evidence for deeply incised valleys, such as coarse clastic sedimentary deposits anywhere within the widely distributed flood plain and lacustrine stratigraphic record of the Cenozoic of

the Tibetan Plateau (Zhang and others, 2013), challenges interpretations for mountainous and topographically varied landscapes.

Oxygen and hydrogen stable isotope-based paleoaltimetric reconstructions, as employed in this study, use a theoretically and empirically calibrated model based on the Rayleigh distillation of oxygen and hydrogen isotopes of vapor, and thus rainwater, as vapor increases in elevation and rains out over land (Rozanski and others, 1993; Chamberlain and Poage, 2000; Rowley and others, 2001). The model input is the difference in stable isotopic compositions of meteoric water ($\delta^{18}O_w$) and coeval, ideally sea level meteoric water ($\Delta(\delta^{18}O_w) = \delta^{18}O_{w,sea\ level} - \delta^{18}O_{w,sample}$; Rowley and others, 2001). In previous work, leaf wax hydrogen (δD_{lipid}; Polissar and others, 2009) and carbonate oxygen isotopic compositions ($\delta^{18}O_c$; Rowley and Currie, 2006) have been used to reconstruct compositions of ancient meteoric water in the Lunpola basin, and to calculate Eocene elevations of ~4050 m and 3600 to 4100 m, respectively, with sustained elevations above 4km since the Eocene. However, Wei and others (2016) interpreted calcareous fossils far inland from any other known marine sedimentary rocks as marine foraminifera transported 100s of km by "storm surges". They combined that interpretation with screening for higher measured $\delta^{18}O_c$ values to reconstruct a low elevation for the Gerze basin during the late Eocene. Wei and others (2016) estimated that the Gerze basin was near sea level from 39 to 36 Ma with >3 km of surface uplift in the subsequent 10 Myr. The foraminifera-bearing strata were coeval with and co-latitudinal with the Lunpola basin lacustrine and pedogenic carbonates measured by Rowley and Currie (2006) and in this study (fig. 1), but Wei and others (2016) did not use the Lunpola basin isotopic data in their reconstruction. Instead, Wei and others (2016) interpreted ^{18}O-depeleted carbonates within the Dingqinghu Formation as the product of water-rock burial alteration, and ^{18}O-enriched carbonates as a record of the primary lake water in equilibrium with meteoric water. However, in closed-basin lakes, lake water can become enriched in ^{18}O and D relative to meteoric water due to evaporative Rayleigh distillation (Stumm and Morgan, 1981), and this "evaporative enrichment" is recorded by $\delta^{18}O_c$ and δD_{lipid}. Wei and others (2016) assessed the degree to which their lacustrine records reflected open versus closed system behavior by examining the covariation of $\delta^{13}C_c$ and $\delta^{18}O_c$, a commonly employed assessment based on Talbot (1990). Their micritic carbonate showed no correlation and were therefore assumed to record open system hydrology. Sparites showed a negative covariation, orthogonal to that expected from evaporation, with $\delta^{18}O_c$ values in the sparites reaching ~−20‰VPDB. Wei and others (2016) did not distinguish $\delta^{18}O_c$ compositions of vein filling sparite from early diagenetic sparite infilling of shells. Covariation of $\delta^{13}C_c$ and $\delta^{18}O_c$ is common but not a universal rule and is less robust than multi-proxy assessments of evaporative effects. For example, partnering measurements of ^{18}O-enrichments in lacustrine carbonates with D-enrichments in leaf waxes (for example, Polissar and others, 2009; this study) or with $\Delta^{17}O$ analyses of the same carbonate minerals (see Discussion) provides external checks on syn-depositional isotope effects and basin hydrological balance when contextualizing proxy data from basin catchments.

A common thread among all proxy-based environmental reconstructions is the basic principle that sedimentary basin strata record a progression of environmental conditions within a region. Environmental proxies analyzed from sequential strata (for example, $\delta^{18}O_c$, δD_{org}, $\delta^{13}C_{org}$, $\delta^{13}C_c$, *et cetera*) reflect changes in temperature, atmospheric circulation, precipitation composition and amount, regional ecology, and changes in latitude and altitude caused by tectonic processes. However, syn- and post-depositional processes can alter the primary environmental signal recorded by the proxy material. For example, lake or soil water evaporation and carbonate recrystallization during burial diagenesis can alter the primary isotopic composition of meteoric

water recorded by carbonate minerals. The relative contributions of primary and secondary processes to a material's final isotopic composition can vary daily to seasonally and on longer geologic time scales, respectively. Therefore, individual depositional environments may yield significantly different compositions from rocks directly below, above, or even adjacent, without necessarily indicating tectonic or climatic changes. For example, in modern environments with dynamic hydrography, such as closed-basin lakes, the existence of primary ^{18}O-enriched carbonate does not preclude the existence of primary ^{18}O-depleted carbonate in the same basin stratigraphy although carbonate rock within the strata may have been deposited in the same environmental and tectonic setting and at the same paleoelevation (Ingalls and others, 2020). Therefore, a better understanding of the physicochemical processes and conditions recorded by each proxy material and how they may be compromised is necessary for building a robust model for the tectonic evolution of the Lhasa block.

Reconstructing Ancient Rainwater Isotopes in Arid Climates

The Global Meteoric Water Line (GMWL; Craig, 1961; Rozanski and others, 1993) describes the relationship between δ^2H_w (δD_w) and $\delta^{18}O_w$ compositions of global meteoric waters—generally represented by:

$$\delta D_w = 8*\delta^{18}O_w + 10 \quad (1)$$

There can be local deviations from GMWL due to local climate and atmospheric circulation. For example, evaporation due to aridity shifts hydrogen and oxygen isotopes towards more enriched values, or to the right of the GMWL. However, the modern (2005–2010) local meteoric water line (LMWL) in Lhasa, constructed from isotopic data from the CHNIP (Chinese Network of Isotopes in Precipitation) station, is essentially invariant from the GMWL ($\delta D_{mw} = 8.04*\delta^{18}O_w + 10.06$; Liu and others, 2014).

A study of $\delta^{18}O$ and δD compositions of modern lake water from open and closed lake systems across the Tibetan Plateau yielded a Tibetan lake water line (TLWL) slope of 5.2 (Yuan and others, 2011), suggesting a stronger influence of evaporation on lake waters than other surface waters. The extent of evaporative kinetic isotope effects is largely dependent on atmospheric relative humidity and wind speed (Craig and Gordon, 1965). The trajectory of evaporated water off the LMWL defines a local evaporation line (LEL)—a tie line between the unevaporated water on the LMWL (Gonfiantini, 1986) and evaporatively enriched compositions. Transpiration of plants is driven by an evaporative flux from leaves and thus shifts the isotopic composition of leaf water to heavier isotopic compositions than the local precipitation source. Slopes associated with evaporative enrichment for various vegetation ecosystems were empirically determined in Polissar and Freeman (2010). For example, a slope of ~1 is expected for mixed forest-shrub vegetation—the closest modeled ecosystem to the vegetation type thought to have existed in the Miocene Lunpola as evidenced by pollen data (Sun and others, 2014).

The local relationship between $\delta^{18}O_w$ and δD_w in an evaporative system can be used to correct isotopic compositions recorded by carbonates and leaf waxes, respectively, back to primary meteoric compositions. This approach involves projecting the calculated water isotopic composition along a LEL back to the GMWL. Polissar and others (2009) applied a very conservative slope of 1 to paired lipid δD and carbonate $\delta^{18}O$ measurements derived from the same samples from Lunpola basin lacustrine strata to estimate the isotopic composition of Niubao (late Eocene) and Dingqinghu (late Oligocene to Miocene) surface waters in the central Tibetan Plateau. Polissar and Freeman (2010) found that the value of precipitation calculated using this approach was comparable to the lowest $\delta^{18}O_w$ values from carbonates at this locality, which are

presumably the carbonates least effected by evaporative enrichment. Therefore, the use of multiple precipitation proxies in strongly evaporative systems—such as lakes in high-altitude, arid climates—provides a quantitative method of correcting evaporative fractionation to estimate primary isotopic values.

Following Polissar and others (2009), we used the LEL to correct carbonate and lipid-derived evaporatively enriched $\delta^{18}O_w$ and δD_w values back to primary meteoric $\delta^{18}O_w$. We then reassessed the existing stable isotope paleoaltimetry records of the Lunpola basin using these corrected $\delta^{18}O_w$ values in the $\Delta(\delta^{18}O_w)$ elevation calculations discussed above. We further constrained the $\delta^{18}O_w$ calculations by using clumped isotope thermometry [$T(\Delta_{47})$] to directly measure the temperature of mineral formation for the late Oligocene to Miocene and late Eocene carbonates. $T(\Delta_{47})$ was used to calculate the temperature-dependent equilibrium fractionation between paleo-waters and proxy carbonate. In addition, we contextualized our multi-proxy data within the interpretive framework of previous studies, and prescribed possible tests and collaborative, interdisciplinary efforts to improve future reconstructions of land surface elevations. Our revised elevation record, considered within the interpretive framework of existing studies, aids in our understanding of the timing of peneplanation and extent of the high-altitude terrane in the early Cenozoic.

Recent Arguments Against Stable Isotope Paleoaltimetry

Recently, Botsyun and others (2019) called into question all interpretations based on stable isotope paleoaltimetry. Botsyun and others (2019) used an isotope-enabled general circulation model (GCM) to examine the distribution of predicted oxygen isotopic compositions in a warmer, Eocene world. Their primary result was the prediction of an inverted isotopic lapse rate in the regions of the Himalaya and Tibet characterized by ^{18}O-depleted compositions ($\delta^{18}O_w \sim -9$ to -12‰VSMOW) at low elevations in the Eocene proto-Indo-Gangetic plain, and relatively ^{18}O-enriched isotopic compositions ($\delta^{18}O_w > -7$‰VSMOW) immediately north in the region of the Tibetan Plateau. Thus, the best fit from their analyses comparing model predictions with measured isotopic compositions was a low Tibetan plateau paleo-elevation. Here, we have summarized their approach and outlined critical issues regarding their model that either undermine or raise significant questions regarding their results.

Data-model comparisons that involve paleogeographic reconstruction, such as that of Botsyun and others (2019), require that the data localities and model paleogeography be independently constrained and within the same coordinate system. Placing the external data and the model within the same reference frame allows the model predictions and data at each given location to be explicitly compared. The configuration of the continents in the Botsyun and others (2019) model accords with other Eocene paleogeographic reconstructions at *circa* 40 Ma (Lunt and others, 2016). However, Botsyun and others (2019) shifted the paleo-positions of the data localities (paleo-basins) independently from the underlying continental crust—specifically, by ~13°S relative to where those localities would be positioned if affixed to the rotating crust (fig. 2). Botsyun and others (2019) applied a uniform ~1400 km southward displacement to all data localities within and external to the Himalaya-Tibet orogenic system, including those in Tarim, Qaidam, Mongolia, northeastern China, and eastern China, regardless of actual latitudinal displacements relative to Eurasia due to internal deformation. The ~1400 km displacement is only relevant to localities on the Tibetan Plateau and the central Burma basin which are certainly displaced relative to Eurasia, but the distribution of shortening within these regions remains uncertain from structural assessments (van Hinsbergen and others, 2011) and the resolution of paleomagnetic data does not allow for this level of discernment (Rowley, 2019). To account for location uncertainty in model predictions of Botsyun and others (2019), the modeled paleogeography must be adjusted and models rerun to reflect that

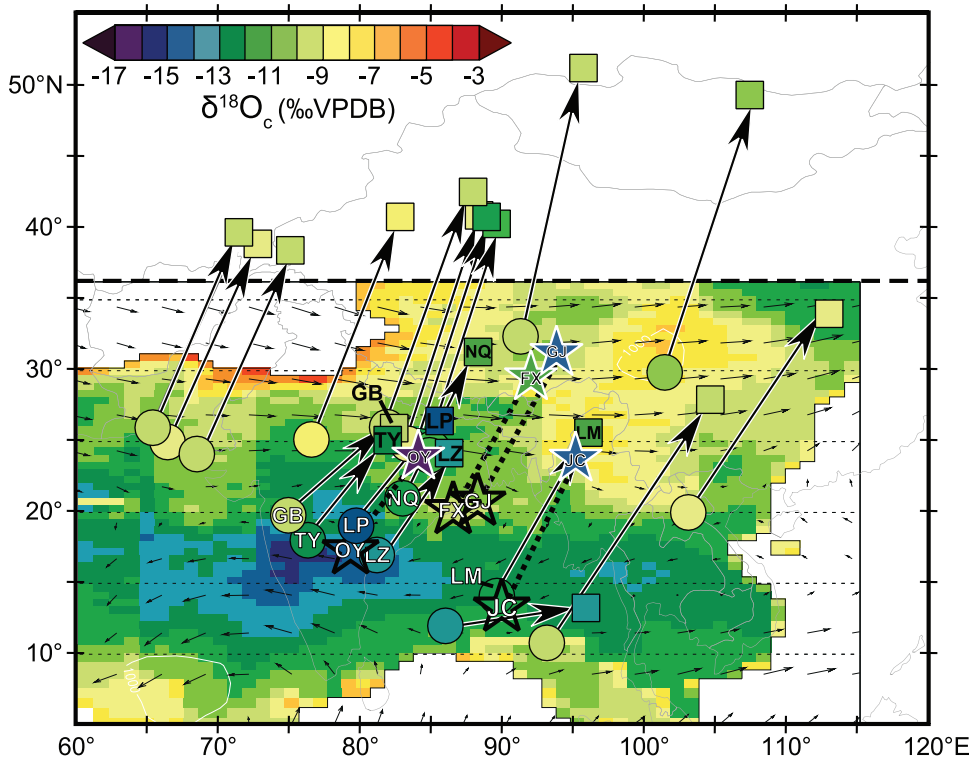

Fig. 2. Predicted compositions of terrestrial carbonates from the EOC-S simulation of Botsyun and others (2019; colored background) compared with measured isotopic compositions of carbonates from the literature. Circles are the locations of Eocene data plotted as per Botsyun and others (their Fig. 5B) with measured compositions colored to same composition scale. White letters refer to the localities of the most ^{18}O-depleted samples from Gerze Basin (GB), Nangqian Basin (NQ), Tangra Yum Tso (TY), Gonjo Basin (GJ), Liming Basin (LM), Jianchuan Basin (JC), Linzhou Basin (LB), Oiyug Basin (OY), and Lunpola Basin (LP) as plotted by Botsyun and others (2019) with four additional localities plotted relative to the locations of the other basins in the Botsyun and others (2019) coordinate frame (unfilled black stars) and in the same reference frame as the continental crust (colored stars). Squares with black letters are the locations of the localities in the same frame of reference as the continental crust. Arrows show the dislocation of Botsyun and others (2019) locality placement (circles) from a coordinate frame tied to the continental crust (squares).

reconfiguration, or the sampled model domain must be expanded beyond the existing model domain to account for these uncertainties. Further, given that the localities are autochthonous relative to the underlying bedrock, any large-scale displacement requires movement of the underlying crustal blocks thereby reconfiguring the paleogeography. Thus, the paleogeography and all of the localities with measured isotopic compositions have been reconstructed in completely different coordinate systems such that the data-model comparisons are invalid.

Nonetheless, we assessed the data-model comparisons of Botsyun and others (2019) emphasizing the measured carbonate oxygen isotopic compositions from the Eocene Tibetan Plateau upon which all published interpretations of high Eocene paleoelevations have been based. Botsyun and others (2019) favored their model EOC-S, which placed the Himalaya and Tibetan Plateau <500 m a.s.l. and, therefore, implied that paleotopography played no role in the distribution of oxygen isotopic compositions across the Tibetan landscape. We found that this interpretation was not supported by their own modeling results when the misplaced data localities were used

(fig. A1). We also compared modeling results with data placed in paleogeographically correct positions (fig. 2).

The original Botsyun and others (2019) comparisons used five of the nine published Eocene age lacustrine and paleosol study sequences from the Tibetan Plateau: the Pana Formation of the Penbo/Linzhou basin (Ding and others 2014), Tangra Yum Tso (Xu and others, 2015), Gerze Basin (Wei and others, 2016), Liming Basin (Hoke and others, 2014), and Lunpola Basin (Rowley and Currie, 2006; Polissar and others, 2009; this study). We added the Jianchuan Basin (Li and others 2015 with updated ages from Gourbet and others, 2017), Nangqian Basin (Li and others, 2019), Gonjo Basin (Tang and others, 2017), and Oiyug Basin (Ingalls and others, 2017) to our reassessment. We also included a more ^{18}O-depleted value from the Pana of the Penbo Basin from Ingalls and others (2017), making ten measured isotopic compositions to be compared with predictions from the various models of Botsyun and others (2019).

In general, successful data-model comparisons are characterized by simple residuals (that is, the difference between measured and modeled compositions) that scatter about a value of zero, such that the sum of those residuals has a value close to zero. Sum-squared residuals, the measure used by Botsyun and others (2019) to assess data-model fit, assumes a distribution of residuals scattered about zero. This assumption was not met by the model predictions of Botsyun and others (2019); rather, mean residuals are skewed strongly towards model simulations of higher $\delta^{18}O_c$ values than the measured $\delta^{18}O_c$ values at almost all localities (fig. A1). Thus, the model simulations of Botsyun and others (2019) did not successfully explain the data. The mean $\delta^{18}O_c$ value of the 10 study sites was −15.1‰VPDB, whereas the mean compositions predicted by the models at those same locations ranged from −8.2‰ to −12.4‰. The data-model mismatch is exacerbated when the paleo-localities are projected from the paleogeographic reference frame employed in Botsyun and others (2019) to the more accurate paleogeographic configuration relative to the underlying continental crust (fig. 2). For example, the most ^{18}O-depleted model prediction of −12.4‰VPDB increased to −9.6‰ when the localities were moved in accord with their underlying continental crust. Thus, the models did not yield predicted compositions compatible with the majority of observed $\delta^{18}O$ values from the Eocene of the Tibetan Plateau.

Finally, the inverted lapse rate that is a fundamental result of their model was achieved in part due to an extreme continentality effect on the isotopic composition of precipitation in the foreland region. In situations dominated by tropical rainforests, comparable to that modeled by Botsyun and others (2019) in the foreland of the Himalaya, the continentality effect on oxygen isotopes of meteoric water is muted due to the wholesale overturning of the moisture by efficient evapo-transpiration. However, the models of Botsyun and others (2019) had an effective continentality effect of 5‰/1000 km, >5 times larger than across the modern Amazon (Rozanski and others, 1993) or Sudd (Levin and others, 2009) regions.

In summary, Botsyun and others (2019) reconstructed the paleogeography of all data localities separately from the underlying paleogeography used in their modeling efforts, thereby invalidating their data-model comparisons. The vast majority of the data-model residuals reflected the model's inability to yield the observed ^{18}O-depleted compositions of almost all Eocene sites on the Tibetan Plateau. These are precisely the data upon which interpretations of high Eocene paleo-elevation have been predicated. The simple implication is that these models in their published configuration have little power to address the origin of these low $\delta^{18}O$ values, and hence, these models are not yet ready to assess whether existing paleoaltimetry estimates are valid or not. In addition, the negative lapse rates largely reflected significant continentality effect along the southern margin of their modeled Himalaya and Tibetan Plateau where

modern analog environments experience very minimal continentality effect (Levin and others, 2009). The conclusions derived by Botsyun and others (2019) should be reevaluated within a revised model framework and have not yet provided key insight as to the paleo-elevation history of the Tibetan Plateau.

GEOLOGIC SETTING

The axis of the Lunpola basin, positioned within the northern Lhasa Block adjacent to the Bangong-Nujiang suture zone (BNSZ; fig. 1), strikes roughly east-west, parallel to the bounding thrust faults and folds associated with north-south shortening during India-Asia convergence (Rowley and Currie, 2006). The BNSZ formed in the latest Jurassic to Early Cretaceous during the collision of the Lhasa and Qiangtang terranes. The origins of the northern Lhasa terrane basins in the Cenozoic remains uncertain, although early extensional structures in the Lunpola have been reactivated as thrusts (Wei and others, 2017), most recently within a 200 to 300 km-wide and 1500 to 1800 km-long zone of conjugate strike-slip faults accommodating east-west extension and north-south contraction (Taylor and others, 2003) (fig. 3A).

Eocene to Pliocene strata in the Lunpola basin are up to more than 4 km thick (Bureau of Geology and Mineral Resources Xizang Autonomous Region; fig. 3B). The strata are most commonly divided into two units: the Eocene to Oligocene Niubao Formation (Fm), with Middle and Upper members, and the Late Oligocene to Pliocene (?) Dingqinghu Fm (Rowley and Currie, 2006) (also referred to as the Dingqing Formation). In this study, we analyze samples from the Middle and Upper Members of the Niubao Fm and the Dingqinghu Fm previously collected by Rowley and Currie (2006; fig. 3). Age constraints are derived primarily from ostracods and palynological assemblages from the efforts of regional geologic mapping and petroleum exploration campaigns (Xu, 1980; Xia, 1983; Xu and others, 1985; Bureau of Geology and Mineral Resources Xizang Autonomous Region, 1992). He and others (2011) provides a zircon U-Pb age of 23.5 ± 0.2 Ma (2σ, MSWD = 1.1) from a bentonite layer in the middle to lower Dingqinghu Fm. More recently, Mao and others (2019) added two tuff ages of 20.7 ± 0.1 Ma and 20.6 ± 0.1 Ma from the middle of the Dingqinghu Fm in the Lunpori section ~24 km to the WNW of our sampling sites, and Ma and others (2017) correlated the Papa section of Sun and others (2014) that is ~5 km to the NW of our sample locality with the middle Dingqinghu Fm (fig. 3A) and suggesting an age closer to 20 Ma for our Dingqinghu samples. These ages place the upper bound of our Niubao Fm samples to late Oligocene. A maximum age of the Niubao Fm is provided by a low temperature thermochronology study conducted 60 km to the south in the Baingoin area of Haider and others (2013). Here, the Niubao Fm nonconformably onlaps Cretaceous plutonic rocks with apatite fission track and comparable AHe ages as young as ~56 to 52 Ma within 1 km of the low-dipping onlapped surface (fig. 3). A younger (<48 Ma) age of the Niubao Fm is implied by the dearth of interbedded tuffs given the thick and extensive Eocene volcanism preserved in the Pana Formation of the Linzizong Group (Zhu and others, 2019) no more than a few hundred kilometers to the south.

Although detailed correlations are not yet available, co-latitudinal basins characterized by similar sequences include the Nima (DeCelles and others, 2007b; DeCelles and others, 2007a), Gerze (Wei and others, 2016), and Avengco (Han and others, 2014; fig. 1). Wei and others (2016), working farther west in the Gerze basin, correlated what they referred to as the Dingqinghu Fm to the late Eocene (42–34 Ma) based on biostratigraphy, and further refined to 39.4 to 35.7 Ma based on magnetostratigraphy. Correlating our Dingqinghu Fm samples to the stratigraphy of He and others (2011) is not straightforward because they sampled from the westernmost reach of the Lunpola basin (fig. 3A). Mao and others (2019) sampled the ~650 m thick Lunpori section approximately 24 km to the WNW of our collection site for Dingqinghu Fm samples,

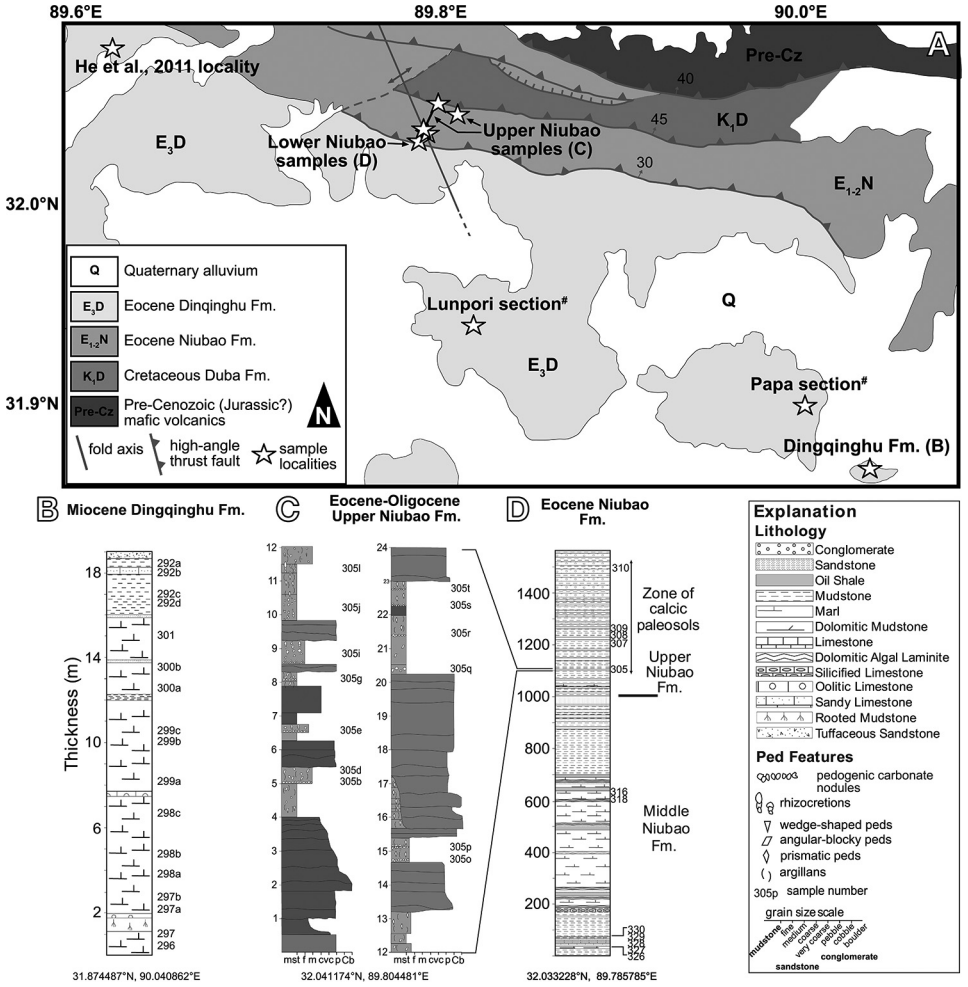

Fig. 3. Stratigraphy of the Lunpola basin and sample locations. (A) Simplified geologic map of Lunpola basin with sampling localities from this study, He and others (2011), and the Lunpori and Papa sections of Ma and others (marked by #; 2017) marked with stars, modified from maps found on the National Geologic Archives of China server (http://geodata.ngac.cn). (B, C, D) Stratigraphic sections of the (B) Miocene Dingqinghu Formation, (C) upper Niubao Formation, and (D) Lower Niubao Formation.

and the spatial correlation between the two sites is also unclear. However, we can assign a loose age of Oligocene or younger to our Dingqinghu section (Wu and others, 2008) (fig. 3). These broad constraints place the age of the unconformity between the Dingqinghu Fm and upper Niubao Fm somewhere in the late Eocene to Oligocene. Within these constraints, our Middle and upper Niubao samples are likely Eocene to Oligocene in age.

Lithologies of the middle Niubao member are dominated by lacustrine deposits (fig. 3). In the sampled strata of Rowley and Currie (2006) and this work, the middle Niubao is composed of lacustrine mudstones, micritic and marl limestones, algal dolostones and dolomitic marls, and kerogenous shale. The upper Niubao member is dominated by more than 400 meters of fluvial/alluvial mudstones, sandstones, and conglomerates with intercalated calcic paleosol horizons. Peds are typically wedge-

shaped, angular-blocky, or prismatic. Pedogenic carbonate nodules and rhizocretions were sampled for stable isotopes. The Dingqinghu Formation is composed of lacustrine marls and limestones. Rowley and Currie (2006) sampled from the Middle Dingqinghu member in the south-central part of the basin where there is 19 meters of exposure. The base of the section is lacustrine marl with a few interbeds of oolitic limestone, rooted mudstone, and conglomeratic sandstone. The upper part of the Dingqinghu section is mostly mudstone, sandy limestone, and sandstone.

METHODS

Sample Preparation and Diagenetic Screening by Microscopy

Samples were sectioned perpendicular to the orientation of dominant fabrics and laminations, and polished. For each sample, one cut face was used to micromill powder for stable isotope analyses and, for a subset, the other half was thin sectioned. Thin sections were optically screened for recrystallization fabrics due to water-rock burial diagenesis, loss of primary porosity, or other fabrics indicative of thermal maturity, and imaged on a Zeiss Axio Imager microscope with a motorized XY stage for thin section-scale composite imaging at the University of Illinois-Chicago. In two samples (330C and 316), we used the Electron Backscatter Diffraction (EBSD) system of the Zeiss 1550VP Scanning Electron Microscope (SEM) housed at Caltech to map preferred crystal orientation, grain size, and grain boundary relationships. EBSD is employed to identify the presence or absence of grain ripening and preferred crystallographic orientations expected of recrystallized micrite (Shelley, 1993; Prior and others, 1999).

Carbon and Oxygen Isotopes of Carbonates

In this study, we measured the $\delta^{18}O_c$ and $\delta^{13}C_c$ compositions of 41 carbonate samples from the early Eocene to Miocene strata in the Lunpola basin. Many of the carbonate $\delta^{13}C$ and $\delta^{18}O$ measurements from each of the three formations were originally reported in Rowley and Currie (2006), and additional measurements were made on a ThermoScientific Delta V paired to a GasBenchII at the University of Chicago in 2016. All isotope ratios are reported using delta notation in parts per thousand (‰) on the VPDB scale, except for calculated $\delta^{18}O_w$ compositions that are reported on the VSMOW scale. $\delta^{13}C_c$ and $\delta^{18}O_c$ values were corrected for sample size dependency and then normalized to the VPDB scale with a three-point calibration (Coplen and others, 2006) using NBS-19.

Carbonate Clumped Isotopes

We performed carbonate clumped isotope analyses on nine of the carbonate samples at the California Institute of Technology in October 2018. Representative samples from each geologic formation that appeared to retain primary or early diagenetic textures were chosen to provide a clumped isotope-derived paleotemperature estimate for each unit.

Clumped isotope measurements of carbonates were analyzed by phosphoric acid digestion in a common acid bath at 90 °C. Contaminants and isobaric interferences were removed from extracted CO_2 from samples and standards cryogenically on the Caltech 'autoline' and through a gas chromatography column. Purified CO_2 was analyzed on a MAT253 gas source mass spectrometer. We measure $\delta_{44\text{-}49}$ as ion current ratios, which are converted to $\delta^{13}C$, $\delta^{18}O$, "raw" Δ_{47}, and "raw" Δ_{48} using the IUPAC ^{17}O correction parameters (Brand and others, 2010). Carbon and oxygen isotope ratios are calculated relative to an Oztech isotopic standard gas (CALT-2049C, $\delta^{13}C = -3.62‰$ VPDB; $\delta^{18}O = 24.97‰$ VSMOW; VSMOW used in Δ_{47} calculations) used as the working reference gas, and Δ_{47} and Δ_{48} are computed relative to the working gas

reference frame. The Δ_{47} values are projected from a working gas reference frame to the Carbon Dioxide Equilibrium Scale (CDES; Dennis and others, 2011) to allow for interlaboratory comparison. To do so, standard CO_2 gases heated to 1000 °C (HG) and CO_2 equilibrated through reaction with water at 25 °C (EG) were measured daily, and a "heated gas line" was created from the δ_{47}-Δ_{47} relationship of the HGs and EGs. An empirical transfer function was created to project $\Delta_{47,\mathrm{SG\text{-}WG}}$ values to $\Delta_{47,\mathrm{CDES}}$ using the slope and intercept of the heated gas line, following the procedures described by Ghosh and others (2006), Huntington and others (2009), and Passey and others (2010). Next, $\Delta_{47,\mathrm{CDES},90}$ values are corrected to an acid digestion temperature of 25 °C ($\Delta_{47,\mathrm{CDES},25}$) using the temperature dependent acid fractionation factor for calcite computed by Guo and others (2009). Finally, carbonate $\Delta_{47,\mathrm{CDES},25}$ values are corrected to two standards, Carrara Marble and TV04 (fig. A2). Individual replicates were averaged together to create final sample Δ_{47} values, and sample-average Δ_{47} errors were calculated in quadrature considering the "external" uncertainty of each replicate analysis:

$$\sigma_{\Delta_{47,CDES,25}} = \sqrt{\frac{\sum \sigma^2_{external}}{\mathrm{n}}},$$

and propagated through the 95 percent confidence interval of the heated gas regression.

We use the Bonifacie and others (2017) T-Δ_{47} calibration to calculate temperatures from Δ_{47} values. Recent calibrations have demonstrated that distinct sample preparation and analysis protocols can yield Δ_{47}-T relationships in agreement with each other (Kelson and others, 2017), suggesting a movement towards a single T-Δ_{47} relationship. Bonifacie and others (2017) present the most individual carbonate preparations on the widest diversity of materials, minerals, and temperature range, and determine a T-Δ_{47} calibration equation in agreement with inorganic (Ghosh and others, 2006a) and biogenic (Ghosh and others, 2007; Eagle and others, 2010; Thiagarajan and others, 2011, *et cetera*) calibrations, and allows for constrained temperature estimates of high-T minerals in metamorphic settings. Further, the Bonifacie calibration was conducted through a series of cross-referenced experiments and measurements between Caltech and IPGP, so half of the calibration was performed on the same instrument following the same gas preparation and analytical protocol as in this study. This calibration uses the $\Delta_{47,\mathrm{CDES},90}$ value rather than correcting to a 25 °C acid digestion because all of the analyses were made under these carbonate digestion conditions, and nearly all clumped isotope laboratories digest carbonate at 90 °C at this time. Two sigma T(Δ_{47}) errors are calculated by propagating the 2σ $\Delta_{47,\mathrm{CDES}}$ error of the sample through the T-$\Delta_{47,\mathrm{CDES}}$ calibration equation.

T(Δ_{47}) ($\pm 2\sigma$) from representative samples within each geologic formation were used to calculate oxygen isotopic values of ancient surface water ($\delta^{18}O_w$) from carbonate rocks ($\delta^{18}O_c$) for all carbonates within the same formation that did not have Δ_{47} measurements. Additionally, where possible, each carbonate lithology (that is, lacustrine versus pedogenic) found in the measured section is measured to account for isotopic and geochemical behavior specific to depositional environment (for example, evaporation in lakes or incident solar heating of soils). If all T(Δ_{47}) values for a geologic formation are considered compromised by Δ_{47} alteration, a temperature estimate synthesized from past geochemical proxy-based studies of low-latitude Paleogene terrestrial temperatures is used for the $\delta^{18}O_c$-$\delta^{18}O_w$ calculation (see Discussion).

Modeling Solid-State Reordering of C—O Bonds in the Niubao Formation

We modeled possible Δ_{47} alteration by C—O bond reordering of the upper and middle Niubao Fm carbonates using the solid-state models of Lloyd (2020), following

after Stolper and Eiler (2015). For the upper Niubao Fm, we assumed a depositional temperature of 20 °C, similar to the measured $T(\Delta_{47})$ of the Dingqinghu Fm, and a depositional age of 40 Ma. We modeled linear burial of the oldest, and therefore stratigraphically lowest, carbonates to 95 °C (~3 km overburden), assuming that the main means of burial was deposition of younger Niubao sediments overtop older sediments rather than tectonics and an average geothermal gradient of 25°C/km, comparable with estimates used in other environmental reconstructions of the Lhasa terrane (for example, Leier and others, 2009; Orme, 2019). We considered steeper geothermal gradients of 30 and 40 °C/km for both the upper and middle Niubao Fms given modern observations of steep thermal gradients in certain regions of the Tibetan crust (for example, Shen, 1993). Using a 30 °C/km gradient, the model Δ_{47} range was within error for the upper Niubao Fm data but not for the middle Niubao Fm. The 40 °C/km geothermal gradient did not match the Δ_{47} measurements for either formation, indicating that a shallower geothermal gradient was more appropriate for this Eocene locality (fig. A3). The modeled time-temperature history for the upper Niubao Fm held the carbonates at the maximum temperature for 15 My during and after the deposition of the Dingqinghu Fm, and rapidly unroofed starting at 5 Ma. This burial history assumed no net denudation during the entire interval of Dingqinghu Fm deposition and, thus, likely overestimated the duration of maximum burial temperature and, in turn, the effects of solid-state reordering. Further, given the independent constraints on maximum temperatures lower than the oil window experienced by the underlying middle Niubao Fm (Polissar and others, 2009; Sun and others, 2014a; Ma and others, 2015), we were confident that this conservative burial history overestimated the impact of reordering on Δ_{47} in this sample set.

For the middle Niubao Fm, we modeled the most deeply buried carbonates held at the two end member possibilities for maximum temperatures—120 °C or 140 °C by 4 km of overburden with two plausible geothermal gradients and 60 °C by organic thermal maturation indices. In these model analyses, the lowermost middle Niubao Fm carbonates were linearly buried to the two endmember maximum temperatures over 15 My and held at maximum temperature for 25 My (an estimate of total duration of sedimentation preserved in the Lunpola basin), followed by linear, relatively rapid unroofing to modern surface temperature. No independent constraints exist from the Lunpola basin on the rate of sedimentation or timing of unroofing from low-temperature thermochronology or proprietary basin thermal models, as used in other solid-state reordering basin models (Ingalls, 2019; Lacroix and Niemi, 2019).

Stable Isotope Paleoaltimetry

Paleoelevations were calculated using a modified version of the theoretically derived Rayleigh distillation-elevation model of Rowley (2007), which fits a $\Delta(\delta^{18}O_w)$-elevation lapse rate statistical regression to observed relative humidity and precipitation isotopic composition data, found in Ingalls and others (2017) (Appendix). $\Delta(\delta^{18}O_w)$ is the difference in the stable isotopic composition of precipitation at the site of carbonate formation and at a coeval, low elevation site along the same mean storm trajectory. No coeval, unequivocally low elevation sections currently exist to the south of Lunpola basin for which to make a direct carbonate-derived $\delta^{18}O_w$ comparison. Instead, we used the value of $-6.0 \pm 1.6‰$ VSMOW for low elevation precipitation, comparable to modern precipitation in New Delhi today and more depleted than the average of $-3.6 \pm 1.6‰$ for all low latitude, low elevation stations monitored by the IAEA Global Network of Isotopes in Precipitation (Rowley and Currie, 2006). This approach is aligned with the assumption that the moisture source to the northern Lhasa terrane was from the south in the Eocene; however, uncertainties in moisture sources, amount, and recycling are the dominant contributors to the relatively large uncertainties in stable isotope paleoaltimetry elevation estimates (Rowley, 2007). The

use of a more ^{18}O-depleted low elevation $\delta^{18}O_w$ value than the modern both accounted for reduced lapse rates due to climate change since the Eocene and provided conservative elevation estimates, as the low elevation $\delta^{18}O_w$ value was closer to high elevation ^{18}O-depleted values. The 2σ paleo-elevation errors captured both the described model uncertainty and 2σ uncertainty on $T(\Delta_{47})$ propagated through the carbonate-water fractionation equations for calcite (Kim and O'Neil, 1997) and dolomite (Horita, 2014).

For samples in which lipid-$\delta D_{leafwax}$ data from Polissar and others (2009) was available to pair with $\delta^{18}O_c$ analyses from the same rocks, we used the evaporation-corrected isotopic composition of surface water, as described in Polissar and Freeman (2010), in the paleo-elevation model. Water δD (here, $\delta D\varepsilon_{a\text{-}corr}$) was calculated from plant-wax δD assuming an ε_a of $-121 \pm 10‰$ (Polissar and Freeman, 2010), as follows:

$$\delta D\varepsilon_{a\text{-}corr} = ((\delta D_{leafwax} + 1)/(\varepsilon_a + 1)) - 1 \quad (3)$$

In an attempt to correct for the effect of aridity on isotope values, we estimated original precipitation isotope values by applying a lake/leaf water evaporation line (LLEL) slope of 1‰δD/‰$\delta^{18}O$, empirically determined for mixed forest-shrub vegetation (Polissar and Freeman, 2010). We used the water isotopic compositions ($\delta D\varepsilon_{a\text{-}corr}$ and $\delta^{18}O_{LW}$) calculated from $\delta D_{leafwax}$ and $\delta^{18}O_c$ and the slope of the LLEL to calculate the LLEL intercept (b_{LLEL}) as follows:

$$b_{LLEL} = \delta D\varepsilon_{a\text{-}corr} - m_{LLEL}\delta^{18}O_{LW} \quad (4)$$

The evaporation-corrected $\delta^{18}O_w$ values were determined by the intersection of the LLEL projected from each data with the GMWL, as follows:

$$\delta^{18}O_{LW} = \frac{b_{LLEL} - b_{GMWL}}{m_{GMWL} - m_{LLEL}} \quad (5)$$

where the slope and intercept of the GMWL were 8 and 10, respectively (Rozanski and others, 1993). δD_w was calculated using the evaporation-corrected $\delta^{18}O_w$ and the GMWL equation. This method was employed to reconstruct primary isotopic compositions of the amount weighted mean precipitation in the basin catchment for lakes or on the basin floor for soils.

RESULTS

Microscopy and Alteration Assessment

Petrographic and crystallographic observations indicated preservation of primary micrite in the samples analyzed for stable isotopes. Grain diameters are predominantly <1 to 10 μm, rather than typically larger calcite spar domains. Further, we found that the micrite crystals retained primary "random" orientations of the crystallographic c-axis, as evidenced in the inverse pole figure (IPF) and pole figures, which plot the orientation of the c-axes, and the r {10-10} and a {11-20} planes (fig. A3). Recrystallization would result in a preferred "misorientation" axis, which would have resulted in a clear hotspot in the upper hemisphere pole figures (fig. A3; Shelley, 1993; Prior and others, 1999).

Oxygen and Carbon Isotopes

Carbon, oxygen, and deuterium stable isotope values of the Lunpola basin were reported in Rowley and Currie (2006) and Polissar and others (2009). $\delta^{13}C_{carb}$ and $\delta^{18}O_c$ of the Paleogene to Miocene carbonates analyzed for this study ranged from −8.2 to +2.5‰VPDB and −17.9 to −1.3‰VPDB (fig. 4), respectively (table A1). $\delta^{18}O_w$ values calculated from $\delta^{18}O_c$ of dolomites and calcites using the temperature-

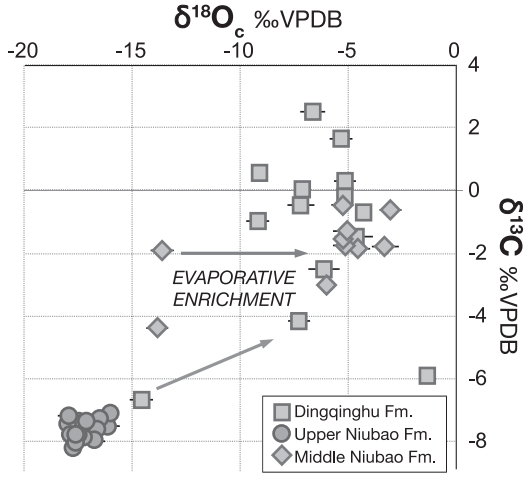

Fig. 4. Carbon and oxygen isotopic compositions with suggested evaporative overprinting. Dingqinghu and middle Niubao Fm carbonates are primarily lacustrine and upper Niubao Fm carbonates are pedogenic.

dependent fractionation equations from Horita (2014) and Kim and O'Neil (1997) ranged from −14.0 to +0.8‰VSMOW. The evaporation-corrected δD_w and $\delta^{18}O_w$ values ranged from −135 to −114‰VSMOW and −17.2 to −20.1‰VSMOW (fig. 5), respectively.

Clumped Isotope Thermometry

All nine clumped isotope samples from the Lunpola basin yielded $\Delta_{47,CDES,25}$ values of ~0.62 to 0.70. The average values for carbonate standards Carrara Marble

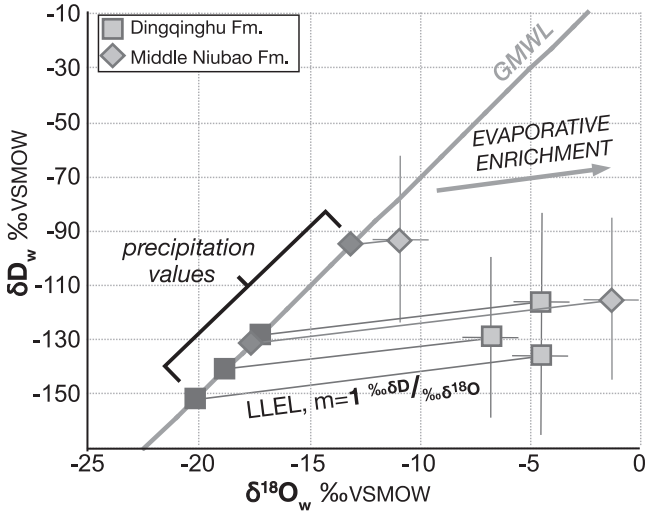

Fig. 5. Leaf wax-derived δD_w versus carbonate-derived $\delta^{18}O_w$ for Lunpola samples relative to the Global Meteoric Water Line. A conservative estimate of original precipitation compositions are calculated using a local evaporation line (LEL) with a slope of 1 (Polissar and others, 2009; Polissar and Freeman, 2010). Data falling to the right of the GMWL are measured values; darker points are evaporation-corrected precipitation values.

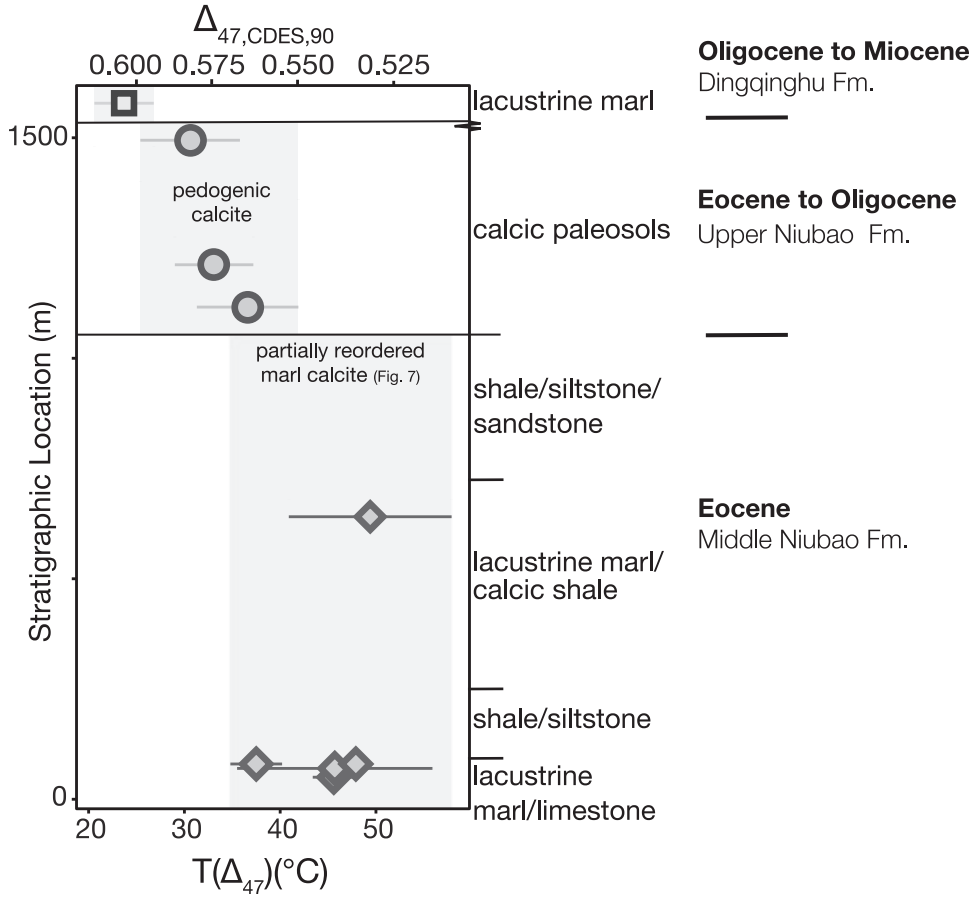

Fig. 6. $\Delta_{47,CDES,90}$-derived temperatures calculated using the T-Δ_{47} relationship of Bonifacie and others (2017) plotted by lithology and age.

and TV04 were 0.404 ± 0.014 (n = 4) and 0.650 ± 0.008 (n = 4), respectively. All clumped isotope results, including samples, standard carbonates, and equilibrated and heated gases, can be found in tables A2, A3, A4 and A5, http://earth.geology.yale.edu/%7eajs/SupplementaryData/2020/Ingalls.

Lacustrine marl 299B from the Dingqinghu Formation yielded a $T(\Delta_{47})$ of 23.7 ± 3.1 °C (n = 3, where n is the number of replicates per sample; fig. 6). The average $T(\Delta_{47})$ of three soil carbonates (n=3 to 4 each) from the upper Niubao Member was 33.4 ± 4.8 °C. The average of five middle Niubao Member lacustrine carbonates was 45.3 ± 6.7 °C (n = 2 to 4). Interpretation of the relative primacy versus diagenetic overprinting recorded by these clumped isotope values can be found in the discussion.

C—O Bond Reordering Models

Under the set of conditions applied for the upper Niubao burial history, the model mean predicted that $T(\Delta_{47})$ of upper Niubao Fm carbonates should not have altered from the depositional value (that is, Earth surface temperature; fig. 7). The 1σ model uncertainty under these depositional and burial conditions allowed for an increase in $T(\Delta_{47})$ to just over 30 °C, coincident with the measured $T(\Delta_{47})$ values of the

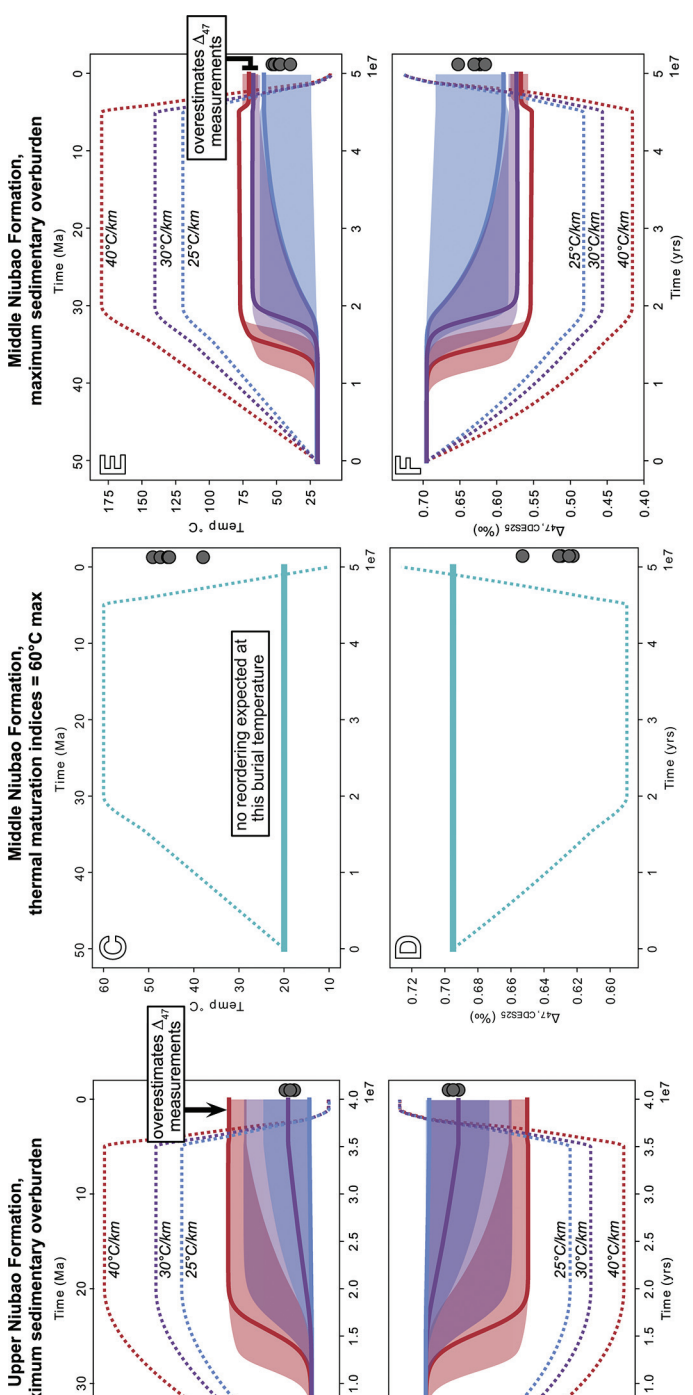

Fig. 7. Solid-state reordering modeling following Stolper and Eiler (2015) with revised T-Δ_{47} relationship (Bonifacie and others, 2017) and ^{17}O parameters (Brand and others, 2010). (A-B) The upper Niubao Fm is linearly buried assuming maximum sedimentary overburden of overlying formations of 3 km. (C-D) Maximum burial temperature for the middle Niubao Fm taken from organic thermal maturation indices. (E-F) Linear burial of the middle Niubao Fm assuming maximum sedimentary overburden from overlying formations of 4 km. The maximum overburden scenarios consider 3 potential geothermal gradients. Duration at maximum burial temperature is based on stasis at that temperature during all subsequent sedimentation preserved in the Lunpola basin, and is thus likely an overestimate.

upper Niubao pedogenic carbonate nodules. However, given the conservative nature of the burial history used and that the strength of the model is in the model mean, which predicts no change in Δ_{47}, we found that very minimal reordering should have occurred in the upper Niubao Fm.

No solid-state reordering was predicted during burial of the middle Niubao Fm to only 60 °C (figs. 7C-7D). However, under the overburden-constrained conditions, $T(\Delta_{47})$ was predicted to reequilibrate to ~50 to 60 °C, exceeding our measured $T(\Delta_{47})$ values (figs. 7E-7F). Because the measured $T(\Delta_{47})$ from the middle Niubao Fm carbonates are lower than expected $T(\Delta_{47})$ based on 25 My of burial by ~4 km of sediment, the rate of denudation and tilting during and prior to the formation of the unconformity between the Niubao and Dingqinghu Formations may have outpaced sedimentation. Therefore, the middle Niubao would have never experienced overburden of the entire >4 km package preserved in the Lunpola basin. However, the elevated $T(\Delta_{47})$ of the middle Niubao do not record primary Earth surface conditions and therefore were not used in calculations of $\delta^{18}O_w$.

DISCUSSION

Evaluation of Syn- and Post-depositional Isotopic Values

Oxygen isotopes of carbonate minerals record higher and lower values than primary meteoric water by (1) evaporation of the water from which the carbonate precipitated and (2) water-rock exchange with diagenetic fluids. In this work, we screened for both means of $\delta^{18}O$ alteration and/or corrected for these effects where possible.

Water-rock recrystallization and solid-state ^{13}C–^{18}O reordering.—Recent work highlighted the challenge of extracting primary Paleocene-Eocene environmental and climatic information from a carbonate record that has been compromised by collision zone tectonics (Quade and others, 2020). Quade and others (2020) asserted that it was impossible to sub-sample primary micrite and sparite (which could have formed under hydrothermal conditions) for stable isotope analyses. As such, they suggested that all published carbonate stable isotope measurements from the Indus-Yarlung Suture Zone represented mixtures of carbonate material having experienced varying degrees of open-system oxygen isotope exchange and should be considered suspect. However, Ingalls and others (2017) and Ingalls (2019) demonstrated that careful petrography (optical and cathodoluminescent, with the addition of EBSD in the present study) allows for the identification and micro-milling of discrete micritic and sparry fabrics that yielded $\delta^{18}O_c$ and Δ_{47} data populations that are consistent with unaltered and altered compositions, respectively. These unique textures and isotope data were interpreted as records of primary versus late stage diagenetic events from some of the same stratigraphy called into question in Quade and others (2020).

Although petrographic and crystallographic observations of the Lunpola basin samples indicated preservation of micrite in the samples used for stable isotope paleoaltimetry, we considered the trends preserved in the bulk stable isotopic values of all carbonates sampled within the Lunpola basin strata. Recrystallization during early or late burial diagenesis can alter the depositional oxygen isotope composition of a carbonate due to exchange of carbonate oxygen with diagenetic fluids (Drever, 1982; Berner, 1988; Budd and Land, 1990; Veizer and Mackenzie, 2003; Swart, 2015; Quade and others, 2020). This water-rock reaction is recorded in the recrystallized material by a $\delta^{18}O$ value shifted towards the composition of the diagenetic water (typically lighter). Isotopic exchange in a high W:R system is expected to collapse primary $\delta^{18}O_c$ variability (such as $\delta^{18}O_c$ variation in the middle Niubao lacustrine carbonates) to a homogeneous value towards that of the diagenetic fluid (Banner and Hanson, 1990; Huntington and others, 2011; Huntington and Lechler, 2015). Although the middle

Niubao samples yielded relatively high $T(\Delta_{47})$, the primary $\delta^{18}O_c$-$\delta^{13}C_c$ correlation and variability due to the original closed-basin lake hydrology was preserved within the measured samples. Therefore, we interpreted the low Δ_{47}-high $T(\Delta_{47})$ values to be the result of partial reordering of the C-O bonds within the calcite lattice rather than water-facilitated oxygen isotope exchange.

In highly rock-buffered systems (low water-rock ratio), carbonate minerals can retain a nearly primary $\delta^{18}O_c$ composition at elevated temperatures because there is little to no water to facilitate oxygen exchange (Banner and Hanson, 1990). However, in the absence of water-facilitated recrystallization, solid-state reordering of the C-O bonds within the carbonate crystal lattice can occur via diffusion, randomizing the distribution of ^{13}C-^{18}O pairs, thereby altering Δ_{47} to lower values (Passey and Henkes, 2012; Stolper and Eiler, 2015).

The Lunpola basin preserves >4 km of stratigraphy, with a significant amount likely missing locally at the unconformity between the upper Niubao Fm and the Dingqinghu Fm. The overburden alone could have buried the lowermost middle Niubao Fm carbonates to ~120 to 180 °C. However, burial temperatures of the most deeply buried samples of the middle Niubao Fm have been assessed using thermal maturation indices (Polissar and others, 2009; Sun and others, 2014; Ma and others, 2015). Based on these burial temperature proxies, the middle Niubao is immature, indicating it did not cross into the oil window and thus unlikely to have experienced burial temperatures >60 °C—a critical window at the lower limit of solid-state reordering (~75 °C; Stolper and Eiler, 2015).

We determined that no solid-state reordering of C—O bonds was expected when the Stolper and Eiler (2015) model was employed within the framework of the described burial pathway to the maximum temperature predicted by organic maturation indices (figs. 7C-7D) for the middle Niubao Fm. Under conditions of maximum sedimentary burial, reaching temperatures from 120 to 180 °C depending on the geothermal gradient applied, partial reordering of C—O bonds was predicted, yielding model means from ~50 to 70 °C (figs. 7E-7F). Because the middle Niubao $T(\Delta_{47})$ values fell between these endmember solutions, the total overburden heating experienced by the middle Niubao Fm was likely sufficient to partially reorder carbonates in the more deeply buried parts of the Lunpola basin. Irrespectively, the elevated $T(\Delta_{47})$ of the middle Niubao do not reflect primary Earth surface conditions and therefore were not used in calculations of $\delta^{18}O_w$.

Overall, clumped isotope-derived temperatures of the upper Niubao and Dingqinghu Fms and SEM-EBSD crystallographic analyses of the middle Niubao Fm were not indicative of water-rock alteration during high-temperature burial diagenesis, and therefore we accepted the bulk stable isotopic compositions ($\delta^{18}O_c$) of the samples from those two formations as recorders of effectively primary depositional conditions.

Syn-depositional isotopic effects.—While carbon isotope values are not directly used in stable isotope paleoaltimetry calculations, these values can be useful in screening for isotopic effects of formational and secondary processes. $\delta^{13}C_c$ primarily reflects $\delta^{13}C$ of the dissolved inorganic carbon (DIC) of the water from which carbonate precipitates. DIC changes with climatic ($\delta^{13}C$ of atmospheric CO_2; Mills and Urey, 1940; Vogel and others, 1970; Zhang and others, 1995; Myrttinen and others, 2012; Zeebe, 2014) or local biological (for example, microbial respiration or biomineralization; Mortimer and Coleman, 1997; McConnaughey, 2003; Gérard and others, 2013; Thaler and others, 2017) processes. Thus, an evolving DIC pool can be indicative of overprinting of primary isotopic values, thereby allowing the use of $\delta^{13}C_c$ as an indicator of early diagenesis. Additionally, positive covariation of carbon and oxygen isotope values can signify an evaporative overprint of primary meteoric water isotopic values in a closed-

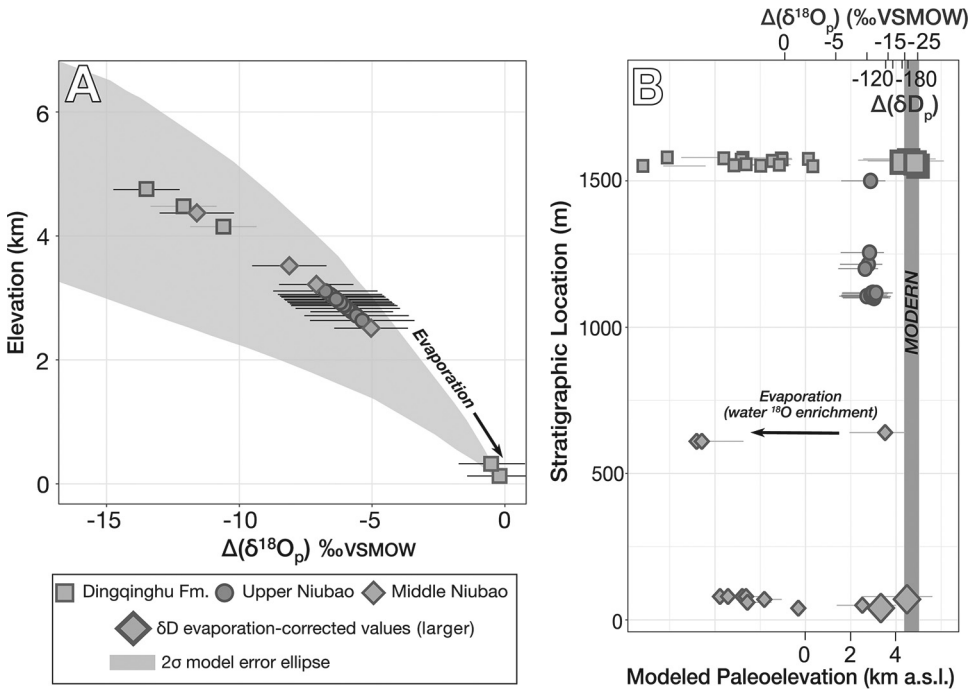

Fig. 8. (A) Elevation reconstruction of the Lunpola basin. The Dingqinghu Formation $\delta^{18}O$ values are evaporatively enriched, leading to higher $\Delta(\delta^{18}O_w)$ values. The upper Niubao Formation preserves the isotopic composition of high elevation precipitation within pedogenic carbonates. (B) Modeled paleoelevations with samples plotted by location in section. The larger symbols represent the evaporation-corrected values based on paired $\delta^{18}O$-δD measurements. The $\Delta(\delta^{18}O_w)$ scale was projected to $\Delta(\delta D_w)$ space using the GMWL.

basin lake, which leaves an apparent enrichment of ^{18}O (Craig and others, 1963) and ^{13}C in carbonate-saturated waters (Leng and Marshall, 2004; fig. 4).

A subset of samples from the Miocene and Eocene units (Dingqinghu and middle Niubao Formations) of the Lunpola basin have experienced extensive evaporative ^{18}O-enrichment (figs. 5 and 8). The magnitude of variation in the carbon and oxygen isotopic compositions of carbonates from these formations likely does not record precipitation compositions over the watershed. We interpreted the isotopic variability to have recorded unique oxygen and DIC compositions of evolving water bodies based on the relative amount of evaporation within the soil porewater or lake water. Independent assessment of the environmental conditions associated with the lacustrine sequences using biomarkers have been interpreted to imply deposition in relatively deep, stratified lakes. Middle and upper Niubao biomarker assemblages are consistent with an increase in humidity relative to older Niubao sequences (Wei and others, 2017).

In contrast, the $\delta^{13}C$ and $\delta^{18}O$ values from the Oligocene upper Niubao Fm were tightly clustered, and therefore more likely to represent isotopic compositions of minerals in equilibrium with meteoric water and considered representative of the environmental and climatic conditions of the depositional environment. Polissar and others (2009) directly screened for evaporative effects in a subset of the samples presented in this study by measuring deuterium and oxygen isotopes from lipids and carbonate, respectively, from the same samples. We used the measured $\delta^{18}O_c$ values for

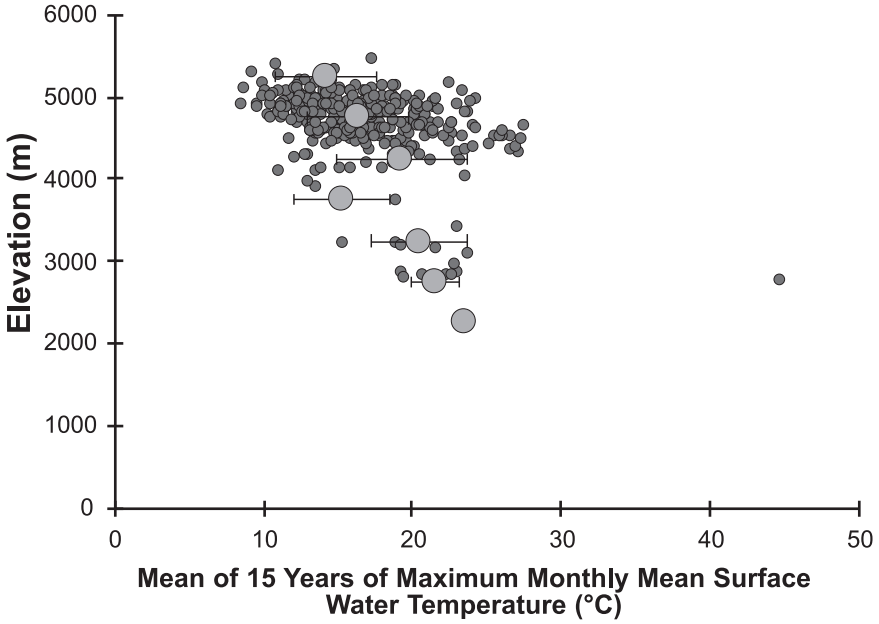

Fig. 9. Modis-derived lake surface water temperatures of 374 Tibetan lakes at varying altitudes from 2001 to 2015 (Wan and others, 2017). Small circles are the mean maximum monthly surface water temperatures ($\pm 1\sigma$) in 15-year bins plotted by lake elevation. Large circles further bin the lake water temperatures in ±250m elevation bins. Note the lowest bin at 2250 m has only a single value and the mean and standard deviation at 2750 m excludes the clear outlier of Gansenquan Lake in the Qaidam Basin (Lake ID=105 in the Wan and others, 2017 dataset).

all samples in our paleo-elevation calculations, but focused our interpretations on the samples interpreted to reflect primary depositional conditions.

Comparison of lacustrine carbonate clumped isotope-derived temperatures with modern Tibetan lakes.—To place the temperatures in better context, we compared the clumped-isotope derived temperatures from the Dingqinghu and middle Niubao lacustrine carbonates to surface water temperatures of modern Tibetan lakes. We used the monthly mean surface water temperature data set compiled by Wan and others (2017) using MODIS (Moderate Resolution Imaging Spectroradiometer) data from 2001 to 2015. We extracted the maximum mean monthly temperature for each year for each lake with a surface area exceeding 10 km^2 (n = 374) and then calculated the mean of those temperatures over the 15-year study (fig. 9; table A6). Based on contemporaneous satellite-derived temperatures and *in situ* measurements in two Tibetan lakes, Ngoring and Gyaring, the surface layer temperature should correspond to at least the top 0.6 m of the water column (Kirillin and others, 2017). For the purposes of our comparison, we assumed that micrite mostly precipitates during the warmest months and that there was close correlation between the MODIS-derived surface water temperature and the water above the thermocline from which carbonates precipitate.

The individual lake maximum monthly mean temperatures were quite scattered with no clear trend of temperature as a function of elevation (fig. 9). However, a trend emerged with a corresponding mean surface lapse rate of ~ -2.8°C/km when the data were binned into ±250 m elevation ranges. Carbonate mineral precipitation does not take place precisely at the lake surface where MODIS temperature estimates are derived so it is likely that these water temperatures represent a warm bias. The mean maximum monthly temperature at 4250 m, comparable to the modern Lunpola basin,

was ~19.3 ± 4.4 °C with a maximum value in excess of ~30 °C. Put into this context, the 23.7 ± 3.1 °C from the Dingqinghu Fm was well within this scatter, independent of any long-term Oligocene to Present change in global mean temperatures. However, the $T(\Delta_{47})$ of 45.3 ± 6.7 °C from the middle Niubao lacustrine carbonate would clearly be an outlier at present, and likely an outlier in the late Eocene, even accounting for climate cooling since that time. Soils and lake surface waters are not directly comparable so it is not clear that a comparison should be made between these data and the upper Niubao clumped isotope-derived temperature of 33.4±4.8 °C. The warmest maximum monthly mean temperature according to Wan and others (2017), excluding Gansenquan Lake, was also in the Qaidam basin with a temperature of 36.1 °C at ~2900 m. Lakes above 4000 m reached maximum temperatures of about 32 °C (Wan and others, 2017). Given a warmer late Eocene to Oligocene, it is possible that the upper Niubao $T(\Delta_{47})$ values recorded surface temperatures even at quite high elevation.

Interpreting Oligocene to Miocene $T(\Delta_{47})$ Based on Lithology

The environmental conditions under which different terrestrial carbonate lithotypes (for example, pedogenic nodules or lacustrine mudstone) form must be carefully considered when interpreting $T(\Delta_{47})$ estimates. For example, empirical calibrations have found that Holocene to modern lacustrine carbonates record Δ_{47} temperatures in agreement of mean annual temperature (MAT; Hudson and others, 2017) or summertime warm month mean temperature (WMMT; Huntington and others, 2015). The Dingqinghu Fm $T(\Delta_{47})$ of ~24 °C fell within the range of mean maximum monthly surface water temperatures for modern Tibetan lakes at the altitude of Lunpola basin. We interpreted the Dingqinghu lacustrine limestones as having formed during the warmest months of the year and thus recorded $T(\Delta_{47})$ approximating WMMT.

The climatic information recorded by soil carbonate Δ_{47} is contentious due to the variability of soil carbonate growing season. Breecker and others (2009) found that Δ_{47} of soil carbonates record a WMMT or warmer bias. However, Peters and others (2013) and Burgener and others (2016) have demonstrated that whether soil carbonate growth season, and in turn, whether Δ_{47} records WMMT or MAAT, depends on both elevation and precipitation type (rain or snow). Further, the timing of soil carbonate formation has been linked to periods of low soil moisture content (Gallagher and Sheldon, 2016; Ringham and others, 2016), often in the early stages of soil drying after large precipitation events when soil pCO_2 is lowest. Thus, the timing of soil carbonate formation can be strongly influenced by the timing of annual monsoons (winter or summer). On the Tibetan Plateau, the monsoon season and its associated drying events occur during the warmest summer months, and thus likely record the warmest days of the year.

Using a combination of temperature estimates from clumped isotope and leaf margin analysis with climate models, Snell and others (2013) found that Paleocene-Eocene mid-latitude, terrestrial soil carbonates recorded $T(\Delta_{47})$ ~18 °C warmer than MAAT, and 3 to 5 °C warmer than mean summer air temperature (Hough and others, 2014). Further, the extent of radiant solar heating of the ground can significantly increase $T(\Delta_{47})$ values (Breecker and others, 2009; Quade and others, 2013). The soil carbonate nodules collected for the present study were extracted from paleo-horizons ~>50 cm below the soil-air interface, within the soil depth range impacted by incident heating (Hillel, 1982). Therefore, we interpret the late Eocene to Oligocene upper Niubao soil carbonate $T(\Delta_{47})$ values of ~30 to 36 °C as the maximum possible surface temperatures when soil carbonates formed after the summer Asian monsoons.

Solid-state reordering due to sedimentary overburden of up to 3 km could potentially have increased measured $T(\Delta_{47})$ values in the upper Niubao Fm carbon-

ates. However, based on current understanding of the kinetics of solid-state reordering at relatively low burial temperatures, and plausible geothermal gradients of 25–30°C/km, the upper Niubao Fm Δ_{47} values fall within the range of model uncertainty of little to no predicted reordering (figs. 7A-7B). Prolonged burial to temperatures >100 °C was required to yield a model mean in agreement with the 30 to 36 °C T(Δ_{47}) range of the upper Niubao Fm. This scenario is unlikely given that heating was not sufficient to significantly mature the organics preserved in the Niubao Fm (Polissar and others, 2009), and thus we preferred the interpretation of the upper Niubao Fm as recorders of well preserved Δ_{47} values reflecting a seasonal bias of soil carbonate formation.

At present, solid-state reordering kinetics are estimated at such low temperatures by assuming a linear Arrhenius slope from higher experimental temperatures (Stolper and Eiler, 2015), which contributes significant uncertainty to solid-state reordering under shallow burial conditions. As such, further work on C–O bond reordering behavior at shallow burial temperatures may change the present interpretation, and thus, we considered possible $\delta^{18}O_w$ and elevations using both the measured soil carbonate T(Δ_{47}) and the Dingqinghu Fm T(Δ_{47}) with the upper Niubao $\delta^{18}O_c$ values.

Finally, the aforementioned seasonality of pedogenic carbonate formation results in a separate issue in using T(Δ_{47}) and $\delta^{18}O_c$ of a pedogenic carbonate nodule to reconstruct paleo-meteoric $\delta^{18}O_w$. By nature of pedogenic carbonate formation during soil drying periods, a soil $\delta^{18}O_w$ pool would evolve towards higher $\delta^{18}O_w$ values as drying and soil carbonate formation progresses. As such, soil carbonate nodules can record heterogeneous $\delta^{18}O_c$ compositions trending towards values more ^{18}O-enriched than meteoric precipitation $\delta^{18}O_w$ (Cerling and Quade, 1993; Gallagher and Sheldon, 2016). As such, the measured $\delta^{18}O_c$ compositions and calculated $\delta^{18}O_w$ values from the upper Niubao Fm pedogenic carbonates could record more ^{18}O-enriched compositions than primary meteoric water at the time of deposition, and thus, underestimate paleo-elevations when the isotopic lapse rate is applied.

A Low-latitude, Terrestrial Temperature Estimate for the Paleogene

There is little to no evidence of open-system water-rock alteration of the middle Niubao Fm carbonates, and thus the $\delta^{18}O_c$ values are interpreted as a record of primary meteoric composition. However, the T(Δ_{47}) range of the middle Niubao Fm lacustrine facies exceeded plausible Earth surface conditions indicative of closed-system partial C—O solid-state reordering to higher apparent T(Δ_{47}). Therefore, we did not use the T(Δ_{47}) measurements from the middle Niubao Fm as our Paleocene to Eocene environmental temperature. Instead, we considered existing reconstructions of terrestrial temperatures from carbonate clumped isotopes to allow for conservative estimates of paleo-meteoric water and elevations.

We considered the depositional environment, age, and paleo-latitude of each study site to most closely match the paleogeographical and depositional conditions of the Paleogene Lunpola basin. Depositional age constraints for the middle Niubao Fm were limited due to the discrepant ages of the lowermost Dingqinghu Fm by bio- and magnetostratigraphy. We determined a reasonable estimate of the paleo-latitude of the Lunpola basin at ~40 Ma of 26 ± 5°N based on strain partitioning between Greater India and Greater Tibet and the global apparent polar wander path of Rowley (2019). We focused on comparison sites with lacustrine carbonate deposits to most closely match the dominant lithofacies of the middle Niubao Fm. Finally, due to seasonality of lacustrine carbonate formation (Huntington and others, 2015; Petryshyn and others, 2015), we considered that the middle Niubao Fm $\delta^{18}O_c$ values likely recorded carbonate precipitation in equilibrium with waters at MAT or warmer, but not as warm as pedogenic carbonates of the same age (Snell and others, 2013).

First, we considered a paleosol record from the Bighorn Basin (Paleocene-Eocene paleo-latitude, ~50°N; Wing and Currano, 2013) of Wyoming, USA. Soil carbonate

nodules yielded a warm month maximum temperature (WMmaxT) range of 31 to 35 °C, with an estimated MAT ~18 °C cooler than the WMmaxT, or 13 to 17 °C (Snell and others, 2013). At > 20° north of the Eocene Lunpola basin, applying a temperature lapse rate of −0.4°C/°latitude (Fricke and Wing, 2004) yielded a range of ~22 to 27 °C for potential MAT of the Lunpola basin.

Next, we considered the lacustrine carbonate clumped isotope record of the geographically and altitudinally similar late Eocene Nangqian basin of the eastern Tibetan Plateau. The paleo-geographic similarities of the two basins allowed for the most comparable environmental conditions based on latitude and regional climate effects due to atmospheric circulation patterns over the Asian continent. Lacustrine carbonates from the Nangqian basin yielded $T(\Delta_{47})$ values of ~30 °C (Li and others, 2019).

Allowing for the full range of compiled temperatures calculated for ~26 ± 5°N, we used 26.5 ± 3.5 °C to calculate $\delta^{18}O_w$ from $\delta^{18}O_c$ for the middle Niubao Fm, favoring the warmer temperatures as more likely representative of terrestrial Tibetan Plateau conditions. Further, we acknowledged that because this is not a direct measurement of carbonate growth temperature from the middle Niubao Fm, the uncertainties in middle Niubao Fm elevation estimates were greater.

Early Eocene to Miocene Paleo-elevations of the Northern Lhasa Terrane and Timing of Peneplanation

The modern Lunpola basin is located at ~4.7 km above sea level (a.s.l.). Here we present our calculated paleoelevation estimates for the three stratigraphic intervals of the Lunpola basin. We used the evaporation-corrected $\delta^{18}O_w$ values (fig. 5) for the three Oligo-Miocene Dingqinghu Fm samples, as they were least affected by evaporative enrichment of the heavy isotopes, to calculate $\Delta(\delta^{18}O_w)$ and elevations of $4150^{+1154}/_{-1821}$ to $4757^{+1351}/_{-2005}$ meters (fig. 8; table A1). The elevation from the most ^{18}O-depleted upper Niubao sample was $3111^{+739}/_{-1401}$ meters using the $T(\Delta_{47})$ value of 36.6 °C from the pedogenic carbonate nodules. However, as previously discussed, this value likely recorded the warmest and wettest surface conditions of the year, and under the most liberal burial scenarios, these samples may have experienced partial solid-state reordering. As such, we also paired the upper Niubao Fm $\delta^{18}O_c$ values with the lacustrine carbonate-derived $T(\Delta_{47})$ of 23.7 °C from the Dingqinghu Fm, which may better represent late Paleogene meteoric temperatures, and yielded a maximum paleo-elevation of $3823^{+1025}/_{-1699}$ meters for the upper Niubao Fm. Although the two model elevation means were highly contingent on the assumed or measured paleo-temperatures used to calculate $\delta^{18}O_w$ from $\delta^{18}O_c$—temperatures which presumably represent plausible interannual conditions within the Lunpola basin and $\delta^{18}O_c$ values that may be higher than meteoric composition due to soil drying—the two calculated elevations were within model uncertainty of each other regardless of which clumped isotope temperature was applied to the oxygen isotope data. Further, both clumped isotope-derived model mean elevations are within model uncertainty of the ~4850 $^{+1630}/_{-1435}$ meters reconstructed in Rowley and Currie (2006) using an assumed temperature range of 10 ± 10 °C and the same $\delta^{18}O_c$ values of the upper Niubao Fm used in this study. However, the agreement between Rowley and Currie (2006) and our estimates is only permissible due to the inherently large uncertainties on our model estimates; the model mean elevations calculated using $T(\Delta_{47})$, and thus a more direct measure of carbonate formation conditions, were a kilometer or more lower than the reconstructed elevation of ~4850 m in Rowley and Currie (2006). Thus, we favored the more conservative elevation estimate of 3.8 ± 1 km a.s.l. for the Oligocene Lunpola basin. Finally, we used the temperature estimate of 26.5 ± 3.5 °C and an evaporation-corrected value for the Eocene middle Niubao Fm to yield an elevation of $4372^{+1234}/_{-1895}$ meters (fig. 8).

Our findings agreed with the current tectonic model that the central Tibetan Plateau (Lhasa and Qiangtang terranes) reached relatively high elevations (>3 to 4 km a.s.l.) sometime prior to the late Eocene (~40 Ma). However, existing data did not permit an assessment of whether this uplift occurred before, synchronous, or after the southern Tibetan Gangdese Range.

The active tectonic state of the Lhasa block, which has accommodated collision-related strain for the last 56 ± 2 My (DeCelles and others, 2014), complicates preservation of primary sediments by burial diagenesis or wholesale elimination of strata by faulting and/or erosion. As such, reconstructions are limited by location and stratigraphic exposure of Cenozoic depocenters and preservation of primary material within active basins. Out of necessity, we must extrapolate from "postage stamp"-sized records to model the elevation distribution across a much larger geologic terrane. Misinterpretations of the primacy of proxy materials and measurements have led to potentially erroneous tectonic models (Wei and others, 2016); however, our ability to extrapolate and reconcile interpretations from different sedimentary basins is aided by the lateral extent of lacustrine facies across the Tibetan Plateau in the Cenozoic. Wu and others (2014) favor a model in which the plateau uplifted by the Oligocene and formed an extensive lake system by the early Miocene. In the Wu and others (2014) model, the majority of the Tibetan Plateau was covered in a series of interconnected lake basins linked by water passages separated by mountain ranges during the Late Oligocene to Early Miocene. The nearly continuous lateral cover of lacustrine facies by the Oligocene indicated that the Lhasa terrane was internally drained and at approximately equal elevation by this time (Wu and others, 2008; Wu and others, 2014).

Hetzel and others (2011) and Haider and others (2013) have argued that a peneplanation surface exposed in the vicinity of Baingoin, ~50 km south of the Lunpola basin, constrains the topographic evolution of this part of the Tibetan Plateau. Both studies dated primarily plutonic rocks of Early (*ca.* 118 Ma) and Late Cretaceous (*ca.* 85 Ma) age using U/Pb zircon dating and determined shallow crustal thermal evolutions using ZHe, AFT, and AHe dating. The low-temperature thermochronometers indicated rapid exhumation of these plutons within the interval from ~75 Ma to ~50 Ma to near surface conditions by ~45 Ma, followed by little to no significant change in temperature. According to the mean AFT and AHe ages of these plutonic rocks, the peneplain surface primarily post-dates ~55 Ma and was clearly in place at the time of deposition of the Eocene red beds in the Baingoin area equivalent to the Niubao Fm.

Haider and others (2013) argued that peneplanation occurred near sea level based on Tibetan derived detritus found in Eocene age sediments of the Bengal Basin associated with the exhumation of this surface. However, base level does not constrain the elevation of the peneplain surface. For example, the modern base level is sea level for the externally drained parts of Tibet while the internally drained Tibetan Plateau is >4 km a.s.l. In addition, the red beds that nonconformably onlap the peneplain surface are correlative with the Niubao Fm from which our high altitude paleoaltimetry estimates were derived from. Thus, the onlapping relationship of the ~4 km a.s.l. Niubao correlative sediments on the red beds implies quite high paleo-elevations for the surface of peneplanation.

A similar unconformity, the Maqu unconformity (England and Searle, 1986) beneath the Linzizong arc, is widely distributed in the southern Lhasa block. This unconformity is overlain by the latest Maastrichtian to Paleocene (~60 Ma) (Zhu and others, 2019) Dianzhong and overlying Nianbo Formations from which recent paleoaltimetry results suggested deposition at >4 km a.s.l. (Ingalls and others, 2017). If the regional peneplanation surface formed at low elevations during Late Cretaceous to Paleocene time, then ~4 km of uplift would be required between peneplanation and

55 Ma in the south (Ingalls and others, 2017) and ~>40 Ma in northern Lhasa block, based on this study. As such, we interpreted that peneplanation occurred at relatively high elevation prior to the deposition of the Nianbo and Niubao Fms nonconformably on top of the peneplain surface.

Comparison to Previous Northern Lhasa Terrane Studies

The addition of paleo-temperature constraints to the stable isotope paleoaltimetry calculations first presented in Rowley and Currie (2006) and Polissar and others (2009) enabled more robust comparisons of our paleo-elevations to those in previous studies from the northern Lhasa terrane. In doing so, we found that our paleo-elevations from the Eocene and Miocene are still in agreement with the original reconstructions from Rowley and Currie (2006). Although the elevations of the presently studied formations agreed within uncertainty, the lower limits of the elevation estimates from the upper Niubao Fm pedogenic carbonates aligned with the lower elevation estimates from other palynological, paleobotanical, and paleontological proxies (for example, Tao and others, 2012; Sun and others, 2014b), and revealed that the mean elevation of the Oligocene Lunpola basin may have been ~1 km lower than previous stable isotope-based estimates suggested. The addition of primary carbonate formation temperatures brought discrepant results from otherwise unrelated proxies into better agreement. However, we did not extract sufficient lipid material from the upper Niubao Fm for $\delta D_{leafwax}$ measurements, which could facilitate an assessment of the agreement between δD_w- and $\delta^{18}O_w$-based elevation estimates, or in the case of disagreement, application of an evaporation correction. Coexistence of higher $\delta D_{leafwax}$ and $\delta^{18}O_c$ values relative to the Lower Niubao and Dingqinghu Fms would further support that the Lunpola basin experienced a period of subsidence in the late Eocene-Oligocene. "Low" $\delta D_{leafwax}$ paired with "high" $\delta^{18}O_c$ values would suggest that the lacustrine carbonates have been evaporatively enriched in ^{18}O and our $\delta^{18}O$-based paleoaltimetry calculations, presented here, were a minimum paleo-altitude for the late Eocene-Oligocene Lunpola basin.

The new information provided by our temperature estimates brought most of the ecosystem arguments for low elevation into agreement with our reconstruction. Many of the palynological and paleobiological arguments for low altitude were founded on temperature sensitivities rather than altitude sensitivity. The warm month temperatures from our reconstruction indicated an annual range that was likely suitable for the fossil flora and fauna found in the Oligocene to Miocene strata. For example, although Wu and others (2017) asserted that fossil palms, golden rain trees, and climbing perch (*Eoanabas thibetana*) from the Nima and Lunpola basins required that these basins were only ~1 km a.s.l. during the Oligocene, our data demonstrated that the Lunpola basin was both warm and at high elevation at that time. These flora and fauna were more sensitive to temperature and humidity conditions than altitude (Peppe and others, 2011; Peppe and others, 2018), and thus, our warm $T(\Delta_{47})$ values eliminated the incompatibility of the ecosystem and stable isotope interpretations. The *Eoanabas thibetana* described by Wu and others (2017) are from the same sections from which DeCelles and others (2007b) and Huntington and others (2015) reported depleted $\delta^{18}O_c$ compositions and mostly warmer $T(\Delta_{47})$ (>40 °C), although one sample yielded a $T(\Delta_{47})$ of 30 °C. Deng and Jia (2018) reported a very low δD_{lipid} value ($-222‰ \pm 12‰$) from the same section as the carbonates with limited thermal maturation. Wu and others (2017) did not attempt to reconcile these disparate results. Based on extant relatives of the climbing perch in west Africa, the optimal water temperature range for perch is 18 to 30 °C—within the range of both the WMmaxT from our pedogenic $T(\Delta_{47})$ and the calculated MAT range from the same measurements. Similarly, a fossil pollen shift to mixed-coniferous forest in the Oligocene (Sun and others, 2014) was in

agreement with regional cooling from the time of deposition of the upper Niubao to the Dingqinghu Fms.

Similarly, Su and others (2019) described fossil palm leaves from the Lunpola basin, first reported by Wu and others (2017), to estimate a maximum elevation of no more than 2.3 km for the Dingqinghu based on NLR temperatures and climate model estimates of local terrestrial lapse rates. Su and others (2019) attempted to reconcile associated isotopic data with the NLR analysis by suggesting that isotopic compositions reflected nearby upland sources whereas the palms represented valley bottoms. However, deep fine-grained siliciclastic and carbonate sediment-dominated lake systems similar to those recorded by the Dingqinghu and middle Niubao Fms are not typical of thrust-loaded basin settings as envisioned by Su and others (2019). Further, isotopic compositions reflect the precipitation-amount weighted-mean elevation, which tends to be more similar to the basin floor than the heights of the adjacent uplands (Rowley, 2007). Added to this, calculated δD_w and the lowest $\delta^{18}O_c$ values of Lunpola basin strata fell close to the GMWL and hence recorded the same precipitation source compositions, which would be highly unlikely if the basin and its vegetation were at one elevation and the riverine source of the lake was at much higher elevation. Finally, the paleotemperatures of 30 to 36 °C presented for the upper Niubao Fm reconcile the NLR analyses for fossil palms with higher, warmer paleoelevations.

The discovery of a rhinocerotid fossil at ~18 to 16 Ma was used to assign a maximum elevation limit of 3 km a.s.l. by Tao and others (2012). Given the age uncertainty of Lunpola strata and the time required for substantial uplift and environmental succession to occur, we considered the range limit of ~3 km a.s.l. to be an assertion rather than a basis by which to benchmark our elevation reconstruction. Additionally, other large mammals, such as *Bos mutus* (wild yak), have adapted to living at modern elevations exceeding 4 km on the Tibetan Plateau. In summary, we found the existence of both the fossil fish and tropical flora to not be discordant with our Oligocene environmental reconstruction of ~3.8± 1 km elevation and air temperatures of ~12 to 36 °C, and the constraints from the rhinocerotid fossil to be unknown.

Finally, Jia and others (2015) reported lipid δD for C29 n-alkanes from the Dingqinghu Fm that average −188 ± 10‰, which were used to derive an estimated paleoelevation of ~3000 meters for the Early Miocene. However, these authors failed to note the published data of Polissar and others (2009) which reported lipid δD for C29 n-alkanes from both the Dingqinghu and middle Niubao Fms that average ~ −220‰ and −200‰, respectively. These more D-depleted values that are the basis for the >4 km paleoelevation estimates reported by Polissar and others (2009) should not be ignored. In a unified effort to build on our understanding of Tibetan tectonics, subsequent work must integrate all of the existing data and not simply derive new estimates based solely on a new sample suite.

Wei and others (2016) provided the elevation reconstruction most divergent from the interpretation presented in this study. Wei and others (2016) used the presence of foraminifera and $\delta^{18}O_c$ of lacustrine carbonates from the Dingqinghu Fm to derive a low elevation reconstruction of the late Eocene Gerze basin. In the present work and Polissar and others (2009), we determined that the Miocene and Eocene lacustrine carbonates were likely significantly ^{18}O-enriched relative to meteoric water due to evaporation. Therefore, the $\delta^{18}O$ values Wei and others (2016) used in their paleoelevation model may not reflect the meteoric water composition of the Eocene Gerze basin. Our calculated primary meteoric water compositions resulting from paired lipid-δD and carbonate-$\delta^{18}O$ measurements were more similar to modern Tibetan meteoric water than compositions presented in Wei and others (2016) (fig. 5). Wei and others (2016) excluded all $\delta^{18}O_c$ measurements derived from sparite under the assumption that sparite resulted from late stage meteoric diagenesis, which is often the

advisable practice. However, particularly in soils and shell voids, sparite can form during early diagenesis and cementation with effectively primary meteoric water. Under this diagenetic scenario, the early sparite would more accurately record the $\delta^{18}O_w$ of surface waters for paleoaltimetry reconstruction than the evaporatively ^{18}O-enriched lacustrine carbonates.

Further, Wei and others (2016) used the presence of a putative foraminifera (*Lagena laevis*) associated with lagoonal and estuarine environments to suggest that storm surges carried this foraminifer hundreds of kilometers inland and deposited the foraminifera in lakes that filled the Eocene Gerze basin from either the Himalayan Sea via rivers across the Gangdese volcanic arc or channels along the coastal-alluvial plain of the Pamir Sea of Western Tibet (Zhang and others, 2013). However, their correlation between fossil presence and environmental reconstruction relied on six total tests found in >300 m of section. We found this correlation untenable. Not only did the assessment rely on very low specimen counts, but the physical process of carrying the foraminifera hundreds of kilometers inland across a terrane that was already significantly above sea level in at least some regions (Wang and others, 2008; Polissar and others, 2009; Ding and others, 2014; Ingalls and others, 2017) was less probable than airborne or avian transport. The side-by-side analysis of the Wei and others (2016) isotope data and the data presented in this study demonstrated the importance of sampling and analyzing both the full temporal extent of deposition as well as lateral (coeval) sampling to characterize intrabed variability using a multi-proxy approach (Ingalls and others, 2020).

In summary, we interpreted the oxygen isotope record from the lacustrine facies of the Dingqinghu Fm, as presented in Wei and others (2016) and here, as a record of primary closed-basin hydrology out of equilibrium with the mean atmospheric water vapor and riverine input, as is true of many modern Tibetan lakes. Finally, new data should be presented within the framework of existing data and interpretations when employing proxy records for environmental and tectonic reconstructions in previously studied basins. In the next section, we proposed potential means of reconciling data sets from unique proxy-based methodologies that are otherwise unrelated in order to come to more robust reconstructions of ancient environments.

Cross-disciplinary Multi-proxy Environmental Reconstructions

The effort to reconstruct the uplift histories of Earth's orogens and plateaus has been undertaken using a broad array of proxies for ancient elevations and temperatures (Rowley and others, 2001; Ghosh and others, 2006; DeCelles and others, 2007; Polissar and others, 2009; Huntington and others, 2010; Fan and Carrapa, 2014; Ingalls and others, 2017, *et cetera*). Each proxy has biases and uncertainties unique to that technique, whether it is a syn-depositional effect (for example, evaporative ^{18}O- or D-enrichment in lake sediments), an extrapolation of extant species range to extinct relatives, or simple assumptions about the temperature-elevation relationships in different environments. Rarely are multiple, unrelated proxies employed in a single study to check an elevation estimate against another aside from measuring different isotopic systems (for example, lipid δD and carbonate $\delta^{18}O$). In this section, we propose two interdisciplinary methods by which elevation estimates from otherwise unrelated proxies can be cross-calibrated.

Species range-based reconstructions relate the maximum elevation that extant relatives of fossil specimens occupy in modern environments. This method relies on the assumption that species are sensitive to altitude rather than air and water temperature and humidity at these elevations in the modern day (Molnar and England, 1990). However, the Paleogene was characterized by globally warm intervals (such as the Paleocene-Eocene Thermal Maximum and Early Eocene Climatic Optimum) during which high-altitude environments experienced elevated temperatures

(Snell and others, 2013). We propose lipid-δD measurements of the same fossil palm leaves and tropical pollen specimens previously used to make low elevation estimates on the northern Lhasa terrane to parse the effects of altitude versus temperature on the maximum allowable ecosystem elevations. Lipid-δD measurements would enable us to assess whether the water incorporated into leaf waxes and pollen has the composition of low- or high-altitude meteoric water. Paleo-δD_{water} compositions paired with $T(\Delta_{47})$ measurements would allow us to determine whether tropical flora could persist at high altitude environments such as the Tibetan Plateau under the warmer, more humid conditions of the Paleogene. Similarly, we would suggest $\delta^{18}O$ measurements from fossil fish otoliths, for example, to directly compare physiological and isotopic estimates of paleoelevation from the same materials.

The isotopic composition of lacustrine carbonates, as employed in this study, can be used to reconstruct the composition of ancient meteoric water if the lake water composition is unaltered from local meteoric water. However, as previously discussed, closed-basin lakes are susceptible to ^{18}O- and D-enrichment during periods of lake level drawdown, and biogenic and sedimentary carbonates forming within these waters are likewise enriched in the heavy isotopes of O and H. In this work, we screen for this syn-depositional isotopic effect by observing a correlation between $\delta^{13}C$ and $\delta^{18}O$ (Leng and Marshall, 2004), and a significant range of $\delta^{18}O_c$ values that cannot feasibly all reflect equilibrium with meteoric water over such a short depositional interval (for example, within a single depositional horizon). However, we propose the use of triple oxygen isotopes to directly assess the presence and magnitude of evaporative enrichment in the carbonates used for stable isotope paleoaltimetry. The ^{17}O anomaly ($\Delta^{17}O$) of natural waters is sensitive to evaporation such that the negative excursion of ^{17}O from the ^{18}O-^{17}O meteoric water line (slope, $\lambda = 0.528$; Luz and Barkan, 2010) is directly related to the magnitude of evaporation. Passey and others (2014) found that the clearest pattern in the triple oxygen system is the ^{17}O-depletion of avian and mammalian body waters relative to meteoric water based on analyses of eggshells and tooth enamels. This technique has been successfully employed in an assortment of biogenic carbonates (Passey and others, 2014) and bioapatite (Gehler and others, 2011) from teeth, bones, and shells. Animal body waters should record the mass balance of compositions of consumed waters from food (leaf water), metabolic water (atmospheric O_2 via respiration), and drinking water (lake and groundwater), and thus should record the $\Delta^{17}O$ values of leaf and lake water as well. We suggest $\Delta^{17}O$ measurements of the fossil mammals (Tao and others, 2012), fish (Wu and others, 2017) and foraminifera (Wei and others, 2016) previously used as bases of low-altitude Tibetan Plateau reconstructions, particularly when paired with $\delta^{18}O$ of evaporatively ^{18}O-enriched lake sediments (Wei and others, 2016). $\Delta^{17}O$ measurements combined with $T(\Delta_{47})$ and $\delta^{18}O$ of the same phosphates and carbonates together with δD_{lipid} compositions would provide a direct assessment of evaporative enrichment in parallel with stable isotope elevation calculations.

CONCLUSIONS

Using carbonate clumped isotopes and stable isotope paleoaltimetry, we determined that the mean elevation of the northern Lhasa terrane has been in excess of 3.1 km above sea level since at least the Eocene. We provided direct measurements of primary carbonate formation temperatures from the late Eocene to Miocene and temperature estimates from other co-latitudinal terrestrial carbonates for the remainder of the Eocene. The middle Niubao Fm, upper Niubao Fm, and Dingqinghu Fms yielded $T(\Delta_{47})$ values of 45.3 ± 6.7 °C, 33.4 ± 4.8 °C, and 23.7 ± 3.1 °C, respectively. Solid-state reordering modeling based on best estimates of burial histories predicted little to no C—O bond reordering for the upper Niubao Fm, but partial reordering for the middle Niubao Fm. As such, the $T(\Delta_{47})$ from the middle Niubao Fm. was not used

for elevation calculations. Finally, we calculated paleo-elevations of $4372^{+1234}/_{-1895}$ m for the Eocene middle Niubao Fm, $3111^{+739}/_{-1401}$ m to $3823^{+1025}/_{-1699}$ m for the late Eocene to Oligocene upper Niubao Fm, and $4150^{+1154}/_{-1821}$ m to $4757^{+1351}/_{-2005}$ m for the Oligo-Miocene Dingqinghu Fm.

In this work, we assessed the means by which intrinsically different proxies have led to divergent interpretations due to the biases and uncertainties unique to each proxy. For the first time, we were able to place stable isotope paleoaltimetry elevation estimates within the same framework as paleontological, paleobotanical, and palynological reconstructions for the northern Lhasa terrane by reconsidering the basis by which these proxies are sensitive to temperature versus altitude. Further, we demonstrated the importance of extensive lateral and vertical sampling of available strata and consideration of the impact of syn-depositional isotopic effects (for example, evaporation) on proxy substrates and data interpretations. Importantly, investigators should realistically consider and faithfully report the accuracy and uncertainties underlying stratigraphic-age determinations of sampled intervals. In this regard, directed efforts to improve both the bio- and chronostratigraphy of depositional basins on the northern Lhasa terrane would be beneficial for our broader understanding of Tibetan tectonics. Finally, we proposed cross-disciplinary studies that would have the goal of inter-calibrating the unique approaches to environmental and tectonic reconstructions from Earth science sub-disciplines.

ACKNOWLEDGMENTS

MI thanks Chi Ma for assistance with SEM-EBSD imaging and analyses, and John Eiler and Nami Kitchen for aiding in clumped isotope analyses and data interpretations at Caltech. Funding for this work was provided by NSF EAR 9973222, EAR 0609782, EAR 0923831, and EAR 1111274 to DR, and a Barr Fellowship from the Geological and Planetary Sciences Division of Caltech to MI. The authors would like to thank Majie Fan, Alex Lechler, Michael Hren, and an anonymous reviewer for their productive reviews.

APPENDIX

Paleoaltimetry

Paleoelevation estimates are calculated using Rowley's (2007) isotopic lapse rate model relating altitude with $\delta^{18}O$ of precipitation as recorded in meteoric water in low-latitude (<35°) orographic systems, slightly modified from the original Lunpola basin stable isotope reconstruction in Rowley and Currie (2006). Rowley and Currie (2006) measured $\delta^{18}O_w$ of modern stream waters from the watershed of the Lunpola basin and determined that the paleoelevation model applied here underestimates the true elevation, and therefore we consider our calculated elevations conservative estimates rather than overestimates. Paleo-meteoric water estimates, $\delta^{18}O_w$, are calculated from carbonate $\delta^{18}O$ using mineral-specific fractionation factors, reported in Supplemental table A1. $\Delta(\delta^{18}O_w)$ was then used to estimate model elevation, Z:

$$Z(m) = -0.0129(\Delta(\delta^{18}O_p))^4 - 1.1213(\Delta(\delta^{18}O_p))^3 - 38.214(\Delta(\delta^{18}O_p))^2 - 715.22(\Delta(\delta^{18}O_p)) \quad (5)$$

where $\Delta(\delta^{18}O_p)$, a model parameter, is the difference between the oxygen isotopic composition of precipitation at elevation and that near sea level along the same mean storm trajectory. We cannot directly measure $\delta^{18}O_w$ of a coeval sea level parcel of water vapor in the past, and so we rely on lower latitude, low elevation carbonate facies to record ancient water compositions. We use a value of −6.6‰ for the low-latitude Eocene precipitation and −5.9‰ for the Oligocene to Miocene precipitation, to account for changes in global ice volume due to globally warm/cool periods. These values are lighter than modern values of $\delta^{18}O_w$ for average low latitude, low elevation

(<100 m) weather stations monitored by IAEA Global Network of Isotopes in Precipitation through 2001, ~−3.6 ± 1.6‰VSMOW, and therefore do not overestimate the isotopic differences between sea level and sample waters. The ± 2σ error envelope for the elevations uses the equations that characterize the 2σ error on the empirically determined modern precipitation-elevation relationship updated from (Rowley, 2007). The $T(\Delta_{47})$ errors are propagated through the equation for the calcite-water fractionation factor to determine $\Delta(\delta^{18}O_p)$ 2σ error. Calculated fractionation factors, reconstructed meteoric water isotopic values, $\Delta(\delta^{18}O_w)$, and elevation estimates are found in table A1.

Table A2. Summary of clumped isotope sample data. Temperatures are calculated using the Bonifacie and others (2017) calibration. The listed fractionation factors are calculated based on mineralogy and assuming $\delta^{18}O_c$ records primary mineral formation or recrystallization at the Δ_{47}-derived temperature; however, we do not use the fractionation factors marked with the double asterisk (**) in our meteoric water and elevation calculations. $\delta^{18}O$ errors are reported as ±1σ analytical uncertainty. Δ_{47} errors are reported as ±2σ combined analytical uncertainty and standard error of the mean, http://earth.geology.yale.edu/%7eajs/SupplementaryData/2020/Ingalls.

Table A3. All clumped isotope sample data for each individual measurement. Δ_{48} excess refers to significant deviation from the δ_{48}-Δ_{48} line, which would indicate an isobaric interference or contaminant on mass-48, http://earth.geology.yale.edu/%7eajs/SupplementaryData/2020/Ingalls.

Table A4. All clumped isotope data for each individual measurement of carbonate standards, http://earth.geology.yale.edu/%7eajs/SupplementaryData/2020/Ingalls.

Table A5. All clumped isotope data for each individual measurement of heated (1000 °C) and water-equilibrated (25 °C) gases, http://earth.geology.yale.edu/%7eajs/SupplementaryData/2020/Ingalls.

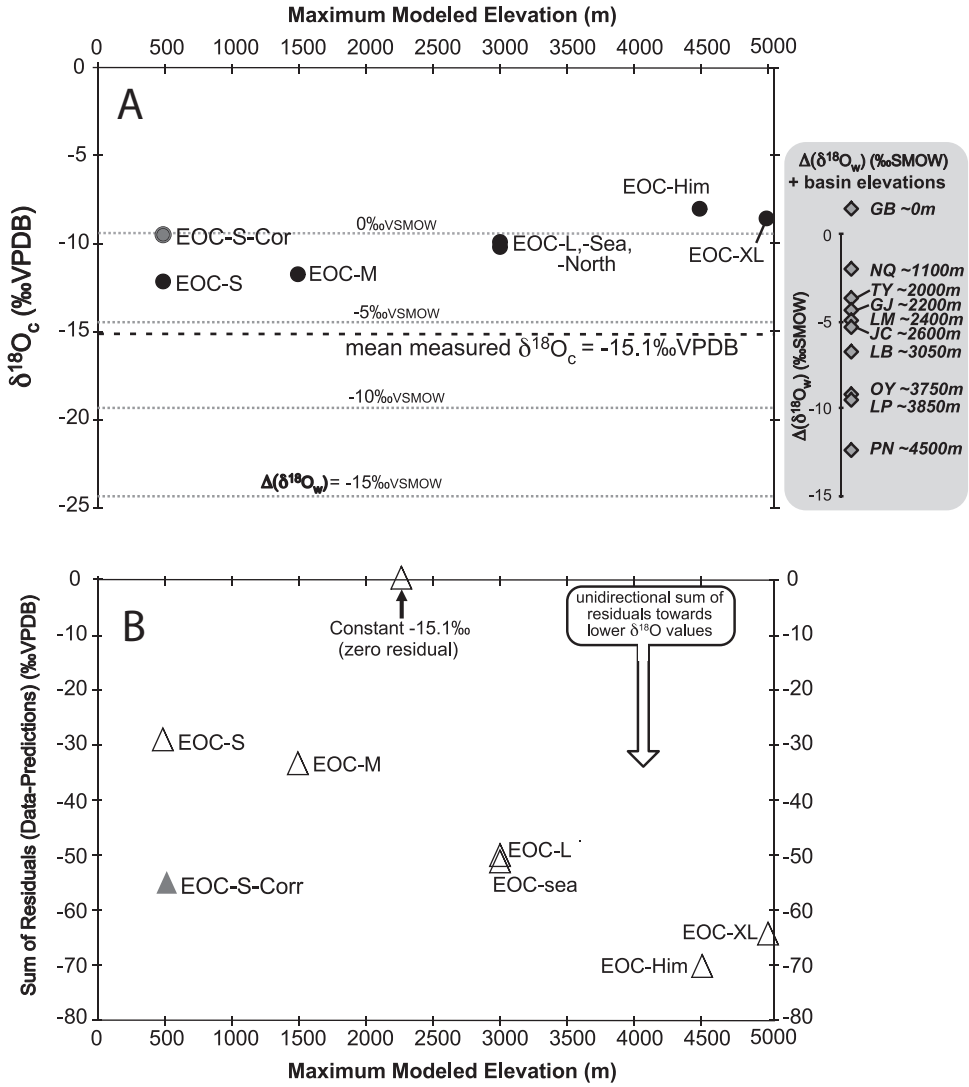

Fig. A1. Comparison of model predictions versus measured compositions for ten Eocene sequences from the Tibetan Plateau used in paleoelevation studies plotted at the maximum model elevation of Botsyun and others (2019). (A) Mean $\delta^{18}O_c$ predicted by the various Botsyun and others (2019) models (EOC-S, EOC-M, *et cetera*; black circles) at each of the 10 localities all yielded higher values than the mean $\delta^{18}O_c$ from paleoaltimetry studies (black dashed line plotted at −15.1‰VPDB) in the Gerze Basin (GB), Nangqian Basin (NQ), Tangra Yum Tso (TY), Gonjo Basin (GJ), Liming Basin (LM), Jianchuan Basin (JC), Linzhou Basin (LB), Oiyug Basin (OY), Lunpola Basin (LP), and Pana of the Penbo/Linzhou Basin (PN) of Ingalls and others (2017). $\Delta(\delta^{18}O_w)$ values with corresponding paleoelevation estimates were determined for these study basins using the conservative modern isotopic lapse rate model from Ingalls and others (2017; right of main plot and light gray dotted contours). Isotopic compositions of the most ^{18}O-depleted carbonate samples (diamonds) and an assumed temperature of 25 °C were used to calculate water isotopic compositions, and then referenced to the mean low-altitude $\delta^{18}O_c$ value of EOC-S-Corr of −9.6‰VPDB from Botsyun and others (2019). Based on the $\Delta(\delta^{18}O_w)$ lapse rate here, all Botsyun and others (2019) model results would yield elevations lower than these revised stable isotope lapse rate-based estimates from 8 of the 10 study basins. (B) The sum of residuals (measured-predicted) for each of the models were plotted as open triangles. These residuals should sum to zero for a model regressed to the data, but instead the model fits are strongly skewed to predictions that are significantly higher than the measured isotopic compositions. Note that EOC-S-Corr localities were plotted in coordinates compatible with the paleogeographic base maps rather than the uniform 13° displacement of the other models, and shown in A and B as gray filled symbols.

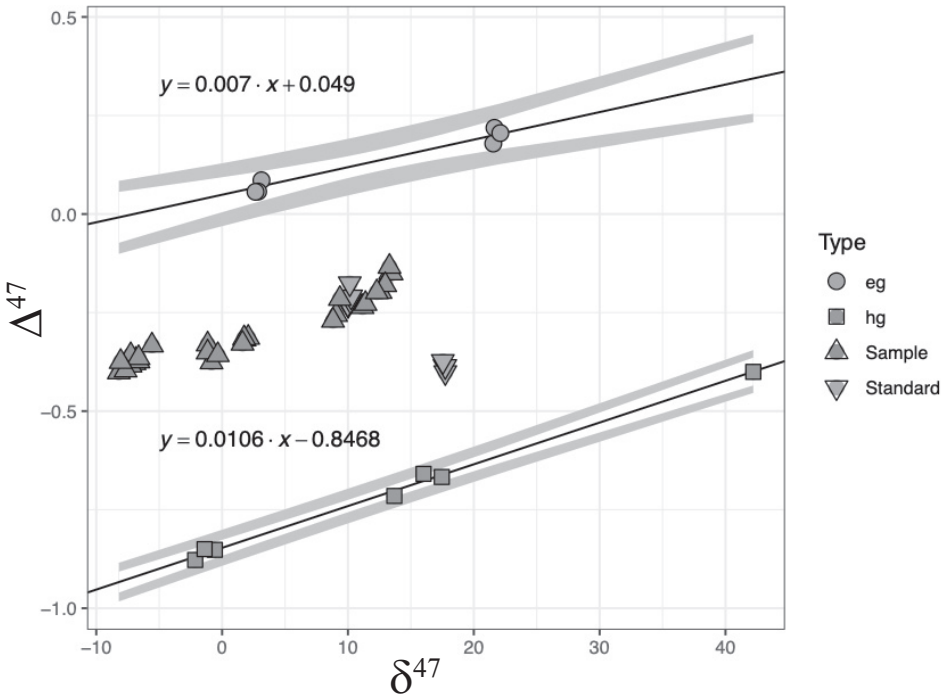

Fig. A2. Heated (1000 °C) and equilibrated (~25 °C) standard gas linear regression, with samples (upwards pointing triangles) and standards (downward pointing triangles).

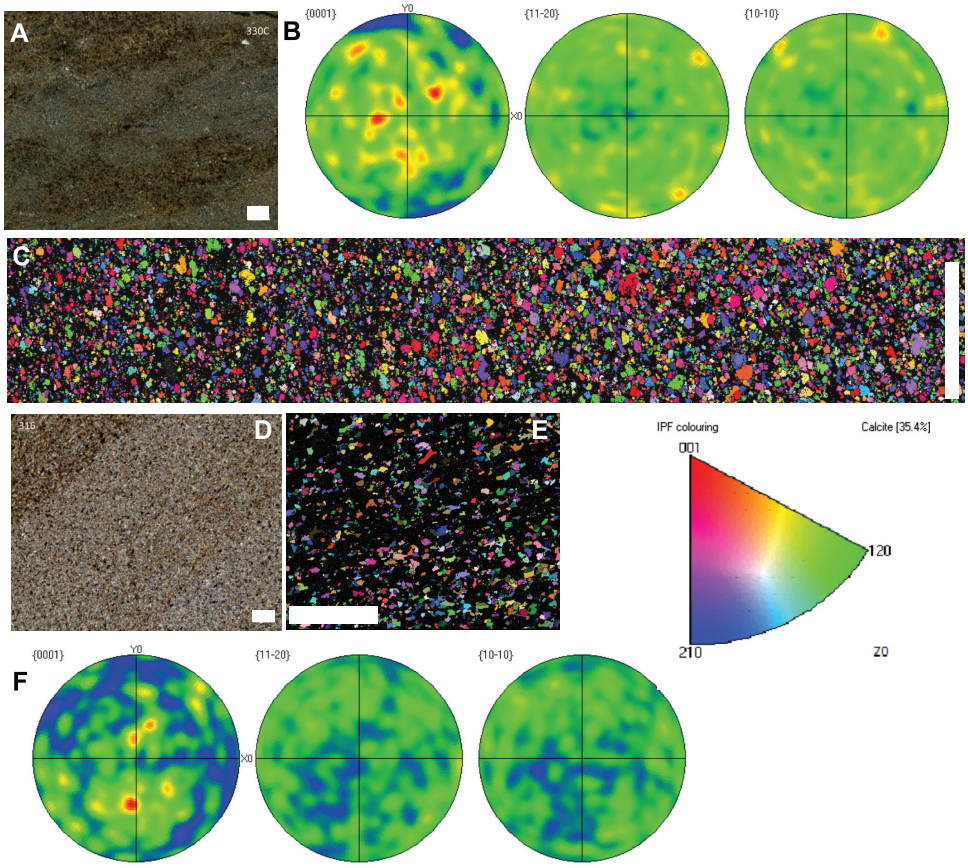

Fig. A3. Crystal preferred orientation of calcite in samples 330C (A-C) and 316 (D-F). EBSD pole figures (B, F) are plotted using an equal area upper hemisphere projection of c axes {0001} and of r {10-14} and a {11-20} planes with 6° binning. (A) Thin section viewed in cross polars of 330C. The width of all scale bars is 100 μm. (B) 330C pole figure. No clear pattern emerges. (C) Inverse pole figure (IPF) of a ~700 μm transect perpendicular to laminations. No preferred c-axis orientation is found. (D) Thin section viewed in cross polars of 316. (E) IPF of a ~300 × 300 μm section of 316. (F) EBSD pole figure of 316. No significant pattern emerges.

TABLE A1

Stable-isotope data for all carbonates and leaf waxes, and calculated paleoelevations

Dingqing Formation											
					T(Δ_{47}) (°C±1σ)	23.7	20.6	26.8			
					$\alpha_{calcite\text{-}water}$	1.02872	1.02938	1.02808			
Sample	**Lithology**	**Depositional Setting**	**Location in Section (m)**	**$\delta^{13}C_c$ (‰VPDB)**	**$\delta^{18}O_c$ (‰VPDB)**		**$\delta^{18}O_w$ (‰VSMOW)**		**Mean $\delta^{18}O_w$ (±2σ=1.3)**	**$\Delta(\delta^{18}O_w)$ (‰)**	**Model elevation (km ± 2σ)**
299B	marl	lacustrine	1580.0	-2.1	-2.1	0.0	-0.6	0.7	0.0	6.6	-6109 +2393/+619
292A	mudstone	lacustrine	1578.5	**0.3**	-5.2	-3.0	-3.7	-2.4	-3.0	3.6	-2763 +1145/+30
292C	mudstone	lacustrine	1577.0	-0.7	-4.3	-2.2	-2.8	-1.5	-2.2	4.4	-3610 +1474/+131
292D	calcareous sandstone	lacustrine	1576.5	-0.5	-7.2	-5.1	-5.7	-4.4	-5.1	1.5	-1064 +455/-50
301	marl	lacustrine	1575.0	0.5	-8.9	-6.8	-7.4	-6.2	-6.8	-0.2	128 +12/-56
301-evapcorr.	marl (leaf wax)	lacustrine	1575.0			δDw=-128±29.8‰ VSMOW			-18.7	-12.1	4478 +1270/-1928
300B	marl	lacustrine	1573.6	-4.2	-7.2	-5.1	-5.7	-4.5	-5.1	1.5	-1033 +442/-50
300A	marl	lacustrine	1572.3	-0.3	-5.1	-3.0	-3.6	-2.3	-3.0	3.6	-2843 +1177/+38
299C	mudstone	lacustrine	1570.5	2.5	-6.7	-4.6	-5.2	-3.9	-4.6	2.0	-1466 +622/-48
299C-evapcorr.	mudstone (leaf wax)	lacustrine	1570.5			δDw=-115±32.6‰ VSMOW			-17.2	-10.6	4150 +1154/-1821
299A	marl	lacustrine	1568.0	2.5	-6.7	-4.6	-5.2	-3.9	-4.6	2.0	-1466 +622/-48
299A-evapcorr.	marl (leaf wax)	lacustrine	1568.0			δDw=-135±29.4‰ VSMOW			-20.1	-13.5	4757 +1351/-2005
298C	marl	lacustrine	1556.6	1.7	-5.3	-3.2	-3.8	-2.6	-3.2	3.4	-2625 +1091/+17
298B	marl	lacustrine	1555.0	0.0	-7.1	-4.9	-5.6	-4.3	-4.9	1.7	-1159 +495/-51
298A	marl	lacustrine	1552.0	-2.5	-6.1	-3.9	-4.6	-3.3	-3.9	2.7	-1979 +832/-29
297B	marl	lacustrine	1553.0	-1.5	-4.8	-2.6	-3.3	-2.0	-2.6	4.0	-3163 +1302/+73
297	limestone	lacustrine	1551.0	-5.9	-1.3	0.9	0.2	1.5	0.8	7.4	-7186 +2768/+902
296	marl	lacustrine	1550.0	-1.0	-9.2	-7.1	-7.7	-6.5	-7.1	-0.5	324 +33/-142
							Most depleted $\delta^{18}O_w$:		-20.1‰VSMOW	-13.5‰	4757 +1351/-2005

TABLE A1
(continued)

Upper Niubao Formation

Sample	Lithology	Depositional Setting	Location in Section (m)	$\delta^{13}C_c$ (‰VPDB)	$\delta^{18}O_c$ (‰VPDB)	$T(\Delta_{47})$ (°C±1σ) / $\alpha_{calcite\text{-}water}$			$\delta^{18}O_w$ (‰VSMOW)		Mean $\delta^{18}O_w$ (±2σ=1.3)	$\Delta(\delta^{18}O_w)$ (‰)	Model elevation (km ± 2σ)
						33.1	29	37.2					
						1.02681	1.02763	1.02601					
308	pedogenic calcite	soil	1215.0	-7.5	-16.3	-12.4	-13.2	-11.6			-12.4±1.6	-5.8	2777 +615/-1252
					$T(\Delta47)$ (°C±1σ)	30.6	25.4	35.8					
					$\alpha_{calcite\text{-}water}$	1.0273	1.02837	1.02628					
Sample	**Lithology**	**Depositional Setting**	**Location in Section (m)**	**$\delta^{13}C_c$ (‰VPDB)**	**$\delta^{18}O_c$ (‰VPDB)**		**$\delta^{18}O_w$ (‰VSMOW)**				**Mean $\delta^{18}O_w$ (±2σ=1.3)**	**$\Delta(\delta^{18}O_w)$ (‰)**	**Model elevation (km ± 2σ)**
310	**pedogenic calcite**	**soil**	**1500.0**	**-7.3**	**-16.1**	**-12.6**	**-13.7**	**-11.7**			**-12.7±2.0**	**-6.1**	**2875 +650/-1296**
					$T(\Delta_{47})$ (°C±1σ)	36.6	31.3	41.9					
					$\alpha_{calcite\text{-}water}$	1.02612	1.02716	1.02512					
Sample	**Lithology**	**Depositional Setting**	**Location in Section (m)**	**$\delta^{13}C_c$ (‰VPDB)**	**$\delta^{18}O_c$ (‰VPDB)**		**$\delta^{18}O_w$ (‰VSMOW)**				**Mean $\delta^{18}O_w$ (±2σ=1.3)**	**$\Delta(\delta^{18}O_w)$ (‰)**	**Model elevation (km ± 2σ)**
309	pedogenic calcite	soil	1255.0	-7.4	-17.1	-12.5	-13.5	-11.5			-12.5	-5.9	2830 +634/-1276
305B	pedogenic calcite	soil	1100.0	-7.9	-17.7	-13.1	-14.1	-12.1			-13.1	-6.5	3029 +708/-1365
305D	pedogenic calcite	soil	1100.4	-7.8	-17.6	-13.0	-14.0	-12.1			-13.1	-6.5	3011 +701/-1357
305G	pedogenic calcite	soil	1103.0	-7.8	-17.5	-12.9	-13.9	-11.9			-12.9	-6.3	2965 +684/-1336
305I	pedogenic calcite	soil	1103.8	-7.9	-17.3	-12.7	-13.7	-11.8			-12.7	-6.1	2903 +661/-1309
305J	pedogenic calcite	soil	1105.1	-8.2	-17.8	-13.2	-14.2	-12.2			-13.2	-6.6	3054 +718/-1376
305L	pedogenic calcite	soil	1106.2	-8.0	-16.8	-12.2	-13.2	-11.2			-12.2	-5.6	2713 +592/-1223
305O	pedogenic calcite	soil	1109.8	-7.5	-17.3	-12.7	-13.7	-11.7			-12.7	-6.1	2882 +653/-1299
305P	pedogenic calcite	soil	1110.0	-7.4	-17.4	-12.8	-13.8	-11.9			-12.8	-6.2	2937 +673/-1324
305Q	**pedogenic calcite**	**soil**	1115.4	**-7.5**	**-17.5**	**-12.9**	**-13.9**	**-11.9**			**-12.9**	**-6.3**	**2966 +684/-1337**
305R	pedogenic calcite	soil	1116.3	-7.5	-17.4	-12.8	-13.8	-11.8			-12.8	-6.2	2926 +669/-1319
305S	pedogenic calcite	soil	1117.1	-7.1	-17.9	-13.3	-14.3	-12.4			-13.4	-6.8	3111 +739/-1401
305T	pedogenic calcite	soil	1117.7	-7.3	-17.5	-12.9	-13.9	-12.0			-13.0	-6.4	2978 +689/-1342
307	pedogenic calcite	soil	1200.0	-7.6	-16.6	-12.0	-13.0	-11.0			-12.0	-5.4	2635 +565/-1188
									Most depleted $\delta^{18}O_w$:		-13.4‰VSMOW	-6.8	3111 +739/-1401

TABLE A1

(continued)

Upper Niubao Formation											
					T(Δ_{47}) (°C±1σ)	33.1	29	37.2			
					$\alpha_{calcite\text{-}water}$	1.02681	1.02763	1.02601			
Sample	**Lithology**	**Depositional Setting**	**Location in Section (m)**	**$\delta^{13}C_c$ (‰VPDB)**	**$\delta^{18}O_c$ (‰VPDB)**		**$\delta^{18}O_w$ (‰VSMOW)**		**Mean $\delta^{18}O_w$ (±2σ=1.3)**	**$\Delta(\delta^{18}O_w)$ (‰)**	**Model elevation (km ± 2σ)**
316	dolomitic algal laminite	lacustrine	640.0	-4.1	-13.8	-14.0	-14.7	-13.3	-14.0	-8.1	3518 +901/-1576
326	dolomite	lacustrine	40.0	-1.6	-5.2	-5.4	-6.1	-4.7	-5.4	0.5	-317 +137/-24
327	mudstone	lacustrine	50.0	-1.6	-13.6	-10.9	-11.6	-10.2	-10.9	-5.0	2511 +522/-1131
327 evap-corr.	mudstone (leaf wax)	lacustrine	50.0			δDw=-92±30.9‰ VSMOW			-13.0	-7.1	3217 +781/-1447
330CM	marl	lacustrine	80.0	-0.9	-4.0	-1.3	-2.0	-0.6	-1.3	4.6	-3780 +1539/+156
330CM evap-corr.	marl (leaf wax)	lacustrine	80.0			δDw=-114±30.1‰ VSMOW			-17.5	-11.6	4372 +1234/-1895
330CL	limesonte	lacustrine	80.0	-1.1	-5.0	-2.3	-3.0	-1.6	-2.3	3.6	-2796 +1158/+33
318	shale	lacustrine	610.0	-0.6	-3.1	-0.4	-1.1	0.3	-0.4	5.5	-4811 +1925/+334
318B	shale	lacustrine	610.0	-1.8	-3.3	-0.6	-1.3	0.1	-0.6	5.3	-4582 +1840/+290
330b	limestone	lacustrine	80.0	-1.8	-5.2	-2.5	-3.2	-1.8	-2.5	3.4	-2629 +1093/+17
330A	limestone	lacustrine	80.0	-1.9	-4.4	-1.7	-2.4	-1.0	-1.7	4.2	-3424 +1403/+106
329	mudstone	lacustrine	70.0	-3.1	-6.1	-3.4	-4.1	-2.7	-3.4	2.5	-1819 +767/-37
328	limestone	lacustrine	60.0	-0.5	-5.2	-2.6	-3.3	-1.9	-2.6	3.3	-2568 +1068/+12
								Most depleted $\delta^{18}O_w$:	-17.5‰VSMOW	-11.6‰	4372 +1234/-1895

Clumped isotope samples for which T(Δ_{47}) values were used for $\delta^{18}O_w$ calculations are in bold text. Each clumped isotope sample's own T(Δ_{47}) was used to calculate mineral-specific fractionation factors (a) and $\delta^{18}O_w$. For samples without T(Δ_{47}) measurements, the most stratigraphically proximal clumped isotope temperature of the same facies (lacustrine or pedogenic) was used to calculate $\delta^{18}O_w$. The temperatures used for the middle Niubao Fm are sourced from previous studies (Keating-Bitonti and others, 2011; Li and others, 2019; Snell and others, 2013).

‡Middle Niubao Fm temperature based on carbonate-derived Paleocene-Eocene terrestrial and shallow marine records (Keating-Bitonti and others, 2011; Snell and others., 2013; Li and others, 2018; see text).

TABLE A2

Lunpola clumped isotopes summary

Formation	Age	Location in section (m)	Lithology	n	$\delta^{13}C_{carb}$ (‰VPBD)	$\delta^{18}O_{CO2}$ (‰VSMOW)	$\delta^{18}O_{carb}$ (‰VPBD)	Δ^{47} (‰SG-WG)	$\Delta_{47,CDES,25}$‡	$\Delta_{47,CDES,90}$	T(Δ_{47}) (°C)+	$\alpha_{calcite-water}$	calc. $\delta^{18}O_{water}$ (‰VSMOW)
Dingqing	Miocene	1580	lacustrine marl	3	-2.1	37.1	-2.2±0.1	13.4	0.696±0.024	0.605	**23.7±3.1**	1.02872	0.0±1.3
Upper Niubao	Late Eocene-Oligocene	1215	pedogenic carbonate nodule	4	-7.8	22.3	-16.4±0.1	-7.1	0.667±0.019	0.576	**33.1±4.1**	1.02681	-12.4±1.6
Upper Niubao	Late Eocene-Oligocene	1500	pedogenic carbonate nodule	3	-7.3	22.6	-16.2±0.8	-6.3	0.674±0.019	0.584	**30.6±5.2**	1.02730	-12.7±2.0
Upper Niubao	Late Eocene-Oligocene	1115.4	pedogenic carbonate nodule	3	-7.5	21.1	-17.6±0.3	-8	0.657±0.023	0.566	**36.6±5.3**	1.02612	-12.9±2.0
Middle Niubao	Eocene	640	dolomitic algal laminite	4	-4.1	24.9	-13.9±0.4	-0.9	0.623±0.020	0.533	**49.4±8.5**	1.02685**	-9.9±2.7
Middle Niubao	Eocene	50	limestone	4	-1.6	25.1	-13.7±0.2	1.8	0.632±0.026	0.542	**45.6±2.2**	1.02444**	-7.4±0.8
Middle Niubao	Eocene	70	laminated mudstone	3	-2.8	33.6	-5.6±0.1	9.1	0.633±0.029	0.542	**45.7±10.2**	1.02442**	0.0±3.6
Middle Niubao	Eocene	80	laminated algal mudstone	2	-1.1	34.1	-5.1±0.2	11.3	0.626±0.016	0.536	**47.9±1.6**	1.02402**	-5.2±0.7
Middle Niubao	Eocene	80	calcitic algal mudstone	3	-0.9	35.2	-4.1±0.3	12.6	0.654±0.020	0.564	**37.5±2.7**	1.02595**	0.0±1.0
			marble	4	2.1	37.5	-1.8±0.1	17.7	0.404±0.014				
			travertine	4	1.5	30.4	-8.7±0.1	10.1	0.650±0.008				

+ Bonifacie and others (2017) T-Δ_{47} calibration.

$\delta^{18}O$ errors are reported as 1σ analytical uncertainty. Δ_{47} errors are reported as 2σ combined analytical uncertainty and standard error of the mean.

The listed fractionation factors are calculated based on mineralogy and assuming $\delta^{18}O_c$ records primary mineral formation or recrystallization at the Δ_{47}-derived temperature; however, we do not use the fractionation factors marked with the double asterisk (**) in our meteoric water and elevation calculations.

‡$\Delta_{47,CDES,25}$ values are adjusted from 90°C acid digestion to expected values from a 25°C digestion ($\varepsilon a = 0.092‰$) and corrected to the values of two known carbonate standards.

TABLE A3

All clumped isotope sample data for each individual measurement

			with Brand parameters																		Heated gas line		Bonifacie et al. (2017) calibration	
Date	Type	SampID	# acqs	$\delta^{13}C_{carb}$ ‰ (VPBD)	s.d.	$\delta^{18}O_{CO2}$ ‰ (VSMOW)	$\delta^{18}O_{calcite}$ ‰ (VPDB)	s.d.	δ_{47}, SG-WG (‰)	s.d.	Δ_{47}, SG-WG (‰)	s.d.	s.e.	δ_{48}, SG-WG (‰)	s.d.	Δ_{48} (‰)	s.d.	Δ_{48} excess?	Δ_{47}, CDES,90	Δ_{47}, CDES,25	$\Delta_{47,CDES}$,std-corr.	slope	intercept	T(K)	T(°C)
10/19/18	sample	308	9	-7.716	0.004	22.332	-16.406	0.012	-6.957	0.039	-0.378	0.035	0.012	-7.598	0.200	-2.457	0.208	FALSE	0.569	0.661	0.660	0.01057	-0.84013	308.6	35.5
10/19/18	sample	308	9	-7.761	0.004	22.466	-16.277	0.011	-6.859	0.034	-0.369	0.028	0.009	-7.077	0.302	-2.196	0.297	FALSE	0.577	0.669	0.667	0.01057	-0.84013	306.0	32.8
10/21/18	sample	308	9	-7.959	0.005	22.252	-16.483	0.016	-7.277	0.032	-0.384	0.028	0.009	-7.792	0.245	-2.496	0.245	FALSE	0.566	0.658	0.657	0.01057	-0.84013	309.7	36.6
10/21/18	sample	308	9	-7.898	0.003	22.181	-16.551	0.007	-7.261	0.020	-0.358	0.023	0.008	-8.027	0.182	-2.594	0.182	FALSE	0.593	0.685	0.684	0.01057	-0.84013	300.6	27.4
			Avg	**-7.833**		**22.308**	**-16.429**		**-7.089**		**-0.372**			**-7.623**		**-2.435**			**0.576**	**0.668**	**0.667**				**33.1**
			± 1σ	**±0.114**		**±0.122**	**±0.118**		**±0.212**		**±0.011**			**±0.404**		**±0.170**			**±0.012**	**±0.012**	**±0.012**				**±4.1**
10/16/18	sample	310	9	-7.513	0.003	23.488	-15.294	0.006	-5.573	0.025	-0.333	0.025	0.008	-4.197	0.258	-1.297	0.267	FALSE	0.602	0.694	0.692	0.01057	-0.84013	297.9	24.8
10/20/18	sample	310	9	-7.206	0.003	22.138	-16.592	0.017	-6.651	0.026	-0.373	0.019	0.006	-8.202	0.261	-2.690	0.244	FALSE	0.571	0.663	0.661	0.01057	-0.84013	308.1	35.0
10/20/18	sample	310	9	-7.182	0.003	22.117	-16.612	0.007	-6.641	0.040	-0.365	0.036	0.012	-8.260	0.146	-2.707	0.144	FALSE	0.579	0.671	0.670	0.01057	-0.84013	305.2	32.0
			Avg	**-7.301**		**22.581**	**-16.166**		**-6.288**		**-0.357**			**-6.886**		**-2.231**			**0.584**	**0.676**	**0.674**				**30.6**
			± 1σ	**±0.369**		**±1.571**	**±0.756**		**±1.239**		**±0.043**			**±4.659**		**±1.618**			**±0.032**	**±0.032**	**±0.032**				**±5.2**
10/16/18	sample	316	9	-4.009	0.004	24.526	-14.294	0.007	-1.148	0.030	-0.330	0.028	0.009	-1.248	0.282	-0.382	0.290	FALSE	0.559	0.651	0.650	0.01057	-0.84013	312.1	39.0
10/19/18	sample	316	9	-4.143	0.005	25.010	-13.829	0.007	-0.843	0.019	-0.376	0.027	0.009	-0.013	0.297	-0.088	0.288	FALSE	0.509	0.601	0.600	0.01057	-0.84013	332.0	58.8
10/21/18	sample	316	9	-4.126	0.003	24.658	-14.168	0.007	-1.151	0.038	-0.351	0.039	0.013	-1.094	0.171	-0.484	0.163	FALSE	0.538	0.630	0.629	0.01057	-0.84013	320.0	46.8
10/22/18	sample	316	9	-4.205	0.004	25.560	-13.300	0.008	-0.340	0.022	-0.358	0.024	0.008	1.482	0.201	0.334	0.204	FALSE	0.523	0.615	0.614	0.01057	-0.84013	326.1	52.9
			Avg	**-4.121**		**24.939**	**-13.898**		**-0.871**		**-0.354**			**-0.218**		**-0.155**			**0.533**	**0.625**	**0.623**				**49.4**
			± 1σ	**±0.082**		**±0.462**	**±0.444**		**±0.382**		**±0.019**			**±1.259**		**±0.367**			**±0.022**	**±0.022**	**±0.022**				**±8.5**
10/17/18	sample	327	9	-1.570	0.002	25.093	-13.749	0.008	1.792	0.049	-0.318	0.043	0.014	0.140	0.144	-0.108	0.139	FALSE	0.543	0.635	0.633	0.01057	-0.84013	318.3	45.2
10/18/18	sample	327	9	-1.596	0.003	25.400	-13.454	0.010	2.076	0.051	-0.314	0.044	0.015	1.250	0.166	0.403	0.179	FALSE	0.544	0.636	0.635	0.01057	-0.84013	317.7	44.6
10/21/18	sample	327	9	-1.571	0.003	25.045	-13.796	0.016	1.746	0.020	-0.315	0.020	0.007	0.074	0.165	-0.080	0.168	FALSE	0.546	0.638	0.637	0.01057	-0.84013	317.0	43.9
10/22/18	sample	327	9	-1.619	0.004	24.982	-13.856	0.007	1.623	0.040	-0.329	0.042	0.014	-0.049	0.187	-0.082	0.191	FALSE	0.533	0.625	0.624	0.01057	-0.84013	322.0	48.8
			Avg	**-1.589**		**25.130**	**-13.714**		**1.809**		**-0.319**			**0.354**		**0.033**			**0.542**	**0.634**	**0.632**				**45.6**
			± 1σ	**±0.024**		**±0.186**	**±0.179**		**±0.192**		**±0.007**			**±0.603**		**±0.247**			**±0.006**	**±0.006**	**±0.006**				**±2.2**
10/19/18	sample	299B	9	-2.122	0.004	37.083	-2.213	0.006	13.351	0.040	-0.148	0.039	0.013	34.294	0.158	10.291	0.155	FALSE	0.601	0.693	0.692	0.01057	-0.84013	298.1	24.9
10/19/18	sample	299B	9	-2.109	0.006	37.194	-2.107	0.011	13.471	0.039	-0.150	0.040	0.013	34.612	0.160	10.386	0.162	FALSE	0.598	0.690	0.688	0.01057	-0.84013	299.1	26.0
10/22/18	sample	299B	9	-2.109	0.004	37.004	-2.290	0.009	13.300	0.018	-0.133	0.026	0.009	34.040	0.310	10.198	0.311	FALSE	0.617	0.709	0.707	0.01057	-0.84013	293.2	20.1
			Avg	**-2.113**		**37.094**	**-2.203**		**13.374**		**-0.144**			**34.316±**		**10.292**			**0.605**	**0.697±**	**0.696**				**23.7**
			± 1σ	**±0.015**		**±0.192**	**±0.092**		**±0.176**		**±0.018**			**0.573**		**±0.188**			**±0.020**	**0.020**	**±0.020**				**±3.1**
10/17/18	sample	305Q	8	-7.522	0.004	20.902	-17.782	0.015	-8.207	0.032	-0.401	0.029	0.010	-11.536	0.338	-3.633	0.334	FALSE	0.558	0.650	0.648	0.01057	-0.84013	312.7	39.6
10/18/18	sample	305Q	9	-7.496	0.007	21.413	-17.290	0.005	-7.671	0.039	-0.397	0.043	0.014	-9.919	0.156	-3.002	0.160	FALSE	0.557	0.649	0.648	0.01057	-0.84013	312.9	39.8
10/20/18	sample	305Q	9	-7.502	0.004	21.003	-17.684	0.008	-8.061	0.031	-0.375	0.025	0.008	-11.322	0.239	-3.615	0.240	FALSE	0.584	0.676	0.674	0.01057	-0.84013	303.7	30.6
			Avg	**-7.507**		**21.106**	**-17.585**		**-7.980**		**-0.391**			**-10.926**		**-3.417**			**0.566**	**0.658**	**0.657**				**36.6±**
			± 1σ	**±0.027**		**±0.541**	**±0.260**		**±0.553**		**±0.028**			**±1.756**		**±0.719**			**±0.030**	**±0.030**	**±0.030**				**5.3**

TABLE A3
(continued)

			with Brand parameters																	Heated gas line		Bonifacie et al. (2017) calibration	
Date	Type	SampID	# acqs	$\delta^{13}C_{carb}$ ‰ (VPBD)	s.d.	$\delta^{18}O_{CO2}$ ‰ (VSMOW)	$\delta^{18}O_{calcite}$ ‰ (VPDB)	s.d.	$\delta_{47,SG-WG}$ (‰)	s.d.	$\Delta_{47,SG-WG}$ (‰)	s.d.	s.e.	$\delta_{48,SG-WG}$ (‰)	s.d.	Δ_{48} (‰)	s.d.	Δ_{48} excess?	$\Delta_{47,CDES,90}$	$\Delta_{47,CDES,25}$	$\Delta_{47,CDES,std-corr.}$	slope	intercept	T(K)	T(°C)
10/18/18	sample	329L	9	-2.915	0.004	33.657	-5.509	0.009	9.060	0.024	-0.256	0.029	0.010	24.436	0.380	7.302	0.378	FALSE	0.533	0.625	0.624	0.01057	-0.84013	322.0	48.8
10/20/18	sample	329L	9	-2.682	0.004	33.691	-5.478	0.008	9.362	0.043	-0.215	0.040	0.013	24.590	0.142	7.388	0.146	FALSE	0.572	0.664	0.663	0.01057	-0.84013	307.5	34.4
10/17/18	sample	329L	8	-2.929	0.003	33.439	-5.720	0.006	8.814	0.058	-0.270	0.055	0.019	23.962	0.300	7.262	0.303	FALSE	0.521	0.613	0.611	0.01057	-0.84013	327.1	54.0
			Avg	**-2.842**		**33.596**	**-5.569**		**9.079**		**-0.247**			**24.329**		**7.318**			**0.542**	**0.634**	**0.633**				**45.7**
			± 1σ	**±0.278**		**±0.274**	**±0.132**		**±0.549**		**±0.057**			**±0.655**		**±0.130**			**±0.054**	**±0.054**	**±0.054**				**±10.2**
10/17/18	sample	330CL	9	-1.1190568	0.005	33.983	-5.197	0.024	11.159	0.031	-0.236	0.021	0.007	25.222	0.286	7.434	0.281	FALSE	0.533	0.625	0.623	0.01057	-0.84013	322.2	49.0
10/18/18	sample	330CL	9	-1.1256341	0.004	34.215	-4.973	0.018	11.392	0.033	-0.228	0.027	0.009	25.952	0.301	7.699	0.297	FALSE	0.539	0.631	0.629	0.01057	-0.84013	319.8	46.7
			Avg	**-1.122**		**34.099**	**-5.085**		**11.276**		**-0.232**			**25.587±**		**7.566**			**0.536**	**0.628**	**0.626**				**47.9**
			± 1σ	**±0.005**		**±0.164**	**±0.158**		**±0.165**		**±0.006**			**0.516**		**±0.187**			**±0.004**	**±0.004**	**±0.004**				**±1.6**
10/18/18	sample	330CM	9	-0.868	0.004	35.134	-4.089	0.008	12.590	0.024	-0.197	0.028	0.009	28.552	0.294	8.460	0.281	FALSE	0.558	0.650	0.649	0.01057	-0.84013	312.6	39.4
10/18/18	sample	330CM	9	-0.867	0.003	35.489	-3.747	0.011	12.962	0.036	-0.180	0.029	0.010	29.499	0.173	8.697	0.162	FALSE	0.572	0.664	0.663	0.01057	-0.84013	307.6	34.4
10/21/18	sample	330CM	9	-0.923	0.007	34.888	-4.325	0.017	12.291	0.032	-0.198	0.032	0.011	28.025	0.161	8.422	0.159	FALSE	0.560	0.652	0.651	0.01057	-0.84013	311.8	38.7
			Avg	**-0.886**		**35.171**	**-4.054**		**12.614**		**-0.192**			**28.692**		**8.526**			**0.564**	**0.656**	**0.654**				**37.5**
			± 1σ	**±0.063**		**±0.604**	**±0.291**		**±0.672**		**±0.021**			**±1.494**		**±0.298**			**±0.015**	**±0.015**	**±0.015**				**±2.7**

Δ_{48} excess refers to significant deviation from the δ_{48}-Δ_{48}line, which would indicate an isobaric interference or contaminant on mass-48.

TABLE A4

All clumped isotope data for each individual measurement of carbonate standards

				with Brand parameters													Heated gas line	
date	**Type**	**Sample ID**	**# acqs**	**$\delta^{13}C_{carb}$ (‰VPBD)**	**$\delta^{18}O_{CO2}$ (‰VSMOW)**	**$\delta^{18}O_{calcite}$ (‰VPDB)**	**δ_{47} (‰SG-WG)**	**Δ_{47} (‰SG-WG)**	**Δ_{47} std. dev.**	**Δ_{47} s.e.**	**δ_{48} (‰SG-WG)**	**Δ_{48}**	**Δ48 excess?**	**$\Delta_{47,CDES,90}$**	**$\Delta_{47,CDES,25}$**	**$\Delta_{47,CDES,std\text{-}corr.}$**	**slope**	**intercept**
10/15/18	standard	CIT Carrara	9	2.147±0.003	37.461	-1.850±0.007	17.673±0.046	-0.386	0.040	0.013	35.555±0.289	10.769±0.287	FALSE	0.310	0.402	0.401	0.01057	-0.84013
10/16/18	standard	CIT Carrara	9	2.155±0.004	37.530	-1.784±0.012	17.734±0.038	-0.402	0.029	0.010	35.612±0.291	10.690±0.293	FALSE	0.293	0.385	0.384	0.01057	-0.84013
10/17/18	standard	CIT Carrara	9	2.123±0.003	37.542	-1.772±0.006	17.730±0.045	-0.386	0.041	0.014	35.109±0.141	10.176±0.139	FALSE	0.317	0.409	0.416	0.01112	-0.84316
10/21/18	standard	CIT Carrara	9	2.103±0.004	37.355	-1.952±0.006	17.538±0.042	-0.373	0.037	0.012	34.829±0.141	10.266±0.133	FALSE	0.326	0.418	0.420	0.01059	-0.84081
			Avg ± 1σ	**2.132±0.024**	**37.472±0.086**	**-1.840±0.082**	**17.669±0.092**	**-0.387±0.012**			**35.276±0.373**	**10.476±0.298**		**0.312±0.014**	**0.404±0.014**	**0.405±0.016**		
10/15/18	standard	TV04	8	1.479±0.003	30.287	-8.753±0.011	10.018±0.029	-0.230	0.024	0.009	14.953±0.222	4.494±0.210	FALSE	0.550	0.642	0.640	0.01057	-0.84013
10/16/18	standard	TV04	9	1.499±0.003	30.235	-8.802±0.006	9.988±0.025	-0.227	0.022	0.007	14.855±0.275	4.497±0.277	FALSE	0.554	0.646	0.644	0.01057	-0.84013
10/17/18	standard	TV04	9	1.462±0.004	30.465	-8.581±0.007	10.191±0.033	-0.219	0.036	0.012	15.293±0.199	4.483±0.190	FALSE	0.560	0.652	0.651	0.01057	-0.84013
10/19/18	standard	TV04	9	1.475±0.005	30.501	-8.546±0.007	10.249±0.035	-0.210	0.035	0.012	15.594±0.157	4.710±0.158	FALSE	0.569	0.661	0.659	0.01057	-0.84013
			Avg ± 1σ	**1.479±0.015**	**30.372±0.131**	**-8.671±0.126**	**10.111±0.128**	**-0.221±0.009**			**15.174±0.337**	**4.546±0.109**		**0.558±0.008**	**0.650±0.008**	**0.649±0.008**		

TABLE A5

All clumped isotope data for each individual measurement of heated (1000°C) and water-equilibrated (25°C) gases

date	Type	Sample ID	# acqs	$\delta^{13}C_{carb}$ (‰VPBD)	$\delta^{13}C_{carb}$ s.d.	$\delta^{18}O_{CO2}$ (‰VSMOW)	$\delta^{18}O$ s.d.	δ_{47} (‰SG-WG)	δ_{47} s.d.	Δ_{47} (‰SG-WG)	Δ_{47} s.d.	Δ_{47} s.e.	δ_{48} (‰SG-WG)	δ_{48} s.d.	Δ_{48}	Δ_{48} s.d.
10/15/18	hg	BOC(HG)	9	-11.105	0.003	31.018	0.006	-2.140	0.030	-0.878	0.024	0.008	17.013	0.299	5.119	0.294
10/15/18	hg	eBOC(HG)	9	-11.046	0.003	50.601	0.006	17.456	0.030	-0.667	0.024	0.008	73.557	0.286		0.266
10/16/18	hg	BOC(HG)	9	-11.000	0.003	32.470	0.013	-0.579	0.012	-0.852	0.025	0.008	20.715	0.182	5.943	0.162
10/17/18	hg	eBOC(HG)	9	-10.876	0.004	46.710	0.006	13.684	0.061	-0.715	0.055	0.018	61.670	0.333	18.100	0.319
10/18/18	hg	eBOC(HG)	8	-11.002	0.003	49.137	0.009	16.009	0.039	-0.659	0.033	0.012	68.340	0.261	19.767	0.245
10/21/18	hg	BOC(HG)	9	-10.981	0.008	31.658	0.016	-1.392	0.047	-0.850	0.040	0.013	18.571	0.229	5.451	0.211
10/20/18	hg	eBOC_ Berkeley(HG)	9	-10.681	0.004	75.094	0.008	42.208	0.025	-0.400	0.030	0.010	143.956	0.212	39.902	0.193
10/14/18	eg	eBOC(25)	8	-10.985	0.002	53.809	0.007	21.549	0.032	0.179	0.031	0.011	83.318	0.268	24.842	0.242
10/15/18	eg	eBOC(25)	9	-10.889	0.003	53.768	0.005	21.644	0.033	0.219	0.032	0.011	83.203	0.333	24.813	0.306
10/15/18	eg	BOC(25)	9	-8.498	0.003	32.806	0.008	3.128	0.019	0.086	0.020	0.007	22.699	0.275	7.242	0.269
10/16/18	eg	BOC(25)	9	-8.463	0.002	32.534	0.005	2.863	0.028	0.057	0.033	0.011	21.600	0.249	6.689	0.244
10/19/18	eg	eBOC(25)	9	-10.573	0.005	53.991	0.019	22.107	0.048	0.205	0.045	0.015	82.612	0.183	23.901	0.155
10/20/18	eg	BOC(25)	9	-8.504	0.003	32.385	0.004	2.651	0.029	0.056	0.030	0.010	20.884	0.193	6.306	0.185

TABLE A6

Modern Tibetan lake surface water temperature metadata compilation from Moderate Resolution Imaging Spectroradiometer data

Lake or identifier	Latitude (°N)	Longitude (°E)	Elevation (m)	Mean monthly max. T (°C)*	Elevation (m)	Mean monthly max. T by elevation bin (°C)
2005NB001innerF	33.5	89.58	4957	14.1	2250	23.6
2005NB001Yellow	36.15	101.77	2227	23.6	2750	21.6
2005NB002innerF	33.94	84.87	4869	18.0	3250	20.4
Aiyong Co	33.37	80.55	4292	27.3	3750	15.3
Ake Sayi Lake	35.21	79.84	4844	13.9	4250	19.3
Alake Lake	35.57	97.12	4101	15.9	4750	16.4
Amjog Co	29.63	86.25	4869	21.6	5250	14.3
Amu Co	33.45	88.7	4969	14.2		
Angdar Co	32.71	89.58	4841	14.0		
Angrenjin Co	29.31	87.19	4300	23.2		
Angshang Co	33.72	82.67	5061	16.8		
A'ong Co	32.77	81.72	4425	18.9		
Aqqikkol Lake	37.08	88.42	4251	12.3		
Argog Co	30.98	82.24	5116	14.6		
Aru Co	33.99	82.39	4950	14.0		
Ashikule Lake	35.74	81.56	4675	21.3		
Ayakkum Lake	37.55	89.42	3876	13.7		
Ayonggama Co	34.78	98.29	4213	21.4		
Ayongwu'erma Co	34.79	98.2	4212	19.7		
Baibing Lake	35.9	86.43	4896	15.4		
Baidoi Co	32.8	87.83	4776	15.8		
Bairab Co	35.03	83.13	4960	11.9		
Baitan Lake	34.56	88.58	4816	20.3		
Baitutang Lake	34.65	87.61	5079	17.4		
Bajiu Co	28.79	90.85	4513	21.0		
Bamco	31.26	90.58	4560	14.0		
Bandao Lake	34.17	88.44	4913	13.5		
Bangdag Co	34.95	81.56	4904	12.5		
Bangkog Co	31.74	89.51	4527	16.0		
Bangong Co	33.69	79.21	4749	16.8		
Baqian Co	31.93	82.78	4975	20.6		
Beilei Co	32.9	88.44	4816	17.7		
Beilikeke Lake	36.71	89.04	4701	16.8		
Beiyu Lake	33.03	86.17	4846	18.3		
Bengze Co	32.08	88.67	4531	21.6		
Bensong Co	33.21	86.43	4913	17.4		
Bero Zeco	32.43	82.93	4402	19.8		
Biluo Co	32.89	88.84	4812	15.2		
Bong Co	31.22	91.16	4666	12.4		
Botao Lake	34.01	89.95	4988	11.9		
Bumu Co	33.26	81.65	4534	22.8		
Burog Co	34.4	85.77	5166	10.1		
Caiji Co	31.21	85.44	4660	18.0		
Caka Salt Lake	36.7	99.11	3061	23.9		
Cam Co	32.12	83.55	4340	17.2		
Cedo Caka	33.17	89	4846	16.8		
Cemar Co	33.55	84.59	4582	16.2		
Chabo Co	33.36	84.19	4513	16.9		
Chabyer Co	31.42	84.06	4424	19.7		
Chacang Co	30.23	88.58	4836	20.4		
Chamu Co	33.26	83.01	4796	23.9		
Changhong Lake	36.05	86.02	4971	17.9		
Changhu Lake1	35.02	84.48	4937	19.6		
Changhu Lake2	34.71	89.04	4839	13.5		
Chaqmaqtin Lake	37.23	74.18	4031	23.6		
Chem Co	34.16	79.78	4961	14.5		
Chen Co	28.95	90.52	4431	19.0		
Chibzhang Co	33.45	90.27	5247	11.1		
Chumba Yumco	28.23	89.64	4596	18.7		
Co Ngoin1	31.59	88.72	4563	15.1		
Co Ngoin2	31.47	91.51	4523	15.7		
Co Nyi	34.57	87.25	4922	13.4		
Como Chamling	28.4	88.23	4424	18.6		
Cuochuolong	29.12	85.4	4632	27.6		
Cuoda Rima	35.33	91.86	4783	11.1		
Cuojia Lake	31.99	91.37	4586	17.3		
Cuojiangqin	33.99	92.82	4494	25.7		
Cuolaba'e'eadong	35.43	95.42	4487	17.9		
Cuona Co	31.63	82.33	4815	18.8		
Cuona Lake	32.03	91.48	4585	13.8		
Cuowomo	29.8	86.94	4983	18.8		
Dachaidan Lake	37.84	95.24	3151	21.7		
Daggyai Co	29.84	85.72	5145	13.6		

TABLE A6
(continued)

Lake or identifier	Latitude (°N)	Longitude (°E)	Elevation (m)	Mean monthly max. T (°C)*	Elevation (m)	Mean monthly max. T by elevation bin (°C)
Dachaidan Lake	37.84	95.24	3151	21.7		
Daggyai Co	29.84	85.72	5145	13.6		
Dangqiong Co	31.57	86.74	4464	17.1		
Darab Co	32.47	83.21	4434	22.7		
Daru Co	31.7	90.74	4683	15.3		
Dawa Co	31.24	84.96	4623	15.5		
Daxiong Lake	34.05	85.61	4880	14.7		
Dazadizha Co	32.87	87.12	4731	20.6		
De'arang Co	31.38	83.66	4506	26.8		
Deyu Lake	35.69	87.26	4855	13.5		
Dingjiamang Co	29.65	85.74	5065	23.6		
Dogai Coring	34.58	88.96	4818	12.5		
Dogaicoring Qangco	35.32	89.24	4787	11.4		
Dong Co	32.18	84.73	4394	17.1		
Donggei Cuona Lake	35.3	98.55	4081	13.6		
Dongka Co	31.78	90.4	4620	15.3		
Dongmo Co	32.3	86.57	4488	22.2		
Dongyue Lake	34.38	89.21	4840	16.7		
Dulishi Lake	34.74	81.89	5039	11.8		
Dung Co	31.71	91.16	4551	14.9		
Duoma Co	32.96	84.46	4675	21.9		
Duoqing Co	28.14	89.36	4472	19.3		
Ezong Co	32.86	89.46	4918	16.3		
Finger Lake	33.72	85.12	4916	21.5		
Ga'a Co	32.21	88.96	4619	20.8		
Gahai1	37.13	97.55	2849	23.1		
Gahai2	37.01	100.57	3197	18.9		
Galala Co	34.49	97.73	4417	14.4		
Gangnagema Co	34.32	98.66	4174	17.0		
Gangtang Co	33.2	86.67	4876	16.9		
Ganongcuo Lake	31.91	91.54	4585	18.0		
Gansenquan Lake	37.46	92.77	2740	44.8		
Gaotai Lake	35.41	90.96	5016	12.5		
Garen Co	30.77	84.95	4693	18.8		
Garkung Caka	33.97	86.49	4909	14.4		
Gasi Kule Lake	38.12	90.78	2854	19.5		
Gemang Co	31.58	87.28	4605	15.4		
Gemu Caka	33.66	85.81	4675	15.5		
Gomang Co	31.22	89.2	4629	15.7		
Gopug Co	31.86	83.18	4718	17.4		
Goren Co	31.12	88.34	4649	13.1		
Gouren Lake	34.6	92.46	4673	15.2		
Gozha Co	35.02	81.07	5080	8.9		
Guogen Co	32.4	89.19	4668	16.2		
Guojialun Lake	31.99	88.69	4522	15.8		
Gyarab Punco	32.2	87.78	4647	15.2		
Gyaring Lake	34.93	97.26	4290	13.0		
Gyesar Co	30.21	84.8	5198	12.5		
Haidingnuo'er	35.58	93.17	4468	16.0		
Haobo Lake	34.4	88	4839	17.2		
Har Lake	38.29	97.59	4076	11.1		
Hehua Lake	36.14	88.99	4843	15.2		
Heihai	35.99	93.26	4438	13.5		
Heishi North Lake	35.56	82.75	5049	10.3		
Hengliang Lake	34.88	89.06	4872	18.1		
Hoh Xil Lake	35.59	91.14	4886	9.8		
Hongshan Lake	35.46	78.94	4831	21.9		
Hot Spring Lake	34.43	83.56	4918	20.4		
Huangshui Lake	34.33	87.69	4890	15.0		
Hulu Lake	34.42	91.03	4887	15.4		
Huluchi Lake	35.04	87.01	4822	16.0		
Huolunuo'er	35.55	91.92	4753	10.3		
Jiamucheng Co	33.74	90.64	5007	13.4		
Jiang Co	31.55	90.82	4611	14.5		
Jiangchai Co	32.16	90.46	4660	20.1		
Jiaomu Caka	33.28	87.21	4765	20.3		
Jiaqing Co	32.45	85.77	4612	21.4		
Jiaruo Co	32.19	86.6	4499	26.3		
Jieyue Lake	35.07	90.27	4827	15.8		
Jieze Caka	33.95	80.9	4525	15.9		
Jingyu Lake	36.33	89.44	4713	10.7		
Jiuru Co	31.01	89.92	4687	15.4		
Junma Co	31.17	81.64	5431	17.4		
Kaba Niu'erduo	35.42	95.11	4585	15.9		

TABLE A6

(continued)

Lake or identifier	Latitude (°N)	Longitude (°E)	Elevation (m)	Mean monthly max. T (°C)*	Elevation (m)	Mean monthly max. T by elevation bin (°C)
Kahu Co	33.39	82.98	4772	17.4		
Kanbakadong Co	35.21	95.13	4539	17.9		
Kangru Caka	33.56	86.96	4768	20.9		
Karacul Lake	39.06	73.42	3942	13.2		
Katiao Co	33.95	82.96	4950	13.8		
Kekao Lake	35.7	91.37	4886	10.5		
Keluke Lake	37.28	96.89	2814	22.4		
Kong Co	30.82	88.35	4908	21.5		
Kongkong Caka	33.16	88.11	4777	15.1		
Kongmu Co	29.01	90.45	4445	16.3		
Koucha	34.01	97.23	4531	15.2		
Kuhai	35.3	99.18	4127	15.2		
Kunggyu Co	30.64	82.13	4784	15.6		
Kunzhong Co	33.1	80.39	4344	26.7		
Kusai Lake	35.74	92.86	4475	11.9		
Kushuihuan	35.99	90.12	5002	10.1		
Kyebxang Co	32.45	89.98	4615	14.4		
Labu Co	32.96	83.8	4552	19.6		
Lagkor Co	32.03	84.13	4467	16.9		
Langa Co	30.69	81.23	4570	13.3		
Langqiang Co	28.72	85.88	4646	24.2		
Laorite Co	33.73	90.01	4954	12.6		
Laxiang Co	33.98	86.04	4971	17.0		
Laxiong Co	34.34	85.23	4885	13.5		
Lexiewudan Co	35.75	90.2	4870	9.7		
Lingguo Co	33.85	88.59	5062	11.1		
Liudan Lake	34.68	79.69	5187	12.9		
Longre Co	34.86	98.02	4213	23.4		
Longwei Co	33.87	88.31	4942	13.3		
Longzhou Lake	35.06	86.93	4805	16.4		
Luma Chagco	33.01	85.37	4745	21.0		
Lumajiangdong Co	34.02	81.62	4812	13.5		
Lungmu Co	34.61	80.46	5004	12.7		
Luotuo Lake	34.44	81.94	5113	12.3		
Luxung Co	32.7	88.54	4839	20.4		
Ma'an Lake	35.23	89.5	4810	15.5		
Ma'erxia Co	30.97	87.47	4705	16.5		
Maindung Co	33.53	78.91	4365	20.3		
Mang Co	34.5	80.44	5133	18.9		
Mapam Yumco	30.68	81.47	4585	13.4		
Maqiao Co	33.62	90.21	4943	13.7		
Margai Caka	35.12	86.75	4793	13.2		
Margog Caka	33.86	87.01	4836	14.9		
Mazhangcuoqin	34.34	91.59	4675	15.8		
Meiju Lake	36.02	88.41	4872	19.1		
Meiriqiecuomari	33.64	89.72	4947	12.8		
Memar Co	34.22	82.31	4920	13.1		
Merqung Co	31.02	84.58	4670	20.0		
Mingjing Lake	35.07	90.54	4803	12.4		
Mudidalayu Co	30.58	88.59	4802	16.9		
Mugqu Co	31.05	89	4686	16.3		
Naiqam Co	32.32	88.69	4607	16.9		
Naka Co	31.86	89.79	4537	19.9		
Nam Co	30.74	90.6	4724	11.4		
Nanzha Co	32.67	85.47	4899	23.1		
Nariyong Co	28.3	91.95	4749	15.4		
Nawu Lake	32.92	82.08	4379	27.0		
Neri Punco	31.3	91.47	4524	15.9		
Ngangla Ringco	31.54	83.08	4716	14.9		
Ngangze Co	31.02	87.14	4685	15.3		
Ngoinyar Coqung	32.98	88.7	4822	14.7		
Ngoring Lake	34.9	97.7	4267	12.9		
Ningri Co	33.32	85.58	5044	15.9		
Niri Acuogai	33.09	93.21	4706	14.8		
Noname_1	34.28	85.07	4862	17.3		
Noname_2	32.82	82.21	4376	20.0		
Noname_3	35.23	83.98	4852	20.6		
Noname_5	35.78	83.46	4902	16.5		
Noname_6	35.99	82.86	4986	18.1		
Noname_7	35.54	83.13	4973	18.6		
Norma Co	32.39	88.05	4712	15.5		
Nyer Co	32.28	82.21	4398	25.2		
Orba Co	34.53	81.04	5194	14.8		
Ou Co	33.81	90.51	5065	14.6		

TABLE A6
(continued)

Lake or identifier	Latitude (°N)	Longitude (°E)	Elevation (m)	Mean monthly max. T (°C)*	Elevation (m)	Mean monthly max. T by elevation bin (°C)
Pa Co	31.91	90.04	4588	24.5		
Pagsum Co	30.02	93.97	4119	14.1		
Paiku Co	28.89	85.59	4585	13.2		
Palung Co	30.89	83.58	5101	12.1		
Pipa Lake	34.19	87.8	4937	16.9		
Pongyin Co	32.9	88.2	4732	14.9		
Pozi Co	30.47	86.11	4963	21.7		
Puga Co	31.11	89.55	4792	16.4		
Puma Yumco	28.57	90.39	5013	10.7		
Pung Co	31.51	90.97	4529	14.9		
Pur Co	34.88	81.96	5048	14.4		
Pusai'er Co	32.33	89.44	4588	19.8		
Puxu Co	31.91	87.21	4494	26.0		
Qagong Co	34.43	82.34	5095	15.2		
Qiagang Co	33.22	88.39	4758	16.1		
Qiagui Co	31.82	88.25	4553	16.0		
Qieli Co	31.68	90.97	4679	22.8		
Qige Co	31.2	85.53	4667	19.3		
Qingche Lake	34.48	81.79	5099	12.5		
Qinghai Lake	36.88	100.2	3194	15.4		
Qingwa Lake	34.71	86.4	4921	15.7		
Qiongjiang Lake	36.02	88.51	4850	16.1		
Qoiden Co	34.37	87.49	4883	16.4		
Quanshui Lake	34.76	80.18	5116	16.4		
Quemo Co	33.89	91.19	4962	13.2		
Rebang Co	33.03	80.58	4321	19.9		
Rejue Caka	33.69	86.84	4755	17.2		
Rena Co	32.73	84.26	4594	22.6		
Rigain Punco	32.58	86.24	4672	15.9		
Rige Co	34.33	98.75	4186	18.8		
Rijiu Co	34.2	91.69	4673	20.9		
Riju Co	33.8	90.36	4961	15.0		
Ringco Kongma	30.93	89.67	4656	14.8		
Ringco Ogma	30.93	89.83	4658	16.0		
Rinqin Xubco	31.28	83.45	4760	13.1		
Rola Co	35.41	88.37	4815	12.4		
S54001	36.18	89.15	4871	15.1		
S63005	35.95	90.83	5010	14.8		
S63022	35.23	91.21	4783	17.9		
Saleikuli Lake	37.44	73.69	4115	18.1		
Salt Water Lake	35.3	83.12	4889	12.3		
Sandao Lake	34.76	83.9	4948	13.6		
Sarezskoe Lake	38.26	72.79	5115	18.9		
Sekezhi Co	32	82.05	4570	26.2		
Selin Co	31.8	88.99	4539	13.6		
Sengli Co	30.44	84.06	5387	10.9		
Serbug Co	32	88.22	4515	15.6		
Shen Co	31.01	90.48	4734	16.9		
Shengli Lake	35.29	86.28	4874	16.5		
Shibu Co	31.39	88.72	4620	20.5		
Shiman Lake	36.25	86.11	5037	16.1		
Salt Water Lake	35.3	83.12	4889	12.3		
Sandao Lake	34.76	83.9	4948	13.6		
Sarezskoe Lake	38.26	72.79	5115	18.9		
Sekezhi Co	32	82.05	4570	26.2		
Selin Co	31.8	88.99	4539	13.6		
Sengli Co	30.44	84.06	5387	10.9		
Serbug Co	32	88.22	4515	15.6		
Shen Co	31.01	90.48	4734	16.9		
Shengli Lake	35.29	86.28	4874	16.5		
Shibu Co	31.39	88.72	4620	20.5		
Shiman Lake	36.25	86.11	5037	16.1		
Shiwa Lake	37.39	71.34	3404	23.2		
Shuanghu	34.47	83.16	5302	14.9		
Shuangju Lake	34.94	87.3	4795	23.7		
Shuixiang Lake	36.04	87.88	4886	20.5		
Sijia Lake	34.04	82.61	4883	17.5		
Songmuxi Co	34.61	80.25	5061	17.0		
Sugan Lake	38.87	93.88	2795	19.5		
Suona Lake	33.91	86.69	4822	19.3		
T54001	34.22	89.75	5041	14.1		
T54024	34.91	81.68	4947	19.0		
Taiping Lake	34.29	89.71	5086	13.3		
Taiyang Lake	35.93	90.63	4881	8.6		

TABLE A6

(continued)

Lake or identifier	Latitude (°N)	Longitude (°E)	Elevation (m)	Mean monthly max. T (°C)*	Elevation (m)	Mean monthly max. T by elevation bin (°C)
Tangra Yumco	31.07	86.61	4535	13.8		
Tao Lake	36.17	89.32	4879	12.2		
Tari Co	31.52	85.68	5049	14.4		
Taro Co	31.14	84.12	4567	13.5		
Telashi Lake	34.81	92.22	4805	11.2		
terang Punco	33.06	89.07	4846	21.1		
Tomgo Co	31.72	86.98	4604	18.1		
Tso moriri	32.9	78.31	4522	16.1		
Tu Co	33.4	89.86	4929	11.5		
Tungpu Co	31.31	87.23	4689	18.8		
Tuoheping Co	34.18	83.15	5021	14.3		
Tuosu Lake	37.14	96.94	2806	20.8		
Tuzhong Lake	34.53	84.7	5057	15.2		
Urru Co	31.72	88	4554	13.4		
Wan'an Lake	34.43	88.56	4941	17.3		
Wandou Lake	34.56	90.85	4858	13.8		
Wanquan Lake	34.24	83.82	4886	14.2		
Weishan Lake	35.96	89.23	4882	16.7		
Wuga Co	32	86.64	4472	27.4		
Wulanwula Lake	34.81	90.48	4902	11.3		
Xiabie Co	32.22	87.27	4600	18.4		
Xiabu Co	32.59	82.38	4351	23.6		
Xiaga Co	32.31	83.81	4356	24.2		
Xiajian Lake	34.16	82.78	4981	19.8		
Xiangtao Lake	34.14	84.97	4899	19.4		
Xiangyang Lake	35.8	89.42	4858	11.7		
Xianhe Lake	36	88.08	4858	12.6		
Xianqie Co	33.67	81.37	4664	22.8		
Xiao Caka	33.06	87.78	4793	18.5		
Xiaobei Lake	34.74	83.51	4962	24.3		
Xiaochaidan Lake	37.49	95.51	3173	19.4		
Xiaokusai Lake	36.08	92.8	4526	16.7		
Xiaoquan Lake	34.08	83.67	4860	16.7		
Xiaosugan Lake	39.06	94.21	2809	22.8		
Xiasa'er Co	31.58	80.99	5150	22.7		
Xijir Ulan Lake	35.21	90.34	4772	11.5		
Xiligou Lake	36.84	98.45	2938	22.9		
Xinhu Lake	34.39	84.25	4814	16.6		
Xinxin Lake	34.83	98.1	4263	20.7		
Xuehuan Lake	35.01	88.05	4825	14.9		
Xuejing Lake	35.98	87.37	4807	12.9		
Xuelian Lake	34.09	90.26	5275	9.3		
Xuemei Lake	36.29	88.27	4873	11.6		
Xuguo Co	31.95	90.34	4608	15.7		
Xuru Co	30.29	86.41	4714	12.6		
Yadao Lake	33.96	83.32	4898	16.2		
Yaggain Co	31.57	89.03	4534	15.1		
Yaggain Co1	33.01	89.79	4875	13.6		
Yaggain Co2	32.35	87.31	4991	12.6		
Yake Co	34.7	87.19	4907	24.0		
Yamzho Yumco	28.95	90.71	4540	16.1		
Yan Lake	35.53	93.41	4441	14.7		
Yanghong Lake	35.25	89.97	4770	14.0		
Yanghu Lake	35.43	84.64	4778	12.7		
Yangnapeng Co	32.33	89.77	4629	20.6		
Yanzi Lake	33.87	89.93	4973	16.1		
Yashilkul Lake	37.76	72.88	3733	19.0		
Yaxi Co	34.25	92.68	4504	17.6		
Yazi Lake	35.07	87.06	4791	15.4		
Yazi Lake(Woniu Lake)	35.72	85.27	4962	19.0		
Yelusu Lake	35.22	92.13	4688	12.0		
Yibug Caka	32.93	86.71	4558	15.7		
Yinbo Lake	36.19	88.14	4879	11.3		
Yingtian Lake	34.43	88.06	4828	17.8		
Yinlong Co	33.91	88.04	5080	14.7		
Yinma Lake	35.6	90.63	4987	10.6		
Yishan Lake	35.24	90.91	4877	14.7		
Yongbo Lake	34.96	89.23	4856	15.2		
Yongqin Co	32.36	87.06	4982	17.5		
Yoqag Co	30.47	88.61	4807	13.5		
Youyi Lake	34.46	88.74	4871	16.7		
Yuan Lake1	34.81	89.28	4888	19.0		
Yuan Lake2	33.95	85.34	4821	18.7		

TABLE A6

(continued)

Lake or identifier	Latitude (°N)	Longitude (°E)	Elevation (m)	Mean monthly max. T (°C)*	Elevation (m)	Mean monthly max. T by elevation bin (°C)
Yueliang Lake	35.61	90.38	4909	12.4		
Yueya Lake	34.92	82.22	5104	18.1		
Yuhuan Lake	35.74	86.69	4882	16.5		
Yupan Lake	34.9	88.39	4900	14.1		
Yuye Lake	36.01	88.78	4856	11.3		
Zainzong Co	32.24	89.61	4570	21.5		
Zhamucuomaqiong	33.15	89.7	4892	14.4		
Zhangnai Co	31.54	87.39	4606	15.9		
Zhangtoujiangmu Co	35.33	95.61	4395	19.0		
Zhaoyang Lake	35.3	87.25	4746	16.1		
Zhari Namco	30.93	85.62	4612	14.3		
Zhaxi Co	32.2	85.12	4416	18.3		
Zhenquan Lake	35.92	86.96	4792	12.9		
Zhuorang Co	34.96	97.48	4290	18.8		
Zige Tangco	32.08	90.86	4568	13.8		
Zigu Co	31.37	87.9	4648	13.7		
Ziru Co	32.17	86.2	4487	23.6		

MODIS-derived lakes, from data compiled by Wan and others (2017).

For the period of 2001-2015, Wan and others (2017) reported the monthly mean surface water temperature for 374 lakes with surface areas greater than 10 km^2.

In this study, we extracted the maximum monthly temperature for each of the 15 years, and took the mean of those annual monthly maximums (reported in asterisked column).

REFERENCES

Banner, J. L., and Hanson, G. N., 1990, Calculation of simultaneous isotopic and trace element variations during water-rock interaction with applications to carbonate diagenesis: Geochimica et Cosmochimica Acta, v. 54, n. 11, p. 3123–3137, https://doi.org/10.1016/0016-7037(90)90128-8

Berner, R. A., 1988, Early Diagenesis: A Theoretical Approach: Princeton, New Jersey, Princeton University Press, 241 p.

Bonifacie, M., Calmels, D., Eiler, J. M., Horita, J., Chaduteau, C., Vasconcelos, C., Agrinier, P., Katz, A., Passey, B. H., Ferry, J. M., and Bourrand, J. J., 2017, Calibration of the dolomite clumped isotope thermometer from 25 to 350 °C, and implications for a universal calibration for all (Ca, Mg, Fe)CO_3 carbonates: Geochimica et Cosmochimica Acta, v. 200, p. 255–279, https://doi.org/10.1016/j.gca.2016.11.028

Botsyun, S., Sepulchre, P., Donnadieu, Y., Risi, C., Licht, A., and Caves Rugenstein, J. K., 2019, Revised paleoaltimetry data show low Tibetan Plateau elevation during the Eocene: Science, v. 363, n. 6430, https://doi.org/10.1126/science.aaq1436

Brand, W. A., Assonov, S. S., and Coplen, T. B., 2010, Correction for the ^{17}O interference in $\delta(^{13}C)$ measurements when analyzing CO_2 with stable isotope mass spectrometry (IUPAC Technical Report): Pure and Applied Chemistry, v. 82, n. 8, p. 1719–1733, https://doi.org/10.1351/PAC-REP-09-01-05

Breecker, D. O., Sharp, Z. D., and McFadden, L. D., 2009, Seasonal bias in the formation and stable isotopic composition of pedogenic carbonate in modern soils from central New Mexico, USA: GSA Bulletin, v. 121, n. 3–4, p. 630–640, https://doi.org/10.1130/B26413.1

Budd, D. A., and Land, L. S., 1990, Geochemical imprint of meteoric diagenesis in Holocene ooid sands, Schooner Cays, Bahamas: Correlation of calcite cement geochemistry with extant groundwaters: Journal of Sedimentary Petrology, v. 60, n. 3, p. 361–378, https://doi.org/10.1306/212F919C-2B24-11D7-8648000102C1865D

Bureau of Geology and Mineral Resources Xizang Autonomous Region, 1992, Regional geology of Xizang (Tibet) autonomous region: Geological Publishing House.

Burgener, L., Huntington, K. W., Hoke, G. D., Schauer, A., Ringham, M. C., Latorre, C., and Díaz, F. P., 2016, Variations in soil carbonate formation and seasonal bias over >4 km of relief in the western Andes (30°S) revealed by clumped isotope thermometry: Earth and Planetary Science Letters, v. 441, p. 188–199, https://doi.org/10.1016/j.epsl.2016.02.033

Cerling, T. E., and Quade, J., 1993, Stable carbon and oxygen isotopes in soil carbonates, *in* Swart, P. K., Lohmann, K. C., McKenzie, J., and Savin, S., editors, Climate Change in Continetnal Isotopic Records: Geophysical Monograph Series, v. 78, p. 217–231, https://doi.org/10.1029/GM078p0217

Chamberlain, C. P., and Poage, M. A., 2000, Reconstructing the paleotopography of mountain belts from the isotopic composition of authigenic minerals: Geology, v. 28, n. 2, p. 115–118, https://doi.org/10.1130/0091-7613(2000)028<0115:RTPOMB>2.3.CO;2

Chengfa, C., Nansheng, C., Coward, M. P., Wanming, D., Dewey, J. F., Gansser, A., Harris, N. B. W., Chengwei, J., Kidd, W. S. F., Leeder, M. R., Huan, L., Jinlu, L., Chengjie, L., Houjun, M., Molnar, P., Yun, P., Yusheng, P., Pearce, J. A., Shackleton, R. M., Smith, A. B., Yiyin, S., Ward, M., Watts, D. R., Juntao, X., Ronghua, X., Jixiang, Y., and Yuquan, Z., 1986, Preliminary conclusions of the Royal Society and Academia Sinica 1985 geotraverse of Tibet: Nature, v. 323, p. 501–507, https://doi.org/10.1038/323501a0

Coplen, T. B., Brand, W. A., Gehre, M., Gröning, M., Meijer, H. A. J., Toman, B., and Verkouteren, R. M., 2006, New guidelines for $\delta^{13}C$ measurements: Analytical Chemistry, v. 78, n. 7, p. 2439–2441, https://doi.org/10.1021/ac052027c

Craig, H., 1961, Isotopic variations in meteoric waters: Science, v. 133, n. 3465, p. 1702–1703, ttps://doi.org/10.1126/science.133.3465.1702

Craig, H., and Gordon, L., 1965, Deuterium and oxygen 18 variations in the ocean and the marine atmosphere, *in* Tongiorgi, E., editor, Stable Isotopes in Oceanographic Studies and Paleotemperatures: Spolito, Italy, Consiglio Nazionale di Recherche, p. 9–130.

Craig, H., Gordon, L. I., and Horibe, Y., 1963, Isotopic exchange effects in the evaporation of water: 1. Low-temperature experimental results: Journal of Geophysical Research, v. 68, n. 17, p. 5079–5087, https://doi.org/10.1029/JZ068i017p05079

Currie, B. S., Polissar, P. J., Rowley, D. B., Ingalls, M., Li, S., Olack, G., and Freeman, K. H., 2016, Multiproxy paleoaltimetry of the late Oligocene-Pliocene Oiyug Basin, southern Tibet: American Journal of Science, v. 316, n. 5, p. 401–436, https://doi.org/10.2475/05.2016.01

DeCelles, P. G., Kapp, P., Ding, L., and Gehrels, G. E., 2007a, Late Cretaceous to middle Tertiary basin evolution in the central Tibetan Plateau: Changing environments in response to tectonic partitioning, aridification, and regional elevation gain: GSA Bulletin, v. 119, n. 5–6, p. 654–680, https://doi.org/10.1130/B26074.1

DeCelles, P. G., Quade, J., Kapp, P., Fan, M., Dettman, D. L., and Ding, L., 2007b, High and dry in central Tibet during the Late Oligocene: Earth and Planetary Science Letters, v. 253, n. 3–4, p. 389–401, https://doi.org/10.1016/j.epsl.2006.11.001

DeCelles, P. G., Kapp, P., Quade, J., and Gehrels, G. E., 2011, Oligocene-Miocene Kailas basin, southwestern Tibet: Record of postcollisional upper-plate extension in the Indus-Yarlung suture zone: GSA Bulletin, v. 123, n. 7–8, p. 1337–1362, https://doi.org/10.1130/B30258.1

DeCelles, P., Kapp, P., Gehrels, G. E., and Ding, L., 2014, Paleocene-Eocene foreland basin evolution in the Himalaya of southern Tibet and Nepal: Implications for the age of initial India-Asia collision: Tectonics, v. 33, n. 5, p. 824–849, https://doi.org/10.1002/2014TC003522

DeCelles, P. G., Castaneda, I. S., Carrapa, B., Liu, J., Quade, J., Leary, R., and Zhang, L., 2018, Oligocene-Miocene Great Lakes in the India-Asia Collision Zone: Basin Research, v. 30, n. S1, p. 228–247, https://doi.org/10.1111/bre.12217

Deng, L., and Jia, G., 2018, High-relief topography of the Nima basin in central Tibetan Plateau during the mid-Cenozoic time: Chemical Geology, v. 493, p. 199–209, https://doi.org/10.1016/j.chemgeo.2018.05.041

Dennis, K. J., Affek, H. P., Passey, B. H., Schrag, D. P., and Eiler, J. M., 2011, Defining an absolute reference frame for 'clumped' isotope studies of CO_2: Geochimica et Cosmochimica Acta, v. 75, n. 22, p. 7117–7131, https://doi.org/10.1016/j.gca.2011.09.025

Ding, L., and Lai, Q., 2003, New geological evidence of crustal thickening in the Gangdese block prior to the Indo-Asian collision: Chinese Science Bulletin, v. 48, p. 1604–1610, https://doi.org/10.1007/BF03183969

Ding, L., Xu, Q., Yue, Y., Wang, H., Cai, F., and Li, S., 2014, The Andean-type Gangdese Mountains: Paleoelevation record from the Paleocene–Eocene Linzhou Basin: Earth and Planetary Science Letters, v. 392, p. 250–264, https://doi.org/10.1016/j.epsl.2014.01.045

Drever, J. I., 1982, The Geochemistry of Natural Waters: Upper Saddle River, New Jersey, Prentice Hall, 388 p.

Eagle, R. A., Schauble, E. A., Tripati, A. K., Tütken, T., Hulbert, R. C., Eiler, J. M., Tutken, T., Hulbert, R. C., and Eiler, J. M., 2010, Body temperatures of modern and extinct vertebrates from ^{13}C-^{18}O bond abundances in bioapatite: Proceedings of the National Academy of Sciences of the United States of America, v. 107, n. 23, p. 10377–10382, https://doi.org/10.1073/pnas.0911115107

England, P., and Searle, M., 1986, The Cretaceous-Tertiary deformation of the Lhasa Block and its implications for crustal thickening in Tibet: Tectonics, v. 5, n. 1, p. 1–14, https://doi.org/10.1029/TC005i001p00001

Fan, M., and Carrapa, B., 2014, Late Cretaceous-early Eocene Laramide uplift, exhumation, and basin subsidence in Wyoming: Crustal responses to flat slab subduction: Tectonics, v. 33, n. 4, p. 509–529, https://doi.org/10.1002/2012TC003221

Fricke, H. C., and Wing, S. L., 2004, Oxygen isotope and paleobotanical estimates of temperature and $\delta^{18}O$-latitude gradients over North America during the early Eocene: American Journal of Science, v. 304, n. 7, p. 612–635, https://doi.org/10.2475/ajs.304.7.612

Gallagher, T. M., and Sheldon, N. D., 2016, Combining soil water balance and clumped isotopes to understand the nature and timing of pedogenic carbonate formation: Chemical Geology, v. 435, p. 79–91, https://doi.org/10.1016/j.chemgeo.2016.04.023

Gehler, A., Tütken, T., and Pack, A., 2011, Triple oxygen isotope analysis of bioapatite as tracer for diagenetic alteration of bones and teeth: Palaeogeography, Palaeoclimatology, Palaeoecology, v. 310, n. 1–2, https://doi.org/10.1016/j.palaeo.2011.04.014

Gérard, E., Ménez, B., Couradeau, E., Moreira, D., Benzerara, K., Tavera, R., and López-García, P., 2013, Specific carbonate-microbe interactions in the modern microbialites of Lake Alchichica (Mexico): The ISME Journal, v. 7, p. 1997–2009, https://doi.org/10.1038/ismej.2013.81

Ghosh, P., Adkins, J., Affek, H., Balta, B., Guo, W. W., Schauble, E. A., Schrag, D., and Eiler, J. M., 2006a, ^{13}C-^{18}O bonds in carbonate minerals: A new kind of paleothermometer: Geochimica et Cosmochimica Acta, v. 70, n. 6, p. 1439–1456, https://doi.org/10.1016/j.gca.2005.11.014

Ghosh, P., Garzione, C. N., and Eiler, J. M., 2006b, Rapid uplift of the Altiplano revealed through ^{13}C-^{18}O bonds in paleosol carbonates: Science, v. 311, n. 5760, p. 511–515, https://doi.org/10.1126/science.1119365

Ghosh, P., Eiler, J., Campana, S. E., and Feeney, R. F., 2007, Calibration of the carbonate 'clumped isotope' paleothermometer for otoliths: Geochimica et Cosmochimica Acta, v. 71, n. 11, https://doi.org/10.1016/j.gca.2007.03.015

Gonfiantini, R., 1986, Environmental Isotopes in Lake Studies, *in* Handbook of Environemtal Isotope Geochemistry, Volume 2: The Terrestrial Environment B, p. 113–168, https://doi.org/10.1016/B978-0-444-42225-5.50008-5

Gourbet, L., Leloup, P. H., Paquette, J.-L., Sorrel, P., Maheo, G., Wang, G., Yadong, X., Cao, K., Antoine, P.-O., Eymard, I., Liu, W., Lu, H., Replumaz, A., Chevalier, M.-L., Kexin, Z., Jing, W., and Shen, T., 2017, Reappraisal of the Jianchuan Cenozoic basin stratigraphy and its implications on the SE Tibetan plateau evolution: Tectonophysics, v. 700–701, p. 162–179, https://doi.org/10.1016/j.tecto.2017.02.007

Guo, W., Mosenfelder, J. L., Goddard III, W. A., and Eiler, J. M., 2009, Isotopic fractionations associated with phosphoric acid digestion of carbonate minerals: Insights from first-principles theoretical modeling and clumped isotope measurements: Geochimica et Cosmochimica Acta, v. 73, n. 24, p. 7203–7225, https://doi.org/10.1016/j.gca.2009.05.071

Haider, V. L., Dunkl, I., von Eynatten, H., Ding, L., Frei, D., and Zhang, L., 2013, Cretaceous to Cenozoic evolution of the northern Lhasa Terrane and the Early Paleogene development of peneplains at Nam Co, Tibetan Plateau: Journal of Asian Earth Sciences, v. 70–71, p. 79–98, https://doi.org/10.1016/j.jseaes.2013.03.005

Han, Z., Xu, M., Li, Y., Wei, Y., and Wang, C., 2014, Paleocene-Eocene potential source rocks in the Avengco Basin, Tibet: Organic geochemical characteristics and their implication for the paleoenvironment: Journal of Asian Earth Sciences, v. 93, p. 60–73, https://doi.org/10.1016/j.jseaes.2014.06.027

He, H., Sun, J., Li, Q., and Zhu, R., 2011, New age determination of the Cenozoic Lunpola basin, central Tibet: Geological Magazine, v. 149, n. 1, p. 141–145, https://doi.org/10.1017/S0016756811000896

He, S., Kapp, P., DeCelles, P. G., Gehrels, G. E., and Heizler, M., 2007, Cretaceous-Tertiary geology of the Gangdese Arc in the Linzhou area, southern Tibet: Tectonophysics, v. 433, n. 1–2, p. 15–37, https://doi.org/10.1016/j.tecto.2007.01.005

Hetzel, R., Dunkl, I., Haider, V., Strobl, M., von Eynatten, H., Ding, L., and Frei, D., 2011, Peneplain formation in southern Tibet predates the India-Asia collision and plateau uplift: Geology, v. 39, n. 10, p. 983–986, https://doi.org/10.1130/G32069.1

Hillel, D., 1982, Introduction to Soil Physics: New York, Academic Press, 392 p.

Horita, J., 2014, Oxygen and carbon isotope fractionation in the system dolomite-water-CO_2 to elevated temperatures: Geochimica et Cosmochimica Acta, v. 129, p. 111–124, https://doi.org/10.1016/j.gca.2013.12.027

Hough, B., Fan, M., and Passey, B. H., 2014, Calibration of the clumped isotope geothermometer in soil carbonate in Wyoming and Nebraska, USA: Implications for paleoelevation and paleoclimate reconstruction: Earth and Planetary Science Letters, v. 391, p. 110–120, https://doi.org/10.1016/j.epsl.2014.01.008

Hudson, A. M., Quade, J., Ali, G., Boyle, D., Bassett, S., Huntington, K. W., De los Santos, M. G., Cohen, A. S., Lin, K., and Wang, X., 2017, Stable C, O and clumped isotope systematics and ^{14}C geochronology of carbonates from the Quaternary Chewaucan closed-basin lake system, Great Basin, USA: Implications for paleoenvironmental reconstructions using carbonates: Geochimica et Cosmochimica Acta, v. 212, p. 274–302, https://doi.org/10.1016/j.gca.2017.06.024

Huntington, K. W., and Lechler, A. R., 2015, Carbonate clumped isotope thermometry in continental tectonics: Tectonophysics, v. 647–648, p. 1–20, https://doi.org/10.1016/j.tecto.2015.02.019

Huntington, K. W., Eiler, J. M., Affek, H. P., Guo, W., Bonifacie, M., Yeung, L. Y., Thiagarajan, N., Passey, B., Tripati, A., Daëron, M., and Came, R., 2009, Methods and limitations of 'clumped' CO_2 isotope (Δ_{47}) analysis by gas-source isotope ratio mass spectrometry: Journal of Mass Spectrometry, v. 44, n. 9, p. 1318–29, https://doi.org/10.1002/jms.1614

Huntington, K. W., Wernicke, B. P., and Eiler, J. M., 2010, Influence of climate change and uplift on Colorado Plateau paleotemperatures from carbonate clumped isotope thermometry: Tectonics, v. 29, n. 3, https://doi.org/10.1029/2009TC002449

Huntington, K. W., Budd, D. A., Wernicke, B. P., and Eiler, J. M., 2011, Use of clumped-isotope thermometry to constrain the crystallization temperature of diagenetic calcite: Journal of Sedimentary Research, v. 81, n. 9, p. 656–669, https://doi.org/10.2110/jsr.2011.51

Huntington, K. W., Saylor, J., Quade, J., and Hudson, A. M., 2015, High late Miocene-Pliocene elevation of the Zhada Basin, southwestern Tibetan Plateau, from carbonate clumped isotope thermometry: GSA Bulletin, v. 127, n. 1–2, p. 181–199, https://doi.org/10.1130/B31000.1

Ingalls, M., 2019, Reconstructing carbonate alteration histories in orogenic sedimentary basins: Xigaze forearc, southern Tibet: Geochimica et Cosmochimica Acta, v. 251, p. 284–300, https://doi.org/10.1016/j.gca.2019.02.005

Ingalls, M., Rowley, D., Olack, G., Currie, B., Li, S., Schmidt, J., Tremblay, M., Polissar, P, Shuster, D. L., Lin, D., and Colman, A., 2017, Paleocene to Pliocene low-latitude, high-elevation basins of southern Tibet: Implications for tectonic models of India-Asia collision, Cenozoic climate, and geochemical weathering: GSA Bulletin, v. 130, n. 1–2, p. 307–330, https://doi.org/10.1130/B31723.1

Ingalls, M., Frantz, C. M., Snell, K. E., and Trower, E. J., 2020, Carbonate facies-specific stable isotope data record climate, hydrology, and microbial communities in Great Salt Lake, UT: Geobiology, p. 28, https://doi.org/10.1111/gbi.12386

Jia, G., Bai, Y., Ma, Y., Sun, J., and Peng, P., 2015, Paleoelevation of Tibetan Lunpola basin in the Oligocene-Miocene transition estimated from leaf wax lipid dual isotopes: Global and Planetary Change, v. 126, p. 14–22, http://dx.doi.org/10.1016/j.gloplacha.2014.12.007

Kapp, P., DeCelles, P. G., Leier, A. L., Fabijanic, J. M., He, S., Pullen, A., Gehrels, G. E., and Ding, L., 2007, The Gangdese retroarc thrust belt revealed: GSA Today, v. 17, n. 7, p. 4–9, https://doi.org/10.1130/GSAT01707A.1

Keating-Bitonti, C. R., Ivany, L. C., Affek, H. P., Douglas, P., and Samson, S. D., 2011, Warm, not super-hot, temperatures in the early Eocene subtropics: Geology, v. 39, n. 8, p. 771–774, https://doi.org/10.1130/G32054.1

Kelson, J. R., Huntington, K. W., Schauer, A. J., Saenger, C., and Lechler, A. R., 2017, Toward a universal carbonate clumped isotope calibration: Diverse synthesis and preparatory methods suggest a single temperature relationship: Geochimica et Cosmochimica Acta, v. 197, p. 104–131, https://doi.org/10.1016/j.gca.2016.10.010

Kim, S.-T., and O'Neil, J. R., 1997, Equilibrium and nonequilibrium oxygen isotope effects in synthetic carbonates: Geochimica et Cosmochimica Acta, v. 61, n. 16, p. 3461–3475, https://doi.org/10.1016/S0016-7037(97)00169-5

Kirillin, G., Wen, L., and Shatwell, T., 2017, Seasonal thermal regime and climatic trends in lakes of the Tibetan highlands: Hydrology and Earth System Sciences, v. 21, n. 4, https://doi.org/10.5194/hess-2016-632-AC2

Lacroix, B., and Niemi, N. A., 2019, Investigating the effect of burial histories on the clumped isotope thermometer: An example from the Green River and Washakie Basins, Wyoming: Geochimica et Cosmochimica Acta, v. 247, p. 40–58, https://doi.org/10.1016/j.gca.2018.12.016

Leier, A., Quade, J., DeCelles, P., and Kapp, P., 2009, Stable isotopic results from paleosol carbonate in South Asia: Paleoenvironmental reconstructions and selective alteration: Earth and Planetary Science Letters, v. 279, n. 3–4, p. 242–254, https://doi.org/10.1016/j.epsl.2008.12.044

Leng, M. J., and Marshall, J. D., 2004, Palaeoclimate interpretation of stable isotope data from lake sediment archives: Quaternary Science Reviews, v. 23, n. 7–8, p. 811–831, https://doi.org/10.1016/j.quascirev.2003.06.012

Levin, N. E., Zipser, E. J., and Cerling, T. E., 2009, Isotopic composition of waters from Ethiopia and Kenya: Insights into moisture sources for eastern Africa: Journal of Geophysical Research-Atmospheres, v. 114, n. D23, https://doi.org/10.1029/2009JD012166

Li, L., Fan, M., Davila, N., Jesmok, G., Mitsunaga, B., Tripati, A., and Orme, D., 2019, Carbonate stable and clumped isotopic evidence for late Eocene moderate to high elevation of the east-central Tibetan Plateau and its geodynamic implications: GSA Bulletin, v. 131, n. 56, p. 831–844, https://doi.org/10.1130/B32060.1

Li, S., Currie, B. S., Rowley, D. B., and Ingalls, M., 2015, Cenozoic paleoaltimetry of the SE margin of the

Tibetan Plateau: Constraints on the tectonic evolution of the region: Earth and Planetary Science Letters, v. 432, p. 415–424, https://doi.org/10.1016/j.epsl.2015.09.044
Liu, J., Song, X., Yuan, G., Sun, X., and Yang, L., 2014, Stable isotopic compositions of precipitation in China: Tellus B: Chemical and Physical Meterology, v. 66, n. 1, https://doi.org/10.3402/tellusb.v66.22567
Lloyd, M. K., 2020, ClumpyCool: Open Science Framework, doi: 10.17605/OSF.IO/JYHSW.
Lunt, D. J., Farnsworth, A., Loptson, C., Foster, G. L., Markwick, P., O'Brien, C. L., Pancost, R. D., Robinson, S. A., and Wrobel, N., 2016, Palaeogeographic controls on climate and proxy interpretation: Climate of the Past, v. 12, p. 1181–1198, https://doi.org/10.5194/cp-12-1181-2016
Luz, B., and Barkan, E., 2010, Variations of $^{17}O/^{16}O$ and $^{18}O/^{16}O$ in meteoric waters: Geochimica et Cosmochimica Acta, v. 74, n. 22, p. 6276–6286, https://doi.org/10.1016/j.gca.2010.08.016
Ma, P., Wang, C., Wang, L., Li, Y., and Hu, J., 2015, Sedimentology and organic properties of lower Tertiary lacustrine source rocks, Lunpola Basin, central Tibetan Plateau: Implications for hydrocarbon potential: Marine and Petroleum Geology, v. 66, Part 4, p. 1029–1041, https://doi.org/10.1016/j.marpetgeo.2015.08.013
Ma, P., Wang, C., Meng, J., Ma, C., Zhao, X., Li, Y., and Wang, M., 2017, Late Oligocene-early Miocene evolution of the Lunpola Basin, central Tibetan Plateau, evidences from successive lacustrine records: Gondwana Research, v. 48, p. 224–236, https://doi.org/10.1016/j.gr.2017.04.023
Mao, Z., Meng, Q., Fang, X., Zhang, T., Wu, F., Yang, Y., Zhang, W., Zan, J., and Tan, M., 2019, Recognition of tuffs in the middle-upper Dingqinghu Fm., Lunpola Basin, central Tibetan Plateau: Constraints on stratigraphic age and implications for paleoclimate: Palaeogeography, Palaeoclimatology, Palaeoecology, v. 525, p. 44–56, https://doi.org/10.1016/j.palaeo.2019.03.040
McConnaughey, T. A., 2003, Sub-equilibrium oxygen-18 and carbon-13 levels in biological carbonates: Carbonate and kinetic models: Coral Reefs, v. 22, p. 316–327, https://doi.org/10.1007/s00338-003-0325-2
Mills, G. A., and Urey, H. C., 1940, The Kinetics of Isotopic Exchange between Carbon Dioxide, Bicarbonate Ion, Carbonate Ion and Water: Journal of the American Chemical Society, v. 62, n. 5, https://doi.org/10.1021/ja01862a010
Molnar P., and England, P., 1990, Late Cenozoic uplift of mountain ranges and global climate change: Nature, v. 346, p. 29–34, https://doi.org/10.1038/346029a0
Mortimer, R. J. G., and Coleman, M. L., 1997, Microbial influence on the oxygen isotopic composition of diagenetic siderite: Geochimica et Cosmochimica Acta, v. 61, n. 8, p. 1705–1711, https://doi.org/10.1016/S0016-7037(97)00027-6
Murphy, M. A., Yin, A., Harrison, T. M., Dürr, S. B., Chen, Z., Ryerson, F. J., Kidd, W. S. F., Wang, X., and Zhou, X., 1997, Did the Indo-Asian collision alone create the Tibetan plateau?: Geology, v. 25, n. 8, p. 719–722, https://doi.org/10.1130/0091-7613(1997)025<0719:DTIACA>2.3.CO;2
Myrttinen, A., Becker, V., and Barth, J. A. C., 2012, A review of methods used for equilibrium isotope fractionation investigations between dissolved inorganic carbon and CO_2: Earth-Science Reviews, v. 115, n. 3, p. 192–199, https://doi.org/10.1016/j.earscirev.2012.08.004
Orme, D. A., 2019, Burial and exhumation history of the Xigaze forearc basin, Yarlung suture zone, Tibet: Geoscience Frontiers, v. 10, n. 3, p. p. 895–908, https://doi.org/10.1016/j.gsf.2017.11.011
Passey, B. H., and Henkes, G. A., 2012, Carbonate clumped isotope bond reordering and geospeedometry: Earth and Planetary Science Letters, v. 351–352, p. 223–236, https://doi.org/10.1016/j.epsl.2012.07.021
Passey, B. H., Levin, N. E., Cerling, T. E., Brown, F. H., and Eiler, J. M., 2010, High-temperature environments of human evolution in East Africa based on bond ordering in paleosol carbonates: Proceedings of the National Academy of Sciences of the United States of America, v. 107, n. 25, p. 11245–11249, https://doi.org/10.1073/pnas.1001824107
Passey, B. H., Hu, H., Ji, H., Montanari, S., Li, S., Henkes, G. A., and Levin, N. E., 2014, Triple oxygen isotopes in biogenic and sedimentary carbonates: Geochimica et Cosmochimica Acta, v. 141, p. 1–25, https://doi.org/10.1016/j.gca.2014.06.006
Peppe, D. J., Royer, D. L., Cariglino, B., Oliver, S. Y., Newman, S., Leight, E., Enikolopov, G., Fernandez-Burgos, M., Herrera, F., Adams, J. M., Correa, E., Currano, E. D., Erickson, J. M., Hinojosa, L. F., Horganson, J. W., Iglesias, A., Jaramillo, C.A., Johnson, K. R., Jordan, G. J., Kraft, N. J. B., Lovelock, E. C., Lusk, C. H., Niinemets, U., Peñuelas, Rapson, G., Wing, S. L., and Wright, I. J., 2011, Sensitivity of leaf size and shape to climate: Global patterns and paleoclimatic applications: New Phytologist, v. 190, n. 3, https://doi.org/10.1111/j.1469-8137.2010.03615.x
Peppe, D. J., Baumgartner, A., Flynn, A., and Blonder, B., 2018, Reconstructing paleoclimate and paleoecology using fossil leaves, *in* Vertebrate Paleobiology and Paleoanthropology: PaleorXiv, https://doi.org/10.31233/osf.io/stzuc
Peters, N. A ., Huntington, K. W., and Hoke, G. D., 2013, Hot or not? Impact of seasonally variable soil carbonate formation on paleotemperature and O-isotope records from clumped isotope thermometry: Earth and Planetary Science Letters, v. 361, p. 208–218, https://doi.org/10.1016/j.epsl.2012.10.024
Petryshyn, V. A., Lim, D., Laval, B. L., Brady, A., Slater, G., and Tripati, A. K., 2015, Reconstruction of limnology and microbialite formation conditions from carbonate clumped isotope thermometry: Geobiology, v. 13, n. 1, p. 53–67, https://doi.org/10.1111/gbi.12121
Polissar, P. J., and Freeman, K. H., 2010, Effects of aridity and vegetation on plant-wax δD in modern lake sediments: Geochimica et Cosmochimica Acta, v. 74, n. 20, p. 5785–5797, https://doi.org/10.1016/j.gca.2010.06.018
Polissar, P. J., Freeman, K. H., Rowley, D. B., McInerney, F. A., and Currie, B. S., 2009, Paleoaltimetry of the Tibetan Plateau from D/H ratios of lipid biomarkers: Earth and Planetary Science Letters, v. 287, n. 1–2, p. 64–76, https://doi.org/10.1016/j.epsl.2009.07.037
Prior, D. J., Boyle, A. P., Brenker, F., Cheadle, M. C., Day, A., Lopez, G., Peruzzi, L., Potts, G. J., Reddy, S., Spiess, R., Timms, N. E., Trimby, P., Wheeler, J., and Zetterström, L., 1999, The application of electron

backscatter diffraction and orientation contrast imaging in the SEM to textural problems in rocks: American Mineralogist, v. 84, n. 11–12, p. 1741–1759, https://doi.org/10.2138/am-1999-11-1204
Quade, J., Breecker, D. O., Daëron, M., and Eiler, J. M., 2011, The paleoaltimetry of Tibet: An isotopic perspective: American Journal of Science, v. 311, n. 2, p. 77–115, https://doi.org/10.2475/02.2011.01
Quade, J., Eiler, J., Daëron, M., and Achyuthan, H., 2013, The clumped isotope geothermometer in soil and paleosol carbonate: Geochimica et Cosmochimica Acta, v. 105, p. 92–107, https://doi.org/10.1016/j.gca.2012.11.031
Quade, J., Leary, R., Dettinger, M. P., Orme, D., Krupa, A., DeCelles, P. G., Kano, A., Kato, H., Waldrip, R., Huang, W., and Kapp, P., 2020, Resetting Southern Tibet: The serious challenge of obtaining primary records of Paleoaltimetry: Global and Planetary Change, v. 191, p. 103194, https://doi.org/10.1016/j.gloplacha.2020.103194
Ringham, M. C., Hoke, G. D., Huntington, K. W., and Aranibar, J. N., 2016, Influence of vegetation type and site-to-site variability on soil carbonate clumped isotope records, Andean piedmont of Central Argentina (32–34°S): Earth and Planetary Science Letters, v. 440, p. 1–11, https://doi.org/10.1016/j.epsl.2016.02.003
Rowley, D. B., 2007, Stable Isotope-Based Paleoaltimetry: Theory and Validation: Reviews in Mineralogy and Geochemistry, v. 66, n. 1, p. 23–52, https://doi.org/10.2138/rmg.2007.66.2
——— 2019, Comparing paleomagnetic study means with apparent wander paths: A case study and paleomagnetic test of the Greater India versus Greater Indian Basin hypotheses: Tectonics, v. 38, n. 2, p. 722–740, https://doi.org/10.1029/2017TC004802
Rowley, D. B., and Currie, B. S., 2006, Palaeo-altimetry of the late Eocene to Miocene Lunpola basin, central Tibet: Nature, v. 439, p. 677–81, https://doi.org/10.1038/nature04506
Rowley, D. B., Pierrehumbert, R. T., and Currie, B. S., 2001, A new approach to stable isotope-based paleoaltimetry: Implications for paleoaltimetry and paleohypsometry of the High Himalaya since the Late Miocene: Earth and Planetary Science Letters, v. 188, n. 1–2, p. 253–268, https://doi.org/10.1016/S0012-821X(01)00324-7
Rozanski, K., Araguas-Araguas, L., and Gonfiantini, R., 1993, Isotopic patterns in modern global precipitation, *in* Cliamte Change in Continental Isotopic Records: Geophysical Monograph Series, v. 78, p. 1–36, https://doi.org/10.1029/GM078p0001
Shelley, D., 1993, Igneous and metamorphic rocks under the microscope: Classification, textures, microstructures, and mineral preferred-orientations: London, Chapman and Hall, 468 p.
Shen, X., 1993, Kinematics and tectonothermal modeling-interpretation of heat flow observed on the Tibetan Plateau: Tectonophysics, v. 225, n. 1–2, p. 91–106, https://doi.org/10.1016/0040-1951(93)90251-E
Snell, K. E., Thrasher, B. L., Eiler, J. M., Koch, P. L., Sloan, L. C., and Tabor, N. J., 2013, Hot summers in the Bighorn Basin during the early Paleogene: Geology, v. 41, n. 1, p. 55–58, https://doi.org/10.1130/G33567.1
Stolper, D. A., and Eiler, J. M., 2015, The kinetics of solid-state isotope-exchange reactions for clumped isotopes: A study of inorganic calcites and apatites from natural and experimental samples: American Journal of Science, v. 315, n. 5, p. 363–411, https://doi.org/10.2475/05.2015.01
Stumm, W., and Morgan, J. J., 1981, Aquatic chemistry: An introduction emphasizing chemical equilibria in natural waters: New York, Wiley-Interscience, 583 p.
Su, T., Farnsworth, A., Spicer, R. A., Huang, J., Wu, F. X., Liu, J., Li, S. F., Xing, Y. W., Huang, Y. J., Deng, W. Y. D., Tang, H., Xu, C. L., Zhao, F., Srivastava, G., Valdes, P. J., Deng, T., and Zhou, Z. K., 2019, No high tibetan plateau until the Neogene: Science Advances, v. 5, n. 3, https://doi.org/10.1126/sciadv.aav2189
Sun, B., Wang, Y., Li, C., Yang, J., Li, J., Li, Y., Deng, T., Wang, S., Zhao, M., Spicer, R. A., Ferguson, D. K., and Mehrotra, R. C., 2015, Early Miocene elevation in northern Tibet estimated by palaeobotanical evidence: Scientific Reports 5, article number 10379, p. 1–6, https://doi.org/10.1038/srep10379
Sun, J., Xu, Q., Liu, W., Zhang, Z., Xue, L., and Zhao, P., 2014b, Palynological evidence for the latest Oligocene – early Miocene paleoelevation estimate in the Lunpola Basin, central Tibet: Palaeogeography, Palaeoclimatology, Palaeoecology, v. 399, p. 21–30, https://doi.org/10.1016/j.palaeo.2014.02.004
Sun, T., Wang, C., Duan, Y., Li, Y., and Hu, B., 2014a, The organic geochemistry of the Eocene–Oligocene black shales from the Lunpola Basin, central Tibet: Journal of Asian Earth Sciences, v. 79, Part A, p. 468–476, https://doi.org/10.1016/j.jseaes.2013.09.034
Sun, X., Zhao, Y., and He, Z., 1984, Oligocene–Miocene sporopollen assemblages in Xining-Minhe basins of Qinghai Province: Geological Review, v. 30, n. 3, p. 207–215.
Swart, P. K., 2015, The geochemistry of carbonate diagenesis: The past, present and future: Sedimentology, v. 62, n. 5, p. 1233–1304, https://doi.org/10.1111/sed.12205
Talbot, M. R., 1990, A review of the palaeohydrological interpretation of carbon and oxygen isotopic ratios in primary lacustrine carbonates: Chemical Geology, v. 80, n. 4, p. 261–279, https://doi.org/10.1016/0168-9622(90)90009-2
Tang, M., Liu-Zeng J., Hoke, G. D., Xu, Q., Wang, W., Li, Z., Zhang, J., and Wang, W., 2017, Paleoelevation reconstruction of the Paleocene-Eocene Gonjo Basin, SE-central Tibet: Tectonophysics, v. 712–713, p. 170–181. https://doi.org/10.1016/j.tecto.2017.05.018.
Tao, D., Shiqi, W., Xie, G. P., Li, Q., Hou, S. K., and Sun, B. Y., 2012, A mammalian fossil from the Dingqing Formation in the Lunpola Basin, northern Tibet, and its relevance to age and paleo-altimetry: Chinese Science Bulletin, v. 57, p. 261–269, https://doi.org/10.1007/s11434-011-4773-8
Taylor, M., Yin, A., Ryerson, F. J., Kapp, P., and Ding, L., 2003, Conjugate strike-slip faulting along the Bangong-Nujiang suture zone accommodates coeval east-west extension and north-south shortening in the interior of the Tibetan Plateau: Tectonics, v. 22, n. 4, p. 7407–7407, https://doi.org/10.1029/2002TC001361

Thaler, C., Millo, C., Ader, M., Chaduteau, C., Guyot, F., and Ménez, B., 2017, Disequilibrium $\delta^{18}O$ values in microbial carbonates as a tracer of metabolic production of dissolved inorganic carbon: Geochimica et Cosmochimica Acta, v. 199, p. 112–129, https://doi.org/10.1016/j.gca.2016.10.051

Thiagarajan, N., Adkins, J., and Eiler, J., 2011, Carbonate clumped isotope thermometry of deep-sea corals and implications for vital effects: Geochimica et Cosmochimica Acta, v. 75, n. 16, p. 4416–4425, https://doi.org/10.1016/j.gca.2011.05.004

van Hinsbergen, D. J. J., Kapp, P., Dupont-Nivet, G., Lippert, P. C., DeCelles, P. G., and Torsvik, T. H., 2011, Restoration of Cenozoic deformation in Asia and the size of Greater India: Tectonics, v. 30, n. 5, p. TC5003, https://doi.org/10.1029/2011TC002908

Veizer, J., and Mackenzie, F. T., 2003, Evolution of Sedimentary Rocks, *in* Mackenzie, F. T., editor, Sediments, Diagenesis, and Sedimentary Rocks: Treatise on Geochemistry, v. 7, p. 369–407, https://doi.org/10.1016/B0-08-043751-6/07103-6

Vogel, J. C., Grootes, P. M., and Mook, W. G., 1970, Isotopic fractionation between gaseous and dissolved carbon dioxide: Zeitschrift für Physik, v. 230, p. 225–238, https://doi.org/10.1007/BF01394688

Wan, W., Li, H., Xie, H., Hong, Y., Long, D., Zhao, L., Han, Z., Cui, Y., Liu, B., Wang, C., and Yang, W., 2017, A comprehensive data set of lake surface water temperature over the Tibetan Plateau derived from MODIS LST products 2001-2015: Scientific Data, v. 4, https://doi.org/10.1038/sdata.2017.95

Wang, C., Zhao, X., Liu, Z., Lippert, P. C., Graham, S. A., Coe, R. S., Yi, H., Zhu, L., Liu, S., and Li, Y., 2008, Constraints on the early uplift history of the Tibetan Plateau: Proceedings of the National Academy of Sciences of the United States of America, v. 105, n. 13, p. 4987–4992, https://doi.org/10.1073/pnas.0703595105

Wei, W., Lu, Y., Xing, F., Liu, Z., Pan, L., and Algeo, T. J., 2017, Sedimentary facies associations and sequence stratigraphy of source and reservoir rocks of the lacustrine Eocene Níubao Formation (Lunpola Basin, central Tibet): Marine and Petroleum Geology, v. 86, p. 1273–1290, https://doi.org/10.1016/j.marpetgeo.2017.07.032

Wei, Y., Zhang, K., Garzione, C. N., Xu, Y., Song, B., and Ji, J., 2016, Low palaeoelevation of the northern Lhasa terrane during late Eocene: Fossil foraminifera and stable isotope evidence from the Gerze Basin: Scientific Reports, v. 6, p. 1–9, https://doi.org/10.1038/srep27508

Wing, S. L., and Currano, E. D., 2013, Plant response to a global greenhouse event 56 million years ago: American Journal of Botany, v. 100, n. 7, p. 1234–1254, https://doi.org/10.3732/ajb.1200554

Wu, F., Miao, D., Chang, M. M., Shi, G., and Wang, N., 2017, Fossil climbing perch and associated plant megafossils indicate a warm and wet central Tibet during the late Oligocene: Scientific Reports, v. 7, p. 1–7, https://doi.org/10.1038/s41598-017-00928-9

Wu, Z., Barosh, P. J., Zhonghai, W., Daogong, H., Xun, Z., and Peisheng, Y., 2008, Vast early Miocene lakes of the central Tibetan plateau: GSA Bulletin, v. 120, n. 9–10, p. 1326–1337, https://doi.org/10.1130/B26043.1

Wu, Z., Yang, Y., Barosh, P. J., Wu, Z., and Zhang, Y., 2014, Tectonics and topography of the tibetan plateau in early Miocene: Acta Geologica Sinica, v. 88, n. 2, p. 410–424, https://doi.org/10.1111/1755-6724.12205

Xia, J.-B., 1983, Cenozoic of Baingoin and its borders, Xizang (Tibet), *in* CGQXP Editorial Committee, Contribution to the Geology of the Qinghai-Xizang Plateau 3, Ministry of Geology and Mineral Resources: Beijing, Geological Publishing House.

Xu, Z. Y., 1980, The Tertiary and its petroleum potential in the Lunpola Basin, Tibet: Oil Gas Geology, v. 1, p. 153–158.

Xu, Z. Y., Zhao, J. P., and Wu, Z. L., 1985, On the Tertiary continental basins and their petroleum potential in Qinghai-Xizang (Tibet) Plateau with Lunpola Basin as example: Contribution to Geology of Qinghai-Xizang (Tibet) Plateau, v. 17, p. 391–399.

Yuan, F., Sheng, Y., Yao, T., Fan, C., Li, J., Zhao, H., and Lei, Y., 2011, Evaporative enrichment of oxygen-18 and deuterium in lake waters on the Tibetan Plateau: Journal of Paleolimnology, v. 46, p. 291–307, https://doi.org/10.1007/s10933-011-9540-y

Zeebe, R. E., 2014, Kinetic fractionation of carbon and oxygen isotopes during hydration of carbon dioxide: Geochimica et Cosmochimica Acta, v. 139, p. 540 552, https://doi.org/10.1016/j.gca.2014.05.005

Zhang, J., Quay, P. D., and Wilbur, D. O., 1995, Carbon isotope fractionation during gas-water exchange and dissolution of CO_2: Geochimica et Cosmochimica Acta, v. 59, n. 1, p. 107–114, https://doi.org/10.1016/0016-7037(95)91550-D

Zhang, K., Wang, G., Xu, Y., Luo, M., Ji, J., Xiao, G., Wang, A., Song, B., Liang, Y., Jiang, S., Cao, K., Chen, F., Chen, R., and Yang, Y., 2013, Sedimentary evolution of the Qinghai-Tibet plateau in Cenozoic and its response to the uplift of the plateau: Acta Geologica Sinica.

Zhu, D.-C., Wang, Q., Chung, S.-L., Cawood, P. A., and Zhao, Z.-D., 2019, Gangdese magmatism in southern Tibet and India–Asia convergence since 120 Ma: Geological Society, London, Special Publications, v. 483, https://doi.org/10.1144/SP483.14